Analysis and Optimization of 3D Antenna Radiation Pattern in Cellular Networks

Mengxin Zhou

A thesis submitted in partial fulfilment of the requirements for the degree of Doctor of Philosophy

The University of Sheffield
Faculty of Engineering
School of Electrical and Electronic Engineering

November 2024

I would like to dedicate this thesis and to my loving parents and partner.

Declaration

I confirm that the Thesis is my own work. I am aware of the University's Guidance on the Use of Unfair Means (www.sheffield.ac.uk/ssid/unfair-means). This work has not been previously been presented for an award at this, or any other, university.

Mengxin Zhou

November 2024

Acknowledgements

I would like to express my sincere gratitude to my supervisor Prof. Xiaoli Chu and adviser Dr. Jiliang Zhang for their continuous guide and support of my Ph.D study and related researches. Their constructive guidance, patience and encouragement have been invaluable in supporting me throughout my study and thesis writing. I would like to thank Porf. Jie Zhang, who gives me support during my Ph.D study as well.

My sincere special thanks go to my colleague Dr. Chen Chen. He contributed in all works in my researches. My researches would not be progressing smoothly without his valuable ideas, suggestions and comments. I also would like to thank Dr. Wulin Liu for the comments in Chapter 3. It also needs to thank my colleagues Dr. Songjiang Yang, Dr. Junwei Zhang, Dr. Wenfei Yang, and Dr. Bintao Hu, who provide me great advice during my study.

Furthermore, I would like to thank the University of Sheffield for all the support they gave during my study, and the support from the European Union's Horizon 2020 Research and Innovation Program under Grant 734798.

Last but not least, I would like to thank my parents and my partner, for supporting me spiritually throughout the study. I would not be who I am today without your love and encouragement.

Abstract

This thesis investigates the impact of 3D antenna radiation patterns on millimeter-wave (mm-Wave) cellular networks and heterogeneous cellular networks (HTCNs), and optimizes BS antenna downtilts to improve network performance.

Mm-Wave cellular networks and two-tier HTCNs with uniform rectangular arrays (URAs) are modeled to investigate the impacts of downtilts and BS statistical measures on downlink transmission performances. Results indicate that appropriate measure adjustments can significantly enhance the cell-averaged spectral efficiency (SE) of mm-Wave networks, and spatially-averaged coverage probability, area spectral efficiency (ASE), and energy efficiency (EE) of HTCNs. Additionally, beam-selection is applied to enhance the EE in mm-Wave networks with various precoding schemes. Analysis of HTCN cell-edge average coverage probability under specific BS deployments reveals negligible impact of downtilts and transmit power.

Optimizing antenna downtilts is critical for effective network deployment. In mm-Wave networks, optimal BS antenna heights and downtilts for cell-averaged SE maximization are initially obtained through quick numerical searches, providing useful deployment guidelines. A tractable iterative algorithm is then proposed for 3D beamforming optimization, jointly optimizing precoding and downtilting to maximize the sum SE. Results validate the algorithm's feasibility, convergence, and potential for significant sum SE gains. In HTCNs, the optimal downtilts across tiers are derived via partial derivatives and the bisection method, showing that the downtilt-pair optimization can greatly enhance the spatially-averaged coverage probability, ASE, and EE.

To facilitate fast computation of integrals in analytical expressions, a Riemann sum approximation method is proposed by discretizing user positions to approximate their continuous distribution in mm-Wave networks. Meanwhile, a Gauss-Chebyshev quadrature method is applied to transform definite integrals into weighted sums in HTCNs. Results validate the accuracy and effectiveness of these methods.

Future work could explore more complex transmission scenarios, advanced interference management techniques, and dynamic user behaviors to further expand the potential of 3D antenna pattern design in cellular networks.

Table of Contents

List of Figures

List of Tables

List of Abbreviations

AAA active antenna array

AAS active antenna system

ACI adjacent channel interference

AO alternating optimization

AoD angle of departure

AP access point

ASE area spectral efficiency

B-MIMO beamspace multiple-input multiple-output

BS base station

CCI co-channel interference

CSI channel state information

DLA discrete lens array

DoF degrees of freedom

EE energy efficiency

FD-MIMO full-dimensional multiple-input multiple-output

FP fractional programming

HG hexagonal grid

HMCN homogeneous cellular network

HPBW half-power beamwidth

HPPP homogeneous Poisson point process

HTCN heterogeneous cellular network

LDT Lagrangian dual transform

LOS line-of-sight

LSAA large-scale antenna array

LTE Long-Term Evolution

MBS macro-cell base station

MIMO multiple-input multiple-output

MISO multiple-input single-output

Mm-Wave millimeter-wave

NLOS non-line-of-sight

NLP nonlinear programming

NOMA non-orthogonal multiple access

OFDMA orthogonal frequency-division multiple access

PPP Poisson point process

QT quadratic transform

RF radio frequency

SBS small-cell base station

SE spectral efficiency

SG stochastic geometry

SINR signal-to-interference-plus-noise ratio

SIR signal-to-interference ratio

TDD time-division duplex

3GPP 3rd Generation Partnership Project

TXRU transceiver units

UE user equipment

URA uniform rectangular array

WF Wiener filter

ZF zero-forcing

Chapter 1

Introduction

1.1 Background

With the fast growth of mobile devices and Web-based applications, the unprecedented data volume leads to a huge explosion in demands on capacity in wireless networks. Under the coverage of cellular network resources, network services such as live streaming, social media websites, and web browsing drive the new manner of interaction and cooperation among smartphones, laptops, smartwatches, etc. The rapid expansion of the number of social network users leads to a huge requirement for real-time connectivity and the consumption of broadband in bandwidth-hungry applications. It aims to guarantee an environment for base stations (BSs), access points (APs), and user equipment (UE) to communicate with each other smoothly in cellular networks. Since 2010, the capacity of the cellular network has increased by more than 1000 times compared to previous network systems to support such massive-scale communications.

To address the surge in wireless data traffic in cellular networks, the 3rd Generation Partnership Project (3GPP) has been studied and cutting-edge wireless communication techniques for 5G standardization have been developed. Some 5G technologies have evolved from Long-Term Evolution (LTE) technologies in previous generations such as multiple-input multiple-output (MIMO) and the Internet of Things [1], [2]. The innovative 5G technologies involved in massive MIMO, downlink MIMO efficiency enhancement for LTE, three-dimensional (3D) beamforming, non-orthogonal multiple access (NOMA), millimeter-wave (mm-Wave) channel modeling, and small-cell deployments are studied in 3GPP Release 13 and later versions [3], [4]. Full-dimensional multiple-input multiple-output (FD-MIMO) with 3D beamforming is one of the key technologies [5], [6]. It improves the realization of high data rates and coverage gains demand by deploying multiple antenna elements in a two-dimensional (2D) planar active antenna array (AAA). The innovative antenna array provides dynamic beams of radio waves with 3D channel models in both azimuth and elevation domains to adapt high-dimensional cells. Adopting the FD-MIMO systems with advanced digital signal processing schemes allows the realization of massive user service in the same time-frequency resource and therefore delivers the enhancement in network performance as against the conventional MIMO system. Moreover, the FD-MIMO system with 3D beamforming offers significant support for 3D network deployment. It is closer to reality because heights of BSs and users are taken into account and thereby scenarios including multi-floor buildings and stadiums reap the benefits from it.

The primary focus of this thesis is on analyzing and optimizing the downtilt of the BS antenna pattern in 3D cellular networks. This chapter begins by introducing the concepts of FD-MIMO systems and 3D beamforming. Subsequently, the motivations behind BS antenna downtilt design in 3D cellular networks are summarized. Following this, the aims and contributions of the research are presented. Lastly, the structure of this thesis and the notations are outlined.

1.1.1 FD-MIMO with 3D Beamforming

MIMO technology has become increasingly popular in the last two decades due to the growing demand to deal with the surge in data traffic and improve the link reliability of wireless communication systems. In the 3GPP LTE standard, the MIMO antenna array uses a panel with up to eight antenna ports mounted along a shared reflector linearly on the horizontal axis. The configuration limitation leads to the result that further enhancements can still be made to the spectral efficiency (SE) of communication systems. In addition, the beamforming always operates the antenna pattern in the horizontal plane with a wide beamwidth, while the vertical antenna pattern is not taken into account. This urged the development of massive MIMO systems, where hundreds of antenna elements are equipped in an antenna array. They can serve multiple users with the same time-frequency resource via simple signal processing to obtain high-capacity gain and coverage of radio streams. Since increasing the number of antenna elements results in the extension of antenna array size, it is impractical to install massive antenna elements in a linear antenna array at the BSs.

To cope with such a problem, the FD-MIMO technology, which is a common architecture for the massive MIMO design, has been proposed. FD-MIMO enables antenna elements to be readily integrated into a passive 2D planar antenna array and individually controlled by power amplifiers. The rectangular structure antenna array can be considered an array comprising several linear arrays. It not only has the benefit of gaining extra degrees of freedom (DoF) by feasible BS and antenna array form factors, but also enables the dynamic beam pattern to be adapted in both horizontal and vertical planes. From this perspective, the radio wave is possible to be controlled in the 3D space. This type of beam control mechanism is referred to as 3D beamforming.

A typical approach to utilize the vertical domain in 3D beamforming is the antenna tilting design. The fundamental concept of this technique involves adjusting the antenna tilt angle of the beam's main lobe along the vertical axis to reconfigure the radiation pattern [7]. It can be mechanical tilting, electrical tilting, or a combination of these two methods [8]. For mechanical tilting, adjustable brackets are required to rotate the antenna array physically, which is impractical to adapt to the ever-changed network configuration and deployment due to the site visit requirement. While for electrical tilting, the direction of the radiation pattern from each antenna element is electronically altered by a phase shifter, which can be manually adjusted or remotely controlled by the network operator.

Most current research studies focus on electrical tilting since it improves the network capacity better than mechanical tilting. In comparison to mechanical tilting, electrical tilting can provide extra gain by beam steering in the elevation plane and back lobes with a consistent azimuth radiation pattern [9]. With the dynamic adaption of 3D radiation patterns, the performance of cellular networks can be further improved by adjusting the electrical tilt to increase the desired power while mitigating inter-cell interference.

1.2 Motivation

In the channel model, it is worthwhile to investigate the design of directional models as they can enhance the received signal while mitigating inter-cell interference [10]. Plenty of efforts have been taken to design beamforming to improve the performance of cellular networks including the data rate, coverage probability, SE, and energy efficiency (EE), which are the factors that users and operators most care about. In 5G networks, beamforming designs in the horizontal plane have been investigated sufficiently and well adopted in the industry. However, there is limited research focused on their performance in the vertical plane within cellular networks. In [11]–[13], the authors offered the optimal antenna tilt angle solutions and derived an analytical expression of the average SE for an active user in a downlink single-tier cellular network, which shed light on the vertical beamforming design. The downlink 3D beamforming performance of single-tier multi-cell multi-user cellular networks has been analyzed in [14]. The performance of antenna tilting in heterogeneous cellular networks (HTCNs) was studied in [15] and [16]. The authors in [15] initially provided system-level simulations on the performance of antenna tilt angle in homogeneous cellular networks (HMCNs) and HTCNs, respectively. It demonstrated that the system performance of HTCNs is sensitive to the antenna tilt angles. The authors in [16] proposed a guard zone to protect macro-cell UEs from small-cell interference, and jointly optimized the size of the guard zone and antenna tilt angles of macro-cell BSs (MBSs). It is noted that the antenna tilting design in cellular networks draws great research interests from industry and academia for system performance enhancement. However, most existing work related to the vertical tilting design is based on the traditional HMCNs with fixed BSs. In addition, only a few research studies have specifically focused on theoretical solutions for cellular network deployments with 3D beamforming. Therefore, the design of BS antenna tilt in both HMCNs and HTCNs can be further improved.

1.2.1 BS Antenna Downtilt Design in Mm-Wave Cellular Networks

The explosion of daily data traffic urges the increase of data bandwidth, hence the mm-Wave technology is investigated in 5G for denser and smaller populated area service. As the physical size of antenna arrays reaps the benefits of the short wavelength of mm-Wave frequencies, mm-Wave beamforming can be realized in short-range communication. However, the short-range communication results in the fact that the 3D signal propagation distance between the transmitter and receiver is sensitive to BS deployments. As the beamforming aims to direct the signal off and around UEs, the height of BS antenna arrays affects the design of antenna downtilt in multi-cell networks, where the inappropriate BS height might increase inter-cell interference. Only a few research studies focus on 3D beamforming in the deployment of mm-Wave cellular networks. Authors in [17] jointly optimized the BS antenna electrical downtilt and mechanical downtilt in a single-cell mm-Wave MIMO system for instantaneous antenna gain enhancement. In [18], the cell coverage and cell average SE for a single-cell mm-Wave network were derived to investigate the impact of height and downtilt of BS antenna. It is noted that the above existing studies do not take into account mm-Wave beamforming in multi-cell networks, whereas the BS deployment including the BS antenna height and antenna downtilt in multi-cell mm-Wave networks is worth investigating.

1.2.2 BS Antenna Downtilt Design in Multi-tier HTCNs

As an HTCN comprises a conventional macro-cell network overlaid with a variety of low-power infrastructure, the BS deployment in an HTCN is much denser than in an HMCN. In this perspective, inter-cell interference generated from multiple tiers becomes more complicated. Compared to the typical hexagonal grid (HG) model, the well-established stochastic geometry (SG) provides a more realistic and tractable analytical framework. The authors in [19] developed a tractable, flexible, and accurate model for a downlink HTCN comprising multiple tiers of randomly distributed BSs following Poisson Point Processes (PPPs). They derived an expression for coverage probability for the entire HTCN with both open and closed forms, which provided useful insights into the HTCN deployment design. Based on this system model, a little research improved the HTCN performance by taking into account the BS vertical antenna pattern [16], [20], [21]. In [20], the authors optimized the MBS vertical tilt angle by considering the users distributed at different heights. In [21], the impact of MBS antenna downtilt and sleep region on EE was studied and optimized in both HMCNs and HTCNs. It is noted that the above research studies do not fully take into account the BS antenna downtilts across all tiers of HTCNs. The joint impact of BS deployment parameters across all tiers including BS antenna downtilts, BS antenna heights, and BS densities should be investigated. The lack of attention on balancing BS antenna downtilts among all tiers results in a miss of the opportunity for further HTCN performance enhancement.

1.3 Thesis Aims and Contributions

1.3.1 Research Aims

This thesis mainly focuses on improving the performance of 3D cellular networks by investigating BS antenna downtilts in mm-Wave cellular networks and HTCNs. The research aims can be summarized as follows:

- To explore the relationship between BS antenna downtilts and various BS statistical measures in mm-Wave cellular networks and HTCNs.
- To evaluate the combined impact of BS antenna downtilts and various BS statistical measures on the performance of mm-Wave cellular networks and HTCNs.
- To jointly optimize BS antenna downtilts and various BS statistical measures to maximize the performance of mm-Wave cellular networks and HTCNs.
- To enhance computational efficiency in evaluating the spatially averaged performance of mm-Wave cellular networks and HTCNs.
- To evaluate the performance of multi-user multi-cell mm-Wave networks with the beam-selection method and various precoding schemes.

1.3.2 Contributions

The main research contributions of the thesis can be summarized as follows:

- The joint impact of the BS antenna height and antenna downtilt on the performance of a mm-Wave 3D large-scale antenna array (LSAA) downlink transmission system is investigated in terms of the user SE within the cell coverage area. An analytical expression for the downlink SE per user averaged over the cell coverage area as a function of the BS antenna height and downtilt is derived. A near-accurate approximation is proposed to reduce the computation complexity. The maximum average downlink SE across the cell coverage area is obtained by the jointly optimized BS antenna height and downtilt.

- The performance of a 3D multi-cell multi-user mm-Wave beamspace MIMO (B-MIMO) network with a beam-selection method is analyzed. Analytical expressions for the downlink cell-averaged SE and EE as functions of BS antenna height and downtilt are derived, considering both Wiener filter (WF) precoding and zero-forcing (ZF) precoding schemes. An efficient numerical method is proposed for fast and accurate computation of the derived expressions.

- A network sum SE maximization problem that jointly optimizes precoding and BS antenna downtilting in a 3D mm-Wave cellular network is formulated. A computationally efficient iterative algorithm based on alternating optimization (AO) and fractional programming (FP) techniques is proposed, leveraging the Lagrangian dual transform (LDT) and the quadratic transform (QT). This algorithm effectively solves the intractable non-convex non-linear sum SE maximization problem. Closed-form expressions for the optimal precoding and BS antenna downtilt are obtained as the problem solutions. The maximum sum SE is obtained by the jointly optimized precoding and BS antenna downtilt.

- The impact of the BS antenna vertical pattern and downtilt on the downlink coverage probability, area spectral efficiency (ASE), and EE of a 3D two-tier HTCN comprising MBSs and small-cell BSs (SBSs) are investigated. A 3D system model is proposed for a two-tier HTCN with multi-antenna BSs, and analytical expressions for the downlink spatially-averaged coverage probability, ASE, and EE are derived. An accurate approximation for spatially-averaged coverage probability is developed to facilitate fast numerical evaluation. A closed-form expression for the cell-edge coverage probability is derived under practical BS deployment scenarios. The BS antenna downtilts in both tiers are jointly optimized to maximize the downlink coverage probability, ASE, and EE. The partial derivatives of the derived spatially-averaged coverage probability expression with respect to the MBS (SBS) antenna downtilt are calculated, and the optimal values are determined utilizing the bisection method.

1.3.3 Publications

The following publications contribute to the overall advancement of the research topic. They are related to the contents of Chapter 6 and Chapter 3, respectively.

1. M. Zhou, C. Chen, and X. Chu, "Impact of 3D Antenna Radiation Pattern on Heterogeneous Cellular Networks," *IEEE Access*, vol. 10, pp. 120866–120879, 2022.
2. M. Zhou, W. Liu, J. Zhang, and X. Chu, "Joint Impact of BS Height and Downtilt on Downlink Data Rate in mmWave Networks with 3D Large-Scale Antenna Arrays," *2020 Int. Symp. Networks, Comput. Commun. ISNCC 2020*, pp. 1–5, 2020.

1.4 Structure of the Thesis

The structure of this thesis is presented in this section, which is organized as follows:

Chapter 2 firstly introduces the background knowledge of FD-MIMO, including the FD-MIMO theory, 3D channel model, and 3D beamforming technique. For the 3D beamforming technique, the 3D beamforming principle, two radiation pattern modeling approaches, and the adaptation of 3D beamforming in cellular networks are mainly presented. Secondly, the mm-Wave MIMO beamforming and B-MIMO are explained according to the features of mm-Wave communication systems. Subsequently, the FP technique including the QT and LDT for MIMO systems optimization is introduced. Finally, the properties and development of HTCNs are illustrated. Two useful techniques for HTCN system modeling to enhance the system load balancing and tractability are also presented.

In Chapter 3, the enhancement of the downlink SE per user at all possible locations in the cell coverage area is proposed by jointly considering the BS antenna height and downtilt for a 3D LSAA downlink transmission in a mm-Wave cellular network. The system model is composed of 3 adjacent clusters, while including all possible path loss and inter-cell interference. An analytical expression for cell-averaged SE as a function of BS antenna height and downtilt is derived, and an approximation approach is utilized to facilitate the computation. The accuracy of the proposed approximate analytical expression for the cell-averaged SE is assessed by simulation. The optimal pair of BS antenna height and downtilt values that maximize the cell-averaged downlink SE is obtained via a quick numerical search.

In Chapter 4, the cell-averaged downlink SE of a 3D multi-user mm-Wave cellular network is improved utilizing a beam-selection method. The system model accounts for both intra-cell and inter-cell interference. Analytical expressions for the cell-averaged SE as functions of BS antenna height and downtilt are derived, leveraging WF precoding and ZF precoding schemes, respectively. An accurate numerical method is developed for rapid computation. The accuracy of the proposed numerical method is validated, the cell-averaged SE is evaluated under various precoding schemes, and the EE enhancements are achieved through the application of the beam-selection method.

In Chapter 5, a 3D mm-Wave cellular network sum SE maximization problem is formulated by jointly optimizing precoding and BS antenna downtilting. A computationally efficient iterative algorithm is developed based on the AO technique and FP approach, leading to the determination of the optimal precoding vectors and BS antenna downtilts that maximize the sum SE. The feasibility and convergence of the proposed joint optimization algorithm are validated.

In Chapter 6, how the BS antenna downtilts of all BSs across different tiers can be jointly optimized to enhance the downlink spatially-averaged coverage probability, ASE, and EE in a 3D two-tier HTCN composed of MBSs and SBSs is investigated. A 3D two-tier HCTN consisting of macro-cells and small-cells is modeled through the SG approach, where the BSs in each tier are assigned an appropriate antenna downtilt to enhance the downlink signal and suppress inter-cell interference. Based on the 3D HCTN model, analytical expressions for the downlink spatially-averaged coverage probability, ASE, and EE are derived as functions of the BS antenna downtilts, BS heights, BS densities and cell-association bias. To facilitate fast numerical evaluation, accurate approximations for the integral parts in the coverage probability expression are proposed. A closed-form expression for cell-edge average coverage probability is derived under practical BS deployment scenarios. The optimal BS antenna downtilts for both tiers that maximize the downlink spatially-averaged coverage probability are obtained by using the partial derivative and the bisection method.

Chapter 7 summarizes the conclusions of the thesis. Potential directions for future work that can be built on the thesis are then discussed.

Notations: Vectors and matrices are denoted by boldface letters; $(\cdot)^{\mathrm{T}}$, $(\cdot)^{\mathrm{H}}$ and $(\cdot)^{-1}$ denote the transpose, the conjugate transpose, and inverse transformation, respectively; $\mathrm{Tr}(\cdot)$ represents the matrix trace; $\mathbb{C}$ and $\mathbb{R}$ denote the set of complex numbers and real numbers, respectively; $\mathcal{CN}(\cdot,\ \cdot)$ represents the complex Gaussian distribution; $|\cdot|$ and $\|\cdot\|$ are the Euclidean norm of scalar and vector variables, respectively; $\Re\{\cdot\}$ denotes the real parts of a complex number; $\mathbb{E}[\cdot]$ represents the statistical expectation.

Chapter 2

Literature Review

In this chapter, the literature related to the thesis is reviewed. The properties of 3D beamforming are first introduced. This section discusses 3D beamforming in FD-MIMO systems, including the FD-MIMO theory, 3D channel model, and 3D beamforming principle. The second section reviews the techniques for mm-Wave MIMO configuration, mm-Wave beamforming design, and B-MIMO. In the third section, optimization techniques including the FP, QT and LDT are detailed. Finally, the key features of HTCN deployment including interference management, user association, and mathematical network framework models are presented in section four.

2.1 3D Beamforming in FD-MIMO Systems

2.1.1 FD-MIMO Theory

FD-MIMO was first proposed as an innovative technology in 3GPP Release 12 workshop in [22]. In 3GPP Release 13 and Release 14, extensive research of FD-MIMO key technologies was studied [4], [23], [24]. Based on studies in [23], 3GPP Release 13 focused on the development of transceiver architectures of FD-MIMO. The antenna configurations for 2D antenna arrays with up to 64 transceiver units (TXRUs) including antenna element spacing, number of antenna elements for each TXRU, number of TXRUs, and polarization are identified and evaluated in both HMCNs and HTCNs. The virtualization model for the antenna elements in each TXRU and the target operating frequency range regarding the practical antenna size limitations are decided. However, due to the limitations of TXRU numbers in 3GPP Release

13, antenna arrays with more TXRUs are restricted to achieve a better performance. FD-MIMO research in 3GPP Release 14 addressed the limitations in Release 13 as well as the overlooked issues on channel state information (CSI).

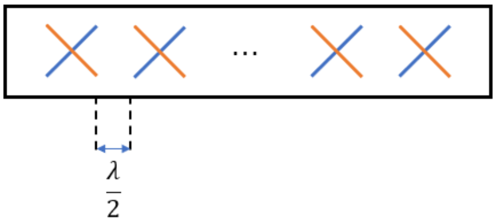

(a) 64 linear array

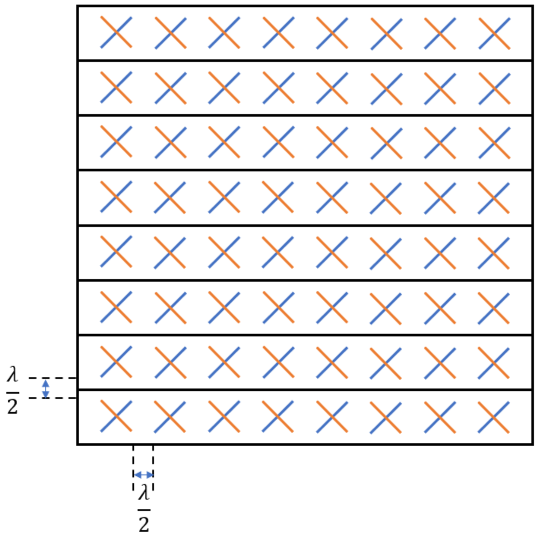

(b) 8 planar array

Fig. 2.1 The structure of a linear antenna array and a planar antenna array with 64 cross-sections.

The conventional MIMO antenna array is a linearly mounted panel with a shared reflector that can accommodate up to eight antenna ports. Since increasing the number of antenna elements results in the extension of antenna array size, it is impractical to install massive antenna elements in a linear antenna array at the BSs. The limitation in the configuration results in the possibility of further improvements in the SE of the communication systems. Therefore, the FD-MIMO technology is proposed to serve multiple users with high-capacity gain and coverage of radio streams.

FD-MIMO is an active antenna system (AAS) that integrates the active transceiver array and the passive 2D planar antenna array into a radome. It is a common architecture for the massive MIMO design. The active transceiver array contains electronic components such as the baseband processing module, amplifiers, and phase shifters to control the direction of beams transmitted from the passive antenna array. The 2D planar antenna array is structured as a rectangular array, which can be considered as an array composed of multiple linear arrays. The design and the actual function of 2D AAA form factors have been explored in [5], [25]–[27]. Fig. 2.1 demonstrates the deployment comparison of 64 perpendicular cross-sections in a linear antenna array and a planar antenna array with half-wavelength dipole element and half-wavelength spacing, where λ denotes the RF carrier wavelength. Assuming a system with an operating frequency of 6 GHz, the linear antenna array would require 3 m horizontal space at the top of BSs. However, this space can be shared with the vertical dimension in the planar antenna array and only 0.4m×0.4m space is required at the top of BSs. According to realistic AASs form factors at the top of the different sizes of cells BSs in Table 2 of [28], the length of the AAS devices equipped at MBSs is always not over 1.5 m and the width of those is always smaller than 0.6 m. Moreover, the room for AAS device installation at SBSs is less than 1/3 of that for MBS AAS device installation. Hence it is more practical to build the planar antenna array at existing BSs. The authors in [29] suggested a framework for FD-MIMO within LTE/LTE-A standards, and discussed the key challenges consisting of downlink precoding, antenna virtualization, and channel quality indicator prediction. The potential of the FD-MIMO technology and its commercial feasibility were suggested in [30] by introducing the theory and architecture of the FD-MIMO prototype. In [31], the authors focused on the configuration of the FD-MIMO and analyzed the data rate of it in practice to achieve a trade-off between cost and performance.

2.1.2 3D Channel Model

The channel model is a geometry-based stochastic channel model that is widely used in 3GPP community to develop the performance of the wireless communication system. The traditional 2D channel model has been implemented in academia as well as industry to evaluate designs for BSs with horizontal linear antenna arrays. The propagation model only captures signal paths in the azimuth plane, while the elevation angles of propagation paths have been disregarded. The design of 2D AAA in FD-MIMO enables the propagation paths in the azimuth plane and elevation plane can be both taken into account, facilitating the generation of 3D radiation patterns. Authors in [5] and [10] extended the 3GPP 2D channel model to the 3D channel model for preliminary research on radio beam patterns in the elevation plane. A comprehensive overview of the latest advancements in the 3D channel model was presented in [32], with a particular focus on research pertaining to the vertical angle. The author in [33] summarized and provided insights into the 3D channel model in 3GPP by considering UEs located on high floors.

There are some ongoing efforts focusing on enhancing the 3D channel model and refining the estimation of various parameters in the elevation domain [34]–[38]. The elevation angle of departures (AoDs) in the urban microcell environment based on channel measurements at a center frequency of 2.3 GHz was studied in [34]. The authors found a notable variation in the AoDs for line-of-sight (LOS) and non-line-of-sight (NLOS) propagation scenarios, where the AoDs followed an exponential model for LOS propagation and a linear model for NLOS propagation. In [35], the 3D channel model was developed by proposing a simplified 3D Weichselberger model to improve its accuracy and performance. The authors in [36] extensively carried out field measurements using a 3D channel model for scenarios involving outdoor and indoor communications to compare channel capacity with the 2D case. In [37], the authors investigated the LOS 3D channel model for short-range indoor scenarios and optimized the placement of transmit antennas. In [38], the authors recognized the shortcomings of existing 3D channel models in explaining the distance-related characteristics of parameters in the elevation domain and the correlation between azimuth and elevation angles. To address these limitations, a reliable and realistic 3D stochastic channel model was proposed with an outfield measurement campaign.

2.1.3 3D Beamforming Technique

2.1.3.1 3D Beamforming Principle

Beamforming is a spatial filtering operation that transmits signals at an identical wavelength and phase from multiple elements in an array toward an intended direction [39]. Modern communication techniques deploy beamforming systems to enhance the network capacity by combining the antenna array gain with diversity gain and interference reduction. It is achieved by employing a phased array to enable the electronic beam steering. The output spatial power distribution is presented as the radiation pattern, which is determined by the combined vector fields of individual antenna elements.

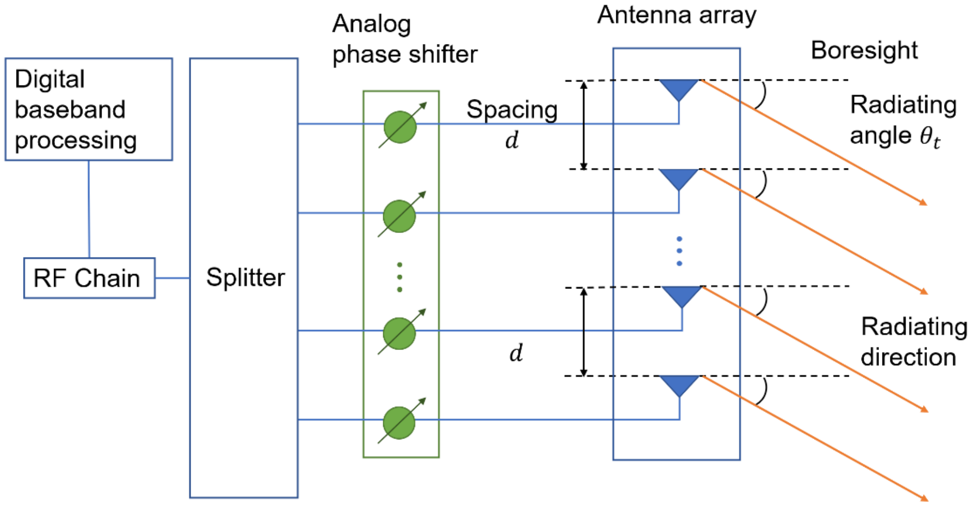

Fig. 2.2 Analog beamformer architectures.

There are three types of beamforming, which are analog beamforming, digital beamforming, and hybrid beamforming. The simplest beamforming technique to process the signal before it reaches the antenna elements is analog beamforming. Fig. 2.2 exhibits the system configuration for analog beamforming utilizing phased arrays. The signal from a single transceiver passes the exclusive RF chain and is divided into several amounts of signals corresponding to the number of antenna elements. Then each divided signal is amplified and arrives at the corresponding antenna element to generate a radiation pattern. The shape and the direction of the beam pattern from each antenna element are electronically controlled by a phase shifter. The elevation radiating angle θ_t, also known as downtilt, which is the angle between the boresight and the radiating direction, is altered by the phase shift φ for a scheduled input signal and the antenna element spacing d. The general guideline for determining the resulting beam angle is described as follows [40]:

$$\theta_t = \arcsin\left(\frac{\varphi \cdot \lambda}{2\pi \cdot d}\right). \tag{2.1}$$

Since each antenna element maps onto a specific phase and amplitude weight, the radiation pattern would be more accurately modeled at the element level.

In contrast to the analog beamforming, the RF chain in the digital beamforming is dedicated to each antenna element path. The phases and amplitudes of the signals are digitally modified by baseband processing before RF transmission, which provides more degrees of freedom to enhance flexibility and efficiency. Beams from the antenna elements in the same group can be radiated simultaneously. However, it suffers power consumption and hardware complexity due to the large quantity of RF chains.

Based on the features of analog beamforming and digital beamforming, a hybrid array architecture was proposed by grouping element paths into several analog sub-arrays [41], [42], which provides a trade-off between the simplicity of analog beamforming and the high processing performance of digital beamforming.

As the antenna elements are arranged linearly in the traditional MIMO antenna array, conventional beamforming always operates the antenna pattern in the horizontal plane with a wide beamwidth, while the vertical pattern with the narrow beamwidth is fixed in direction. This is known as 2D beamforming. The combination with the cell sectorization method allows it to exploit the resource assignment to reduce interference and improve the network capacity. Rather than utilizing an omni-directional antenna array at the BS in a network cell, the cell is divided into several sectors and each sector is served by fan-shaped radiation patterns from one of the directional antenna arrays at the BS. Compared to the traditional linear MIMO, a salient feature of FD-MIMO is that a stack of vertically arranged antenna elements in the planar antenna array can be fed by a transceiver port with identical data symbols, then the AAS allows dynamic beam patterns in both horizontal and vertical dimensions to adapt different cell range and vertical cell geometries. This type of beam control method is referred to as 3D beamforming. It can allocate different powers to beams to serve UEs close to the cell center and the cell border separately.

The initial works on 3D beamforming focus on the beamforming in the elevation plane based on the system-level studies and field trials to validate the improvement of gain [40], [43]–[47]. In [43], the realizations of vertical beam steering were investigated in noise-and-interference-limited environments. The authors also explored the impact of the antenna downtilts, vertical half-power beamwidth (HPBW), and inter-site distance on the SE and cell coverage. The authors in [44] demonstrated how 3D beamforming provides extra DoF and how it dynamically suppresses interference by adapting the vertical dimension of the antenna pattern. In [45] and [47], the lab and field trials were utilized to validate the expected performance of 3D beamforming in real indoor and outdoor deployments with the adaptation of BS antenna downtilt. The authors in [40] and [47] considered various approaches for BS antenna downtilt adaptation in single-cell and multi-cell network scenarios with and without inter-BS antenna beam coordination to mitigate interference. These works explored the basic ideas of 3D beamforming, thereby uncovering a multitude of potential application areas and implementation options.

2.1.3.2 Radiation Pattern Modeling

- **Antenna Port Approach**

Encouraged by the promising outcomes of 3D beamforming realizations in real networks, theoretical studies on BS antenna downtilt adaptation were carried out by employing the antenna radiation pattern expression presented in [48] and [49]. Early research considered the 3D channel between the transmitting BS antenna port and the UE rather than the port constituted by physical antenna elements. This approach is based on the fact that the antenna elements within a port transmit the same signal with corresponding weights to achieve the desired downtilt angle, thereby presenting each port as a single antenna to the UE. The role of individual antenna elements and downtilt weights in determining the 3D antenna port radiation pattern is not taken into account. The combined 3D antenna port radiation pattern consists of a Gaussian-shaped main lobe and is attached to some side lobes. The approximate expression of it is defined in [49] in dBi and is given by

$$A_{P,3D}(\theta,\phi,\theta_t) = -\min\left\{-\left[A_{P,V}(\theta,\theta_t) + A_{P,H}(\phi)\right], A_{P,m}\right\} + G_{P,max}, \quad (2.2)$$

where $G_{P,max}$ is the maximum directional antenna port gain; $A_{P,m}$ denotes the port front-to-back ratio;

$$A_{P,V}(\theta,\theta_t) = -\min\left[12\left(\frac{\theta-\theta_t}{\theta_{P,3dB}}\right), SLA_{P,V}\right], \quad (2.3)$$

$$A_{P,H}(\phi) = -\min\left[12\left(\frac{\phi-\phi_t}{\phi_{P,3dB}}\right), SLA_{P,H}\right], \quad (2.4)$$

where $\theta_{P,3dB}$ and $\phi_{P,3dB}$ denote the port HPBW in the elevation and the azimuth plane, respectively; θ and ϕ are the elevation and azimuth angles relative to the user location; $SLA_{P,V}$, $SLA_{P,H}$ represent the maximum value of port side lobes in the antenna radiation pattern for the respective planes; ϕ_t is the horizontal steering angle of the antenna boresight.

This approach is widely employed in current studies on 3D beamforming, primarily since the channel is a direct function of each port's downtilt angle [9], [11]–[13], [50]–[52]. Utilizing the approximate antenna port radiation pattern expression, the authors in [9] demonstrated the user throughput in conventional non-coordinated MIMO systems when considering the BS antenna downtilt via system-level simulation. The vertical antenna radiation pattern in the single-cell multiple-input single-output (MISO) system was investigated in [50]. The authors proposed a coordinated framework in which multiple BSs jointly adjust the antenna downtilts to enhance the sum throughput of a scheduled user. In [51], the authors also utilized vertical beamforming in a single-cell multi-user MIMO system. The cell is divided into several vertical regions, and one out of a finite number of downtilt and HPBW sets is applied to serve each region. A scheduler is employed to select the vertical region for transmission in each time slot to optimize the user throughput.

In [11] and [12], the authors proposed a framework based on the probability density function of user distribution on the vertical plane. Combined with the antenna port radiation pattern, they optimized the vertical tilting angle for active and passive antenna systems in downlink single-user and multi-user MIMO networks.

The optimization of BS antenna downtilt represents a significant advancement in exploring vertical antenna patterns. The authors in [52] focused on dealing with the problem of optimizing the antenna tilt angle adjustment under the constraints of the cellular network. As the optimization problem is non-convex, the authors analyzed the situations where the problem can be transformed into a convex optimization and developed a primal-dual approach to determine the optimal antenna downtilt. In [13], the authors addressed the joint optimization problem of BS antenna downtilt adjustment and the closed-loop precoding design by proposing an algorithm that separates the problem into two sub-problems.

- **Antenna Element Approach**

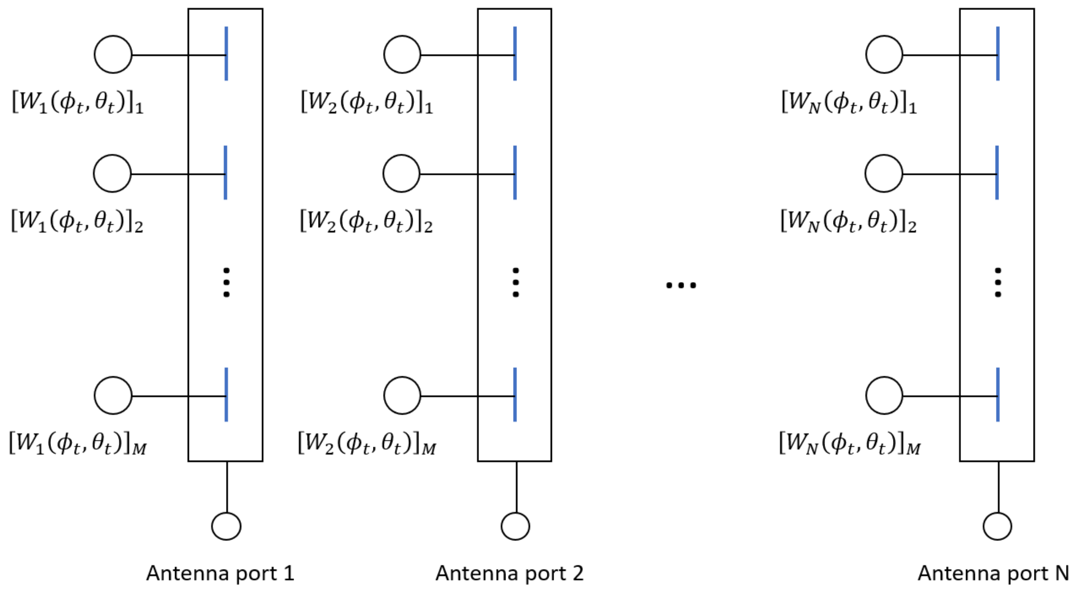

Fig. 2.3 An AAA with N sub-array partitions, each containing M elements.

In order to improve the accuracy and realism of the 3D beamforming techniques, the individual antenna elements should be taken into account in the 3D model design. The overall antenna radiation pattern which is generated from a port is determined by the layout and the number of antenna elements within the antenna array, as well as the radiation pattern of each antenna element and the applied weight. Mathematically, it is expressed as the combination of the antenna element radiation pattern and the array factor specific to the port. Considering N uniform linear sub-array partitions in a planar antenna array, of which each sub-array contains M antenna elements, as shown in Fig. 2.3. The combined 3D antenna element radiation pattern is expressed in dBi scale as follows [53],

$$A_{E,3D}(\theta,\theta_t,\phi) = -\min\left\{-\left[A_{E,V}(\theta,\theta_t) + A_{E,H}(\phi)\right], A_{E,m}\right\} + G_{E,max}, \qquad (2.5)$$

where $G_{E,max}$ is the maximum directional antenna element gain; $A_{E,m}$ is the element front-to-back ratio;

$$A_{E,V}(\theta,\theta_t) = -\min\left[12\left(\frac{\theta-\theta_t}{\theta_{E,3dB}}\right), SLA_{E,V}\right], \qquad (2.6)$$

$$A_{E,H}(\phi) = -\min\left[12\left(\frac{\phi-\phi_t}{\phi_{E,3dB}}\right), SLA_{E,V}\right], \qquad (2.7)$$

where $\theta_{E,3dB}$ and $\phi_{E,3dB}$ denote the element HPBW in the elevation and the azimuth plane, respectively; $SLA_{E,V}$ and $SLA_{E,H}$ represent the element side lobe levels for the respective planes.

The array factor quantifies the extent to which a particular characteristic changes due to the grouping of elements in an antenna array, and is given as follows,

$$A_F = \boldsymbol{S}\cdot\boldsymbol{W}, \qquad (2.8)$$

where $\boldsymbol{S}$ represents the phase shift, which is determined by the array placement; $\boldsymbol{W}$ represents the weighting factor, which is dependent on the steering angle in the horizontal and vertical plane. They are given by [4]

$$\boldsymbol{S}(\phi,\theta) = [\boldsymbol{s}_1(\phi,\theta)\boldsymbol{s}_2(\phi,\theta) \ldots \boldsymbol{s}_N(\phi,\theta)], \qquad (2.9)$$

$$\boldsymbol{W}(\phi_t,\theta_t) = [\boldsymbol{w}_1(\phi_t,\theta_t)\boldsymbol{w}_2(\phi_t,\theta_t) \ldots \boldsymbol{w}_N(\phi_t,\theta_t)]^{\mathrm{T}}, \qquad (2.10)$$

where

$$[\boldsymbol{s}_n(\phi,\theta)]_m = \exp\left(j2\pi\left((n-1)\frac{d_H}{\lambda}\sin\theta\sin\phi + (m-1)\frac{d_V}{\lambda}\cos\theta\right)\right), \quad (2.11)$$

$$[\boldsymbol{w}_n(\phi_t,\theta_t)]_m = \frac{1}{\sqrt{MN}}\exp\left(-j2\pi\left((n-1)\frac{d_H}{\lambda}\sin\phi_t + (m-1)\frac{d_V}{\lambda}\cos\theta_t\right)\right), \quad (2.12)$$

where $n = 1,2,\dots,N$ denotes the sub-array partition index and $m = 1,2,\dots,M$ denotes the index of antenna elements in each sub-array partition; d_H and d_V represent the horizontal and vertical antenna element spacing, respectively.

The exact expression of an antenna radiation pattern for a sub-array port n is given by [54]

$$A_{O,n}(\theta,\theta_t,\phi) = A_{E,3D}(\theta,\theta_t,\phi) + 20\log_{10}|[\boldsymbol{A}_F]_n|. \quad (2.13)$$

In [55], the authors demonstrated that the single-cell multi-user MIMO network performance can be improved by utilizing the antenna element approach channel model, because it can control not only the beam direction, but also the shape of beams.

In [56], the authors investigated the reduced complexity B-MIMO transceivers which is applied to the AP antenna array serving multi-user mm-Wave networks by utilizing the antenna element approach channel model. Their findings demonstrate that the network SE is heavily affected by the configuration of the antenna array, including the array rotation angle, the number of antenna elements, and the number of beams.

An elevation beamforming algorithm for the FD-MIMO system was provided in [57] by considering the quasi-static channel covariance matrices of users. The authors derived a predictable equivalent of signal-to-interference ratio (SIR) by establishing a functional relationship with BS downtilt port weight vectors. The downtilt weight vectors were also quasi-optimized to maximize the SIR.

In order to enhance the downlink mm-Wave transmission from an AP featuring a large number of antenna elements with FD-MIMO technology to multiple users, the authors in [58] introduced a beam selection algorithm along with an associated precoder to maximize the SE for the system.

- **Comparison and Selection of Antenna Port and Element Approaches**

In the previous section, two radiation pattern generation approaches for antenna arrays were introduced. The antenna port approach simplifies the role of antenna elements in realizing beam radiating angle by approximating the overall radiation pattern of a sub-array partition port with a narrow beam. In the antenna element approach, the overall radiation pattern generated from an antenna port can be viewed as a superposition of the individual antenna element radiation pattern and the array factor for the entire port.

These two approaches are both extensively utilized in 3D channel model construction in current studies. To identify the differences between these two approaches in practice, the overall radiation patterns generated using these two approaches are compared.

A uniform linear array with a column of M antenna elements is considered, and only the vertical beam pattern is investigated ($\phi = 0°$). According to (2.8)-(2.12), the array factor is computed as,

$$\begin{aligned} A_F(\theta, \theta_t) &= \boldsymbol{s}(\phi, \theta)\boldsymbol{w}(\phi_t, \theta_t) \\ &= \sum_{m=1}^{M} \frac{1}{\sqrt{M}} \exp\left(j2\pi(m-1)\frac{d_V}{\lambda}(\cos\theta - \cos\theta_t)\right). \end{aligned} \tag{2.14}$$

To achieve a more precise antenna port radiation pattern, $G_{P,max}$ and $\theta_{P,3dB}$ can be computed using the following calculations based on the array configuration [59],

$$G_{P,max} = G_{E,max} + 20\log_{10}\sqrt{M}, \tag{2.15}$$

$$\theta_{P,3dB} \simeq 2\left[\frac{\pi}{2} - \cos^{-1}\left(\frac{1.391\lambda}{\pi M d_V}\right)\right]. \tag{2.16}$$

Table 2.1 Simulation Settings for the Antenna Port Approach and the Antenna Element Approach

	Parameter	**Value**
Basic parameters	Number of elements, M	8
	Downtilt angle, θ_t	90°
Antenna element approach parameters	Maximum directional antenna element gain, $G_{E,max}$	8 dBi
	Vertical element HPBW, $\theta_{E,3dB}$	65°
	Vertical element side lobe, $SLA_{E,V}$	30 dBi
	Element front-to-back ratio, $A_{E,m}$	30 dBi
	d_V/λ	0.8
	Vertical port side lobe, $SLA_{P,V}$	20 dBi
	Port front-to-back ratio, $A_{P,m}$	25 dBi

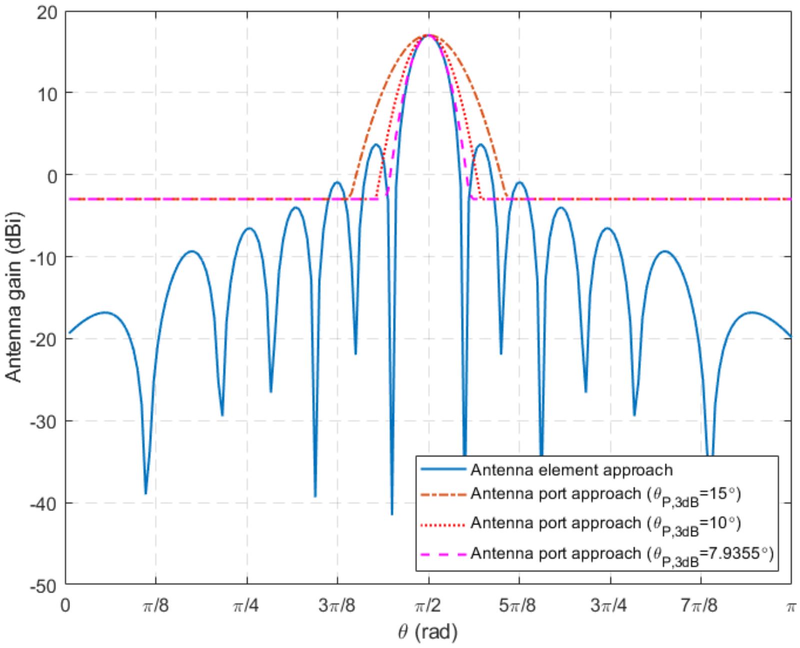

Fig. 2.4 Comparison of the vertical radiation pattern for the antenna element approach and the antenna port approach.

The rest simulation parameters are set in Table 2.1 in accordance with the values in [49], [53]. Utilizing parameter values in Table 2.1, the results $G_{P,max} \approx 17$ dBi and $\theta_{P,3dB} = 7.9355°$ can be obtained. The vertical antenna radiation patterns generated by the antenna element approach and the antenna port approach are presented in Fig. 2.4. The antenna port approach benchmarks for $\theta_{P,3dB} = 15°, 10°$ provided in [49] are also simulated to study the impact of HPBW on the radiation pattern. It is shown that smaller $\theta_{P,3dB}$ results in the narrower vertical main beam. Comparing the radiation pattern generated by different approaches, it can be seen that the side lobes of the port radiation pattern are dismissed, while only the main beams are taken into account. Nevertheless, the main beam generated using the antenna port approach can closely align with that produced by the antenna element approach by utilizing $\theta_{P,3dB}$ obtained through (2.16), which accounts for the actual array configuration and operating frequency.

The antenna port approach proves to be remaining wildly favored in theoretical studies on 3D beamforming due to its simplicity [9], [11]–[13], [50]–[52]. It works effectively in an extensive range of scenarios, with the exception being when the tilt angle is excessively low or high. In such cases, when users are located far away from the main beam, the influence of side lobes becomes significant in the beamforming process. The radiation pattern generated by the antenna element approach is more accurate since the beam can be controlled by means of the downtilt weight applied to each element. Furthermore, (2.12) can be replaced by other unity norm weight vectors depending on the specific situations [4].

2.1.3.3 3D Beamforming in Cellular Networks

- **Antenna Tilting Schemes**

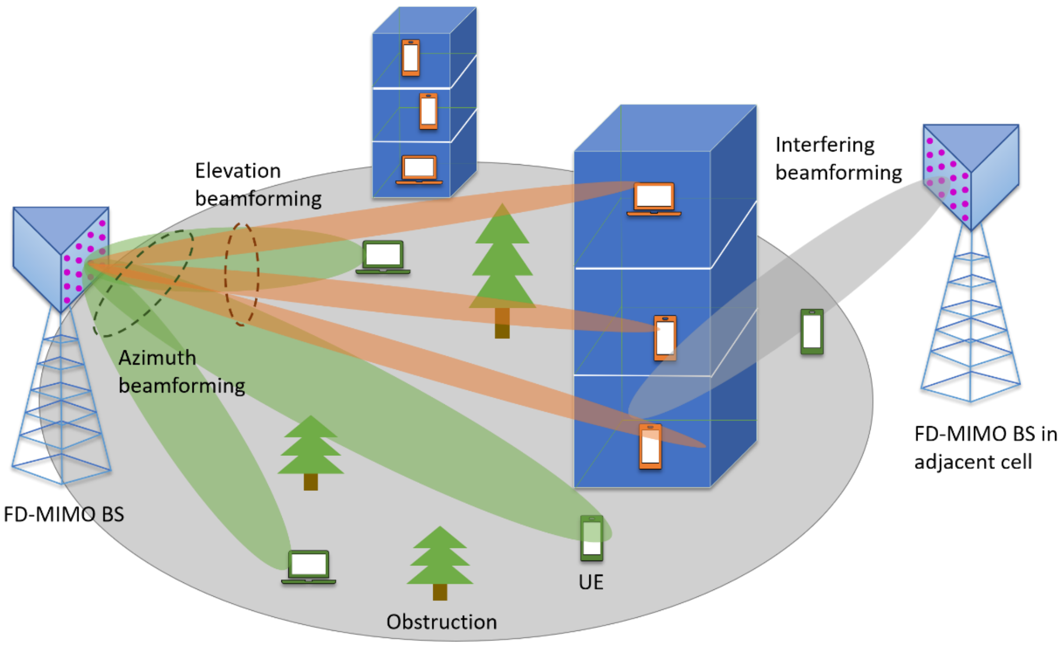

Fig. 2.5 FD-MIMO beamforming in cellular networks.

To cope with the ever-changed configuration and deployment, antenna tilting is a typical approach in the 3D beamforming technique to adapt to the changes in the network and improve the network performance. The fundamental idea of this scheme is adjusting the BS antenna downtilt to reconfigure the network with ever-changing demands. The BS antenna aims to radiate most of the power into the desired direction and avoid it becoming interference for undesired locations. It can strike a balance between the desired signal and interference for the FD-MIMO multi-cell network. The signal-to-interference-plus-noise ratio (SINR) at users can be enhanced without physically regulating the BS antenna position. Fig. 2.5 shows a macro cell comprising multiple UEs. Due to the adjustment of the vertical beam, UEs deployed on different floors can be taken care of. Depending on the novelty of elevation beam adjustment in 3D beamforming, there are two operation modes for antenna tilting angle design [45]. On the one hand, the tilt of the vertical beam can be fixed at an appropriate value for a certain area in the target sector. The tilting angle is always determined by the given statistical measures for a long-term average sense such as the density of users, the height of BSs, and the power transmitted from BSs. This is referred to as the cell-specific tilting design. On the other hand, the vertical tilting angle can be dynamically adjusted towards the exact location of the target UE instantaneously, which maximizes the desired UE signal. This is referred to as the user-specific tilting design.

These two tilting design schemes were introduced in [50] and applied in [60]. In [60], the authors discovered that the vertical sectorization and tilting selection scheme exploited in [51] cannot ensure the attainment of maximum system throughput. This approach lacks a specific algorithm for throughput maximization. In this perspective, the coordinated cell-specific and user-specific tilting scheme is proposed to enhance the cell-average and cell-edge throughput.

- **Interference Management by 3D Beamforming**

Since the possibility of users located at the cell edge is larger than that of users located at the cell center, it is probable that the beam is steered to the direction close to the cell edge in a 3D geometry network, which leads to interference in adjacent cells [43]. In [61], the authors proposed specific downtilts for the cell-center and cell-edge UEs to mitigate interference and maximize the throughput for UEs in both regions. In [62], a coordinated 3D beamforming approach was proposed in a high delay or mobility cellular network to mitigate inter-cell interference. The approach is composed of an interference cancellation strategy in the horizontal plane and a BS antenna downtilt control strategy in the vertical plane. The authors in [63] divided a hexagon coverage area into two disjoint vertical regions and adapted a hybrid multi-cell BS radiation pattern cooperation strategy to control interference in an MU-MIMO network with imperfect CSI. They focused on the cell-specific tilting scheme and investigated the impact of BS antenna downtilt on the throughput of the traditional uncoordinated transmission and the beamforming coordination transmission, respectively. In the cooperative transmission model, the channels of all BSs function as a single distributed antenna transmitter, where the data and CSI of all UEs are shared among BSs. This transmission model was investigated in [64] as well. The authors divided the network into clusters and proposed a two-level 3D beamforming coordination approach including the intra-cluster interference coordination and the inter-cluster interference coordination. The results show that the system capacity and the throughput of cluster-edge UE are improved under the proposed transmission approach.

2.2 Mm-Wave MIMO Beamforming

The Mm-Wave communication system is envisaged as a promising technique to meet the capacity demands in 5G networks. It occupies the high-frequency spectrum range from 30 GHz to 300 GHz, which offers significant advantages in terms of high transmission data rates up to the order of Gigabits/second and low latency service [65]–[67]. Compared to traditional microwave communications with the frequency spectrum between 2.4 GHz and 5 GHz, mm-Wave provides much wider bandwidths and has the potential to revolutionize the higher mobile data traffic. The high frequency of mm-Wave significantly reduces the physical size of the antenna elements due to the short wavelength. On the one hand, this can shrink the size of antenna arrays and realize the small coverage area within 200 m, which compensates for particular challenges of mm-Wave frequencies including high propagation attenuation, sensitivity to blockage, and penetration loss [65], [68], [69]. On the other hand, the increased carrier frequency enables the dense packing of a large number of antenna elements in a compact form factor within a fixed spatial dimensional antenna array, which is referred to as the mm-Wave massive MIMO. It enhances the antenna gain and directivity with extremely narrow beamwidth and could be expected that the capacity of a dense network with the mm-Wave technique can achieve 1000-fold enhancement for 5G [70]. However, it should be noted that there is a limitation on the maximum number of antenna elements in an antenna array. An example in 3GPP presents that the maximum antenna element for the BSs and UEs in a system operating at 70 GHz are 1024 and 64, respectively. For RF chains, these numbers are 32 and 8, respectively [3], [71]. To maximize the performance of the mm-Wave massive MIMO system, it is useful to set the antenna element spacing to more than 0.5λ, and ensure channel coefficients of the transmitter-receiver antenna pairs exhibit independent fading.

Due to the small size of antenna arrays in the mm-Wave communication system, the low transmitting power and high propagation loss urge the requirement of beamforming to compensate for the signal power received by UEs. The design of the transceiver beamformer relies on the CSI, hence the optimal beamforming performance is dependent on the channel estimation [72], [73]. The overviews and guidelines of beamforming in mm-Wave wireless communication systems are provided in [39], [68], [69], [74]. According to the introduction of beamforming categories in Section 2.1.3.1, the low complexity analog beamforming technique is mainly applied in indoor mm-Wave networks with short-range communications in the 60 GHz frequency band [75], [76]. For outdoor mm-Wave networks with operating frequencies at 28 GHz, 38 GHz, 73 GHz, and the range between 81-86 GHz [77], hybrid beamforming can provide additional signal processing to improve the efficiency of multiple channel transmission and interference management.

The mm-Wave beamforming design was studied in [78]–[85]. The sub-array structure for the hybrid beamforming was investigated in [78]. The authors proposed an iterative beamforming scheme to nearly optimize the system performance with low structure complexity. In [79], the authors considered two types of hybrid beamforming structures, which are fully-connected structures and partially-connected structures, respectively. The beamforming design was perceived by a matrix factorization problem, and addressed by a minimization algorithm for these two structures in the orthogonal frequency-division multiplexing (OFDM) system. However, due to the complexity of the algorithm, the authors in [81]–[83] proposed two iterative algorithms. One is based on the power factorization method, and the other is based on the Gauss-Seidel method. These algorithms aim to reduce the complexity and improve the beamforming performance. In [80], the non-convex optimization problem of the hybrid unicast and multicast beamforming design was addressed by a low-complexity hybrid ZF beamforming scheme. The scheme was designed in two directions. On the one hand, the channel gains were enhanced by optimizing the analog beamformers. On the other hand, inter-cell interference was mitigated by jointly optimizing the digital beamformers and the power allocation strategy. In [84], the authors proposed a federated learning framework for hybrid beamforming design in mm-Wave massive MIMO systems. It only requires gradient information for model training, and can provide more powerful and tolerant performance compared to centralized machine learning frameworks. For high-speed mobile mm-Wave communication systems, a two-stage beamforming scheme was proposed in [85]. First, the authors developed an algorithm to solve a threshold-constrained beam pattern approximation problem. Then, a binary search method was utilized to widen the coverage of each beam, thereby reducing BS antenna switching power.

2.2.1 Beamspace MIMO

The adoption of large-scale MIMO techniques at mm-Wave frequencies remains impractical due to the significant number of antenna elements and the resulting high hardware complexity [86]. The deployment of a large number of antenna elements inherently necessitates a corresponding increase in the number of RF chains. Studies have demonstrated that systems employing massive antenna arrays in MIMO are especially vulnerable to imperfections in the RF chains, which contribute to further performance degradation [87]. Furthermore, it has been shown that RF components can account for as much as 70% of the total power consumption of the transceiver [88]. To harness the benefits of mm-Wave communications, current research is focused on developing novel techniques designed to reduce the transceiver hardware complexity of large-scale MIMO systems. B-MIMO is one of the techniques that gained considerable attention due to its ability to reduce the number of required RF chains [89]–[91]. By utilizing a discrete lens array (DLA) in place of a traditional electromagnetic antenna array, B-MIMO can convert the conventional spatial channel into a beamspace channel by focusing signals onto different points on the focal surface [89], [92]. Due to the limited scattering in mm-Wave communications, the number of effective propagation paths is relatively small, thus only a few beams are utilized. Consequently, the mm-Wave beamspace channel exhibits sparsity, allowing for the selection of a limited number of dominant beams [89]. This notably reduces the MIMO system dimensionality and the required number of RF chains, without causing substantial performance degradation [93].

The concept of B-MIMO in mm-Wave communications was initially proposed in [89]. A physically accurate computational model of the continuous aperture phased MIMO was designed and analyzed. The validation and performance of the proposed MIMO system were evaluated through prototype-based measurements, with results demonstrating close alignment with theoretical predictions. In [56] and [93], the concept of B-MIMO along with beam selection was exploited for complexity reduction in mm-Wave networks by multiplexing data onto orthogonal spatial beams. However, these B-MIMO systems are constrained by the limitation that the number of active users cannot exceed the number of available RF chains within the same time-frequency resources. To overcome the congenital limitation, the authors in [94]–[96] proposed mm-Wave B-MIMO incorporating NOMA systems. Results show that apart from enabling massive connectivity, the utilization of NOMA can further enhance the capacity limits of B-MIMO systems.

Beam selection algorithms were investigated in [58], [97]–[104]. In [97], several beam selection algorithms based on channel power were proposed for B-MIMO. These algorithms achieve near-optimal performance in mm-Wave networks while significantly reducing RF complexity. To mitigate multi-user interference and enhance EE, the authors in [98] introduced an interference-aware beam selection algorithm, while the authors in [58] developed an iterative beam selection algorithm that grabs the beam with the highest contribution for each user. These algorithms aim to select the optimal non-overlapping beams for users, thereby reducing the channel dimensionality and maximizing the network performance. In [99], the authors introduced two efficient beam selection approaches: a greedy beam selection algorithm and a maximum weight matching algorithm. These methods provide valuable insights into the development of novel beam selection strategies. In [100], a decentralized beam selection algorithm for dynamic networks was proposed, where the beam selection process is based on the exchange of location information among users, rather than being determined by the BS antenna arrays. This approach reduces the size of channel matrix that needs to be processed by the transmitter, thereby enhancing computational efficiency. To address the performance degradation due to the beam squint in wideband networks, the authors in [101] proposed a phase-shifter-aided beam selection algorithm, allowing a single RF chain to generate multiple focused-energy beams. Additionally, they integrated the proposed beam selection algorithm with beamspace precoding to optimize the sum SE. This approach effectively balances hardware cost and system performance. The authors in [102] proposed a hybrid beam selection scheme that enables multiple beam group selections to reduce quantization error. In [103], a blockwise beam selection algorithm was introduced, aiming to achieve a low-dimensional hybrid beamformer and minimize the computation of baseband processing in mm-Wave beamspace systems. While most recent research has focused on the design of beam selection algorithms, the associated computational cost has often been overlooked. In response, the authors in [104] explored the efficiency improvement of existing beam-selection algorithms using incremental and decremental QR precoders. Their findings demonstrated that the proposed algorithms significantly reduce computational complexity while achieving comparable sum SE compared to benchmark algorithms.

2.3 Optimization Techniques for MIMO Systems

MIMO system optimization is a critical challenge for enhancing cellular network performance. Various mathematical optimization techniques have been explored to improve the efficiency and effectiveness of MIMO systems [105]. Among these, FP is a widely used approach, which is particularly useful for problems characterized by the presence of fractional terms, such as SINR, SE, and EE maximization. These problems are inherently nonlinear and difficult to solve using conventional optimization methods.

Traditional FP typically focuses on single-ratio problems, where the objective function contains only one fractional term. In contrast, multi-ratio FP involves the summation of multiple fractional terms. A single-ratio FP problem is represented as

$$\begin{aligned} &\max_{\mathbf{x}} \quad \frac{A(\mathbf{x})}{B(\mathbf{x})} \\ &\text{s.t.} \quad \mathbf{x} \in \mathcal{X}, \end{aligned} \tag{2.17}$$

where $A(\mathbf{x})$ is a non-negative function: $\mathbb{R}^d \to \mathbb{R}_+$, $B(\mathbf{x})$ is a positive function: $\mathbb{R}^d \to \mathbb{R}_{++}$, $\mathcal{X} \subseteq \mathbb{R}^d$ is a non-empty constraint set, and $d \in \mathbb{N}$. The conventional approaches for solving the above problem involve Charnes-Cooper transform [106], [107] and Dinkelbach's transform [108]. However, extending these techniques to multiple-ratio FP is challenging. While these classical transforms ensure that the transformed problem and the original FP share the same optimal solution, it is not necessary to correspond the optimal value of the objective function in the transformed problem to that in the original FP. Consequently, when dealing with multiple ratios, these transforms cannot be applied independently to each ratio. Therefore, a QT inspired by Dinkelbach's transform was proposed in [109], and is represented as

$$g(\mathbf{x}, y) = 2y\sqrt{A(\mathbf{x})} - y^2 B(\mathbf{x}), \tag{2.18}$$

where y is an auxiliary variable and is updated iteratively by $y[t+1] = \frac{A(\mathbf{x}[t])}{B(\mathbf{x}[t])}$, t is the iteration index. This transform meets the essential conditions required for the multi-ratio objective function, including the decoupling of the numerator and denominator, maintaining equivalence in both the solution and the auxiliary variable, and preserving concavity. By applying the QT, typical problems including the sum-of-ratio problem, the sum-of-functions-of-ratio problem, and the max-min-ratio problem can be effectively addressed. The QT can be further extended to deal with multi-dimensional and complex problems, such as multi-antenna communication systems. Considering a multi-dimensional single-ratio FP problem:

$$\begin{aligned} \max_{\mathbf{x}} \quad & \sum_{n=1}^{N} \mathbf{a}_n^{\dagger}(\mathbf{x}) \mathbf{B}_n^{-1}(\mathbf{x}) \mathbf{a}_n(\mathbf{x}) \\ \text{s.t.} \quad & \mathbf{x} \in \mathcal{X}, \end{aligned} \tag{2.19}$$

where $\mathbf{a}_n(\mathbf{x})\colon \mathbb{C}^{d_1} \to \mathbb{C}^{d_2}$, $\mathbf{B}_n(\mathbf{x})\colon \mathbb{C}^{d_1} \to \mathbb{S}_{++}^{d_1 \times d_2}$, $\mathcal{X} \subseteq \mathbb{C}^{d_1}$, $n = 1, \cdots, N$, and $d \in \mathbb{N}$. The equivalent problem of (2.19) after applying the QT is given by

$$\max_{\mathbf{x}} \quad \sum_{n=1}^{N} \left(2\Re\left\{\gamma_n^{\dagger}\mathbf{a}_n(\mathbf{x})\right\} - \gamma_n^{\dagger}\mathbf{B}_n(\mathbf{x})\gamma_n\right)$$

$$\text{s.t.} \quad \mathbf{x} \in \mathcal{X}, \gamma_n \in \mathbb{C}^{d_2}, \tag{2.20}$$

where $\boldsymbol{\gamma} = \{\gamma_1, \cdots, \gamma_N\}$ is a collection of auxiliary variables.

The QT mentioned above serves as the fundamental technique in FP for addressing continuous optimization problems. In communication system design, the widely-used data rate function $\log(1 + SINR)$ frequently appears in user scheduling problems. To address such discrete scheduling problems, the LDT introduced in [110] facilitates the application of the subsequent quadratic transform, enabling the expression of all optimization variables in linear terms.

Considering a weighted sum-of-logarithms maximization problem:

$$\max_{\mathbf{x}} \quad \sum_{n=1}^{N} w_n \log\left(1 + \frac{A_n(\mathbf{x})}{B_n(\mathbf{x})}\right)$$

$$\text{s.t.} \quad \mathbf{x} \in \mathcal{X}, \tag{2.21}$$

where w_n is non-negative weights. The equivalent problem of (2.21) after applying the LDT is given by

$$\max_{\mathbf{x},\gamma} \quad \sum_{n=1}^{N} w_n \log(1 + \gamma_n) - \sum_{n=1}^{N} w_n \gamma_n + \underbrace{\sum_{n=1}^{N} \frac{w_n(1 + \gamma_n)A_n(\mathbf{x})}{A_n(\mathbf{x}) + B_n(\mathbf{x})}}_{\text{Sum-of-ratio term}}$$

$$\text{s.t.} \quad \mathbf{x} \in \mathcal{X}. \tag{2.22}$$

The solution $\mathbf{x}$ of problem (2.21) and (2.22) are identical, as is the optimal auxiliary variable values $\boldsymbol{\gamma}$.

Similar to the QT, the LDT technique can be extended to address the multi-dimensional and complex logarithmic FP problem as follows

$$\max_{\mathbf{x}} \quad \sum_{n=1}^{N} w_n \log\left(1 + \mathbf{a}_n^{\dagger}(\mathbf{x})\mathbf{B}_n^{-1}(\mathbf{x})\mathbf{a}_n(\mathbf{x})\right)$$

$$\text{s.t.} \quad \mathbf{x} \in \mathcal{X}. \tag{2.23}$$

The equivalent problem of (2.23) after applying the LDT is given by

$$\max_{\mathbf{x},\boldsymbol{\gamma}} \quad \sum_{n=1}^{N} w_n \log\left(1 + \gamma_n\right) - \sum_{n=1}^{N} w_n \gamma_n$$

$$+ \sum_{n=1}^{N} w_n (1 + \gamma_n)\mathbf{a}_n^{\dagger}(\mathbf{x})\left(\mathbf{a}_n(\mathbf{x})\mathbf{a}_n^{\dagger}(\mathbf{x}) + \mathbf{B}_n(\mathbf{x})\right)^{-1}\mathbf{a}_n(\mathbf{x})$$

$$\text{s.t.} \quad \mathbf{x} \in \mathcal{X}, \boldsymbol{\gamma}_n \in \mathbb{C}^{d_2}. \tag{2.24}$$

With the introduction of the QT and the LDT, FP has been applied to various wireless communication system design scenarios, such as MIMO systems [111]–[113], hybrid beamforming [114], [115], satellite systems [116], [117], edge-cloud computing [118]–[120], unmanned aerial vehicles [121]–[123], and intelligent reflecting surfaces or reconfigurable intelligent surfaces [124]–[127]. In general, when a practical problem can be formulated as the maximization of a sum of positive ratios, these transform techniques consistently provide efficient algorithmic solutions.

The previously presented FP techniques are effective for maximizing or minimizing ratio terms. However, they generally cannot convert one case into the other. To address this limitation, the authors in [128] extended the QT to min-FP case. They further integrated this new min-FP method with the existing max-FP method into a unified framework for the mixed max-and-min FP problem, which can simultaneously maximize SINR while minimizing the eavesdropper.

2.4 HTCN Deployment

In traditional HMCNs, the majority of the MBSs are equipped at the top of buildings with high transmit power and developed as points on hexagonal lattices. However, with the exponential growth in data traffic demand within 5G mobile communication systems, the need to increase the number of MBSs has become essential to ensure sufficient service coverage for UEs in all areas. This results in a proportional increase in energy consumption, rendering the HMCN economically and ecologically infeasible. To enhance the EE, the HTCN has evolved from the HMCN by incorporating massive heterogeneous characteristics into cellular network deployments. This evolution provides additional wireless coverage and reduces the cost of MBSs in various scenarios, including both outdoor and indoor environments. The architecture of the HTCN was proposed in 3GPP Release 12 [129]. A typical HTCN deployment includes macro cells, micro cells, pico cells, and femto cells. The network types are classified with respect to the coverage areas and application scenarios. BSs in macro-cell networks can transmit high power, which provides a wide coverage area, where the cell radius is typically on the order of 1 km or more. Micro-cell BSs are always deployed in densely urban areas and cover the smaller cell coverage area with a radius between 200 m to 1 km. BSs in pico-cell networks always install omnidirectional antennas and provide lower transmit power that serves the indoor users located in a building area. APs in the femto-cell network give the lowest cost and power consumption, which is suitable for small-area deployments such as homes and offices.

2.4.1 Interference in HTCNs

The high network density in the HTCN leads to an increase in the SE accompanied by a corresponding rise in interference levels. The inter-cell interference suffered by a user occurs due to the signal interaction among the target cell and adjacent cells. It is either because of the same frequency spectrum utilization, which is referred to as co-channel interference (CCI), or the overlapping among channels from different transmitters in adjacent cells, which is referred to as adjacent channel interference (ACI) [130].

CCI is a form of traffic congestion that occurs due to the limitation of resources, where the same frequency spectrum is shared by multiple cells simultaneously. A conventional approach to mitigate CCI is interference coordination, which is based on frequency reuse [131]. The entire frequency spectrum is divided into several non-overlapping sub-bands, which are allocated to different cells. Mitigating the impact of CCI is achieved by carefully planning the frequency sub-bands and deploying cells in an optimal manner.

ACI is mainly attributed to the non-ideal receiver filter. In multi-cell networks, a frequency band makes it easier to leak energy on adjacent frequency bands within the filter pass band of the receiver equipment in the same geographical location. The out-of-band emissions might be increased if similar frequency channels are close to each other in a communication system. The following approaches can be chosen to reduce ACI: select appropriate filters in the receiver equipment, assign channels carefully, design antenna radiation patterns, and manage cell deployments [132].

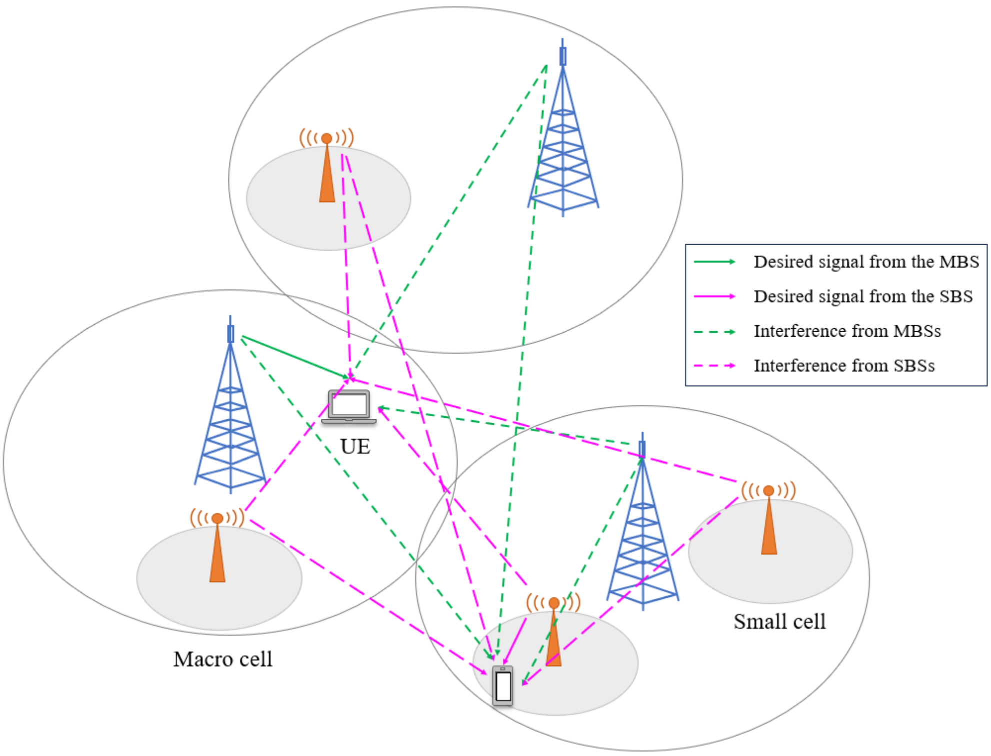

Fig. 2.6 A two-tier HTCN architecture: solid arrows denote desired signals; dashed arrows denote co-tier and cross-tier interference.

The inter-cell interference for a UE associated with an MBS or an SBS in an HTCN is composed of co-tier interference and cross-tier interference, as illustrated in Fig. 2.6. The co-tier interference denotes the interference occurring between the UE and BSs within the same network tier. The cross-tier interference denotes the interference experienced from the different network tiers. The SINR of the typical UE served by an MBS or an SBS is expressed as

$$SINR_{\mathrm{M}} = \frac{P_{\mathrm{M}}}{\sum_{m\in\Phi_{\mathrm{M}}\backslash\{M_0\}} I_m + \sum_{s\in\Phi_{\mathrm{S}}} I_s + \sigma^2}, \tag{2.25}$$

$$SINR_{\mathrm{S}} = \frac{P_{\mathrm{S}}}{\sum_{s\in\Phi_{\mathrm{S}}\backslash\{S_0\}} I_s + \sum_{m\in\Phi_{\mathrm{M}}} I_m + \sigma^2}, \tag{2.26}$$

where P_{M} and P_{S} represent signals of the typical user received from the serving MBS or SBS; Φ_{M} and Φ_{S} represent the group of MBSs and SBSs, respectively; M_0 and S_0 represent the serving MBS and SBS, respectively; I and σ represent interference and noise, respectively.

Some techniques were proposed to suppress these two types of inter-interference in current studies. The research studies in [133]–[135] focused on managing cross-tier interference. The authors in [133] proposed a distributed resource allocation scheme in a two-tier orthogonal frequency-division multiple access (OFDMA)-based HTCN to deal with the SBS interference. The proposed scheme leverages the CSI of UEs that are adjacent to an MBS, enabling the SBS to predict and constrain the subchannels accordingly. The results show that the SE can be maximized by letting the SBS fully reuse the estimating subchannels from neighboring UEs. The resource allocation scheme, along with the MBS transmit power, was also investigated in [134]. In [135], the cross-tier interference was mitigated through an annealing algorithm and a minimum distance maximization algorithm with only the locally overhead CSI required. The management for both co-tier interference and cross-tier interference is researched in [136]–[139]. In [137], a frequency reuse strategy was implemented by sectorizing the macrocell coverage area into three sections and three layers, and dividing the frequency spectrum into seven sub-bands which could be distributed among the entire HTCN. The authors in [138] applied the resource allocation scheme on a 3-tier HTCN to alleviate the small-cell interference by grouping the lowest-tier cells. This scheme effectively mitigates inter-cell interference and improves the network throughput in a fully distributed resource management manner, but the high density of SBSs leads to an increase in energy consumption.

2.4.2 User Association

With the distribution of multiple types of small cells, the gaps among larger-size cells can be filled by offloading the traffic to smaller-size cells to achieve load balancing and improve service quality. However, due to the transmit power disparity between MBSs and SBSs, load balancing cannot be achieved for a satisfying performance. To cope with this problem, the concept of biasing technique was introduced in 3GPP Release 10 [140], where the user association is artificially determined by the biasing factor. It aims to extend the cell range and make the small cells more attractive for UEs to suppress the traffic in the cell edge.

Various user association schemes lead to different levels of service quality. It can be selected according to the HTCN deployment and performance requirements. UEs in the overlapping coverage area of multiple tiers can be served by the antenna of any tier with respect to the user association scheme. The authors in [141] considered the coverage probability and average SE of the HTCN under three example user association schemes:

(i). Maximum averaged biased received power scheme [142], where the UE connects the BS that provides the strongest average biased received power;

(ii). Minimum biased transmission distance scheme [143], where the UE connects the BS with the biased minimum distance;

(iii). Maximum instantaneous SINR scheme [19], where the UE connects the BS that provides the highest instantaneous SINR.

The benefits of the range expansion in HTCNs were investigated in [144], where the system capacity can be enhanced by offloading the macro-cell UEs to small cells. The authors in [142] proposed an analytical K-tier downlink HTCN model with a flexible cell association strategy to investigate the impact of biasing on HTCN long-term averaged performance. The results show that expanding the small-cell region enhances the outage probability but deteriorates the ergodic rate of the HTCN, which means UEs in the range expansion area who are forced to be associated with SBSs incur strong interference from the co-tier MBS for a high biasing factor. The load balancing problem was investigated in [145] and [146]. The analysis shows that light-loaded SBSs can enhance the coverage probability and data rates, while fullyloaded SBSs are extremely pessimistic about the data rates of cell-edge UEs because of the heavy congestion of these UEs. Only UEs that are close to MBSs can be prioritized to receive the high data rates. This problem was addressed in [147] with a low-complexity load-aware user association approach and distributed algorithm to optimize the load-balancing problem. The distributed algorithm can converge to a near-optimal solution that is linear to the number of BSs and UEs. The authors combined the algorithm with the load-aware user association approach to evaluate the impact of BS density and transmit power on the SINR biasing factor and user data rate biasing factor. Authors in [148] also proposed a novel real-time dynamic user association approach that takes into account UEs' mobility and traffic dynamics, along with a location-based interference mitigation algorithm for the overload problem. The dynamic user association does not depend on the specific biasing factor. In this user association approach, UEs initially associate with BSs according to the maximum SINR. After that, UEs in the over-loaded area are redistributed to relieve the load of SBSs. The authors in [149] optimized the biasing factor for an inter radio access technology offloading in a K-tier HTCN utilizing numerical evaluations. They found that there exists an optimum traffic-offloading percentage value to maximize the rate coverage.

Some recent studies have integrated user association with other techniques to jointly improve the performance of NTCN [150]–[154]. User association was jointly optimized with power control in [152] to maximize the weighted sum of long-term user SE and mitigate network interference and energy consumption. In [153], user association was considered together with the resource allocation to mitigate both uplink and downlink interference and achieve a load balancing in the HTCN. In [154], the authors proposed a distributed optimization scheme based on user association and the coordinated multi-point transmission technique to deal with the cell-specific offset problem.

2.4.3 Mathematical Models for Cellular Networks

Due to the irregularity and denseness of the multi-tier infrastructure development, system modeling and evaluation become more complicated in HTCNs than in HMCNs. The SG approach plays a crucial role in providing a cohesive mathematical framework to model different kinds of wireless networks by capturing the spatial randomness in networks. Because of its natural extensibility in describing various sources of uncertainty, such as BSs and path loss, it enables the derivation of closed-form expressions in network analysis. Compared with computationally intensive simulations, this makes the analysis more rigorous and tractable, which is beneficial for providing useful practical design guidelines.

In cellular network modeling, the SG model is quite different from the most frequently used idealized HG model. The studies conducted in [155]–[157] introduced the architectural framework of the network by SG models and examined the performance of cellular networks utilizing SG in comparison to traditional regular HG models. These studies demonstrated the irregular topology inherent in SG, which enables random variations in network configurations. Authors in [155] proposed general models and some special cases for SINR in cellular networks utilizing SG. Rather than assuming the deterministic placement for BSs in HG, BSs in SG are always distributed by homogeneous Poisson point processes (HPPPs). Comparing the results from HG-based simulations and SG-based actual BS deployment in urban areas, they found that the SINR of a UE is upper bounded by the HG model, and lower bounded by the SG model about equally accurate and more tractable. In [156], an accurate point process was proposed to present the actual spatial patterns of BSs by SG spatial patterns modeling. The authors also examined the accuracy and tractability of the lower bound of the SINR using the SG model. The authors in [157] exhibited a mathematical Poisson-convergence result to demonstrate that the SINR of any UE in the HG network can be perceived by that of a typical UE in the SG network with an equivalent Poisson process when the shadowing is quite strong.

2.5 Summary

This chapter comprises several key overview sections, including FD-MIMO, 3D channel model, 3D beamforming, mmWave MIMO beamforming, B-MIMO, Optimization techniques for MIMO systems, interference management in HTCN, user association, and mathematical network framework models. These sections provide a comprehensive understanding of the relevant topics and serve as a foundation for the subsequent research in the following chapters.

In the reviews of 3D beamforming in FD-MIMO systems, the properties of 3D beamforming were summarized. The configuration and advantages of the planar antenna array in FD-MIMO systems are presented, highlighting its benefits over the conventional linear antenna array, followed by the introduction of the 3D channel model. For the 3D beamforming technique, three types of beamformer architectures are first exhibited, and some initial works on 3D beamforming are reviewed. Two kinds of radiation pattern modeling approaches are introduced in detail. The performance of these approaches is compared to demonstrate their effectiveness and feasibility. By conducting a comparative analysis, the practical implementation and benefits of each approach can be ascertained. After the introduction of two types of antenna tilting schemes, several studies on interference management by 3D beamforming are reviewed.

In the reviews of mm-Wave MIMO beamforming, the benefits that mm-Wave technology brings to MIMO systems are studied. The high frequency of mm-Wave improves the MIMO system capacity and signal quality, and enhances the realization of beamforming. However, this feature brings some challenges that require to be addressed during channel modeling such as high path loss and propagation for signals, hardware complexity, and interference management. B-MIMO is one of the techniques used to reduce hardware complexity, facilitated by the use of beam selection algorithms.

In the reviews of optimization techniques for MIMO systems, FP is presented, starting with an overview of single-ratio, multi-ratio, and multidimension FP optimization problems. The QT and LDT techniques, which can be applied to these FP problems, are introduced to simplify the computation of complex optimization tasks. Additionally, several studies on the application of FP techniques in wireless communication system design are reviewed.

In the reviews of HTCN deployment, some techniques that deal with the complications encountered in HTCNs are explored to provide a foundation for further research on 3D beamforming in HTCNs. In the aspect of interference management, the constituents of interference that a typical UE incurred are considered, which include co-tier interference and cross-tier interference. In order to achieve load balancing among multiple tiers, the user association technique is discussed regarding the user association schemes and some research on analyzing and optimizing the biasing factor. Finally, the SG mathematical network framework model is introduced to better capture the irregularity and density of HTCNs.

Chapter 3

Joint Impact of BS Height and Downtilt on Downlink SE in Mm-Wave Networks with 3D LSAAs

3.1 Introduction

With the fast growth of mobile devices, the unprecedented data volume leads to increasing demands on capacity in wireless networks. 3D MIMO is a promising 5G technology that allows a large number of antenna elements stacked in the 3D LSAA at the BS to enhance the network capacity [158]. The mm-Wave system can achieve high rates due to the large bandwidth channels which use the spectrum between 30 GHz to 300 GHz [159]. Although the high frequency of mm-Wave gives rise to the propagation attenuation, the small wavelength enables employing more radiating antenna elements in a single radome, which can not only mitigate the propagation loss but also realize highly directional beamforming [65], [72]. In a cellular network, inter-cell interference is a significant factor that limits the user throughput. One technique to mitigate it is 3D beamforming. Compared to two-dimensional beamforming, which only adjusts beams in the horizontal plane, 3D beamforming leveraging the narrow beam from a mm-Wave antenna array is able to adjust the elevation angle of the BS antenna pattern. Thereby, the BS radiation pattern can be steered to an intended user, thus enhancing the desired signal while suppressing interference to other users [7], [158].

Recently, vertical beamforming has been studied to improve the performance of cellular networks [11], [18], [63], [160], [161]. In [11], the authors derived the optimal BS antenna tilt and provided the analytical expression of the average SE for an active user in a downlink MISO single-cell network. In [63] and [160], the authors studied the antenna downtilt for a downlink hexagonal cellular network and derived the average SE per user, where the height of BS was fixed. In [161], the authors investigated the relationship between the antenna tilt and the coverage probability, where the BS antenna height was only considered on specific working points but was not optimized to maximize the coverage probability. The cell average SE for a mm-Wave network was derived in [18] by considering the downtilt and BS antenna height, while the optimal BS antenna height was not obtained and the inter-cell interference was not taken into account.

It is noted that the above existing works on optimizing BS antenna downtilt set the BS antenna height with specific values. However, the BS antenna height determines the 3D distance between the transmitter and the receiver. It has been shown in [161] that different BS antenna heights with the corresponding optimal BS antenna downtilts lead to different performances for a 3D mm-Wave network, indicating that the BS antenna height cannot be ignored in the 3D LSAA design. The joint impact of BS antenna height and downtilt on the downlink of a mm-Wave network with 3D LSAA has not been sufficiently studied.

In this chapter, the downlink SE per user is enhanced across all possible locations within the cell coverage area by jointly optimizing the BS antenna height and downtilt for 3D LSAA downlink transmission in a mm-Wave cellular network. Without loss of generality, attention is directed toward three adjacent clusters, incorporating all potential inter-cell interference. An analytical expression is first derived for the downlink SE per user averaged over the cell coverage area, as a function of the BS antenna height and downtilt. To compute the derived average downlink SE, a novel numerical approach is proposed based on the Riemann sum approximation [162] to approximately calculate the integral in the expression. Therein, the coverage area is divided into equilateral triangle grids to approximate the continuous distribution of user positions by discretizing user positions. The accuracy of the proposed discrete approximation for the average downlink SE is assessed by simulation. The numerical analysis shows that an optimal pair of BS antenna height and downtilt values that maximize the cell-averaged downlink SE can be obtained via a quick numerical search.

The remainder of this chapter is organized as follows. In Section 3.2, a multicell 3D LSAA system model is presented. In Section 3.3, the exact and approximate expressions for the cell-averaged downlink SE are derived. The simulation and analytical results are presented in Section 3.4. Finally, this chapter is summarized in Section 3.5.

3.2 System Model

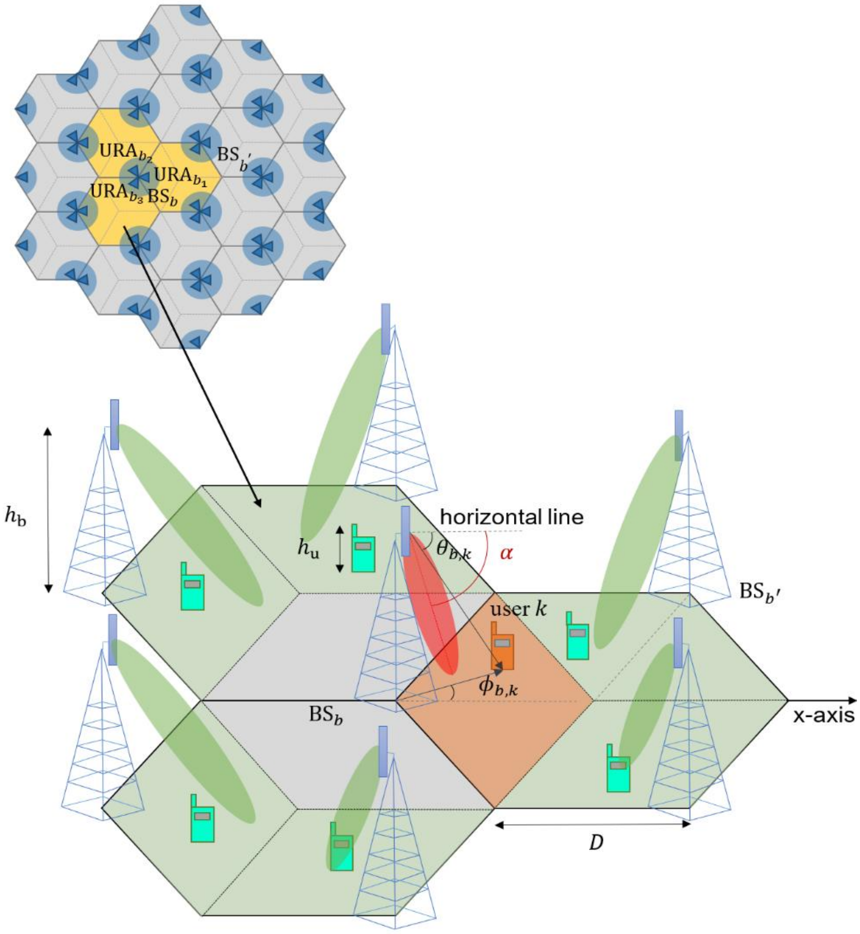

Fig. 3.1 A network consisting of three hexagonal clusters, each including three adjacent cells.

Considering the downlink transmission in a mm-Wave network consisting of 19 hexagonal clusters, each cluster contains 3 rhombic cells with a side length of D, as shown in Fig. 3.1. In each cell, a BS is located at the height of h_{b} above the ground at a vertex. The BS is equipped with three uniform rectangular arrays (URAs) of dimension $N_{\mathrm{t}} = N_{\mathrm{az}} \times N_{\mathrm{el}}$, where N_{az} and N_{el} are the number of antennas in the azimuth and elevation dimensions of the array plane, respectively. Users are uniformly distributed in the network coverage area at the height of h_{u} ($h_{\mathrm{u}} < h_{\mathrm{b}}$). For simplicity, all user devices are assumed to be equipped with a single antenna. In a given time-frequency resource block, a user is associated with the nearest BS, which is called home BS.

Considering a typical user k served by its home BS b, to capture interference from other cells that affect the intended cell containing user k, a network consisting of three adjacent clusters is focused on. Let the home BS b locate at the origin, the position of the typical user k is denoted by $(x_{b,k}, y_{b,k})$. In the illustrated network, interfering BSs are indexed by $b' = 1, \dots, B-1$. Assuming that each cell contains one user, users associated with BS b' are indexed by $k' = 1, \dots, K-1$, and $K = B$. The coverage area in the horizontal plane for each cell spans an angular range of 120°, implying that all other BSs within these 3 clusters contribute interference to the typical user.

3.2.1 Channel Model

In order to simplify the system model, a typical LOS propagation scenario is considered. The downlink channel vector between BS b and its associated user k is denoted by $\boldsymbol{h}_{b,k} \in \mathbb{C}^{N_{\mathrm{t}} \times 1}$ and expressed as [93]

$$\boldsymbol{h}_{b,k} = \rho_{b,k}(\phi_{b,k}, \theta_{b,k})\boldsymbol{a}(\phi_{b,k}, \theta_{b,k}), \tag{3.1}$$

where $\rho_{b,k}(\phi_{b,k}, \theta_{b,k})$ denotes the complex path loss from BS b to user k, and is given by [56]

$$\rho_{b,k}(\phi_{b,k}, \theta_{b,k}) = |\rho_{b,k}| e^{j\varphi} = \frac{\lambda e^{j\varphi}}{4\pi} \sqrt{\frac{G_{b,k}(\phi_{b,k}, \theta_{b.k}, \alpha)}{r_{b,k}^2 + (h_{\mathrm{b}} - h_{\mathrm{u}})^2}}, \tag{3.2}$$

where $|\rho_{b,k}|$ is the amplitude of the path loss which can be calculated via Friis transmission formula [163]; λ denotes the wavelength; φ indicates the phase, which has the uniform distribution on $(0,2\pi)$; $r_{b,k}$ represents the distance between BS b and user k in the ground plane. The user antenna is assumed to have an omni-directional antenna pattern. The antenna gain

$G_{b,k}(\phi_{b,k}, \theta_{b,k}, \alpha)$ from any antenna element in the URA at BS b to user k is written in dBi scale as [53]

$$G_{b,k}^{\mathrm{dBi}}(\phi_{b,k}, \theta_{b,k}, \alpha) = -\min\left\{\begin{bmatrix} \min\left(12\left(\frac{\phi_{b,k}}{\phi_{3\mathrm{dB}}}\right)^2, SLL_{\mathrm{az}}\right) \\ +\min\left(12\left(\frac{\theta_{b,k}-\alpha}{\theta_{3\mathrm{dB}}}\right)^2, SLL_{\mathrm{el}}\right) \end{bmatrix}, SLL_{\mathrm{az}}\right\}, \quad (3.3)$$

where α denotes the electrical tilt of antennas at a BS, which is the angle between the ground plane and the peak of the main beam of each antenna; $\phi_{b,k}$ and $\theta_{b,k}$ denote the physical azimuth and elevation AoD at user k, respectively, and are obtained by $\phi_{b,k} = \tan^{-1}(y_{b,k}/x_{b,k})$ and $\theta_{b,k} = \tan^{-1}\left(\frac{h_{\mathrm{b}}-h_{\mathrm{u}}}{\sqrt{x_{b,k}^2+y_{b,k}^2}}\right)$. Furthermore, $\phi_{3\mathrm{dB}}$ and $\theta_{3\mathrm{dB}}$ are the HPBW in the azimuth and elevation dimensions, respectively, and SLL_{az} and SLL_{el} represent the maximum attenuation in the horizontal and vertical planes, respectively.

In addition, $\boldsymbol{a}(\phi_{b,k}, \theta_{b,k})$ in (3.1) stands for the 2D transmit array beam steering vector. The analog beamforming is applied to control the direction of beam by adjusting the phase shift. For the URA at BS b with N_{t} antenna elements, the beam steering vector can be expressed as [90]

$$\boldsymbol{a}(\phi_{b,k}, \theta_{b,k}) = \frac{1}{\sqrt{N_{\mathrm{t}}}}\left[1, \cdots, e^{-j2\pi(m_{\mathrm{az}}\psi_{\mathrm{az}}+m_{\mathrm{el}}\psi_{\mathrm{el}})}, \cdots, e^{-j2\pi((N_{\mathrm{az}}-1)\psi_{\mathrm{az}}+(N_{\mathrm{el}}-1)\psi_{\mathrm{el}})}\right]^{\mathrm{T}}, \quad (3.4)$$

where $m_{\mathrm{az}} = 0,1, \dots, N_{\mathrm{az}} - 1$, and $m_{\mathrm{el}} = 0,1, \dots, N_{\mathrm{el}} - 1$ are the antenna indices. Moreover, $\psi_{\mathrm{az}} = \frac{d}{\lambda}\sin\phi_{b,k}\sin\theta_{b,k}$ and $\psi_{\mathrm{el}} = \frac{d}{\lambda}\cos\theta_{b,k}$ represent the spatial frequencies ranging over $\left[-\frac{d}{\lambda}, \frac{d}{\lambda}\right]$, where d is the antenna spacing which should not be larger than half-wavelength [164].

3.2.2 Received Signal and SINR

The beam from each URA is assumed to have the same direction with an AoD between the URA and its serving user. The optimal beamforming vector from the URA of BS b to user k corresponding to the optimal AoD is given by $\boldsymbol{\omega}_{b,k} = \boldsymbol{a}\left(\phi'_{b,k}, \theta'_{b,k}\right)$. The received signal at user k served by its home BS b is expressed as

$$r_k = \boldsymbol{h}_{b,k}^{\mathrm{H}} \boldsymbol{\omega}_{b,k} s_{b,k} + \sum_{\substack{b'=1 \\ k'=b'}}^{B-1} \boldsymbol{h}_{b',k}^{\mathrm{H}} \boldsymbol{\omega}_{b',k'} s_{b',k'} + n, \tag{3.5}$$

where $s_{b,k}$ is the data symbol from BS b to user k, and is subjected to the power constraint $P_{\mathrm{t}} = \mathbb{E}\left[\left\|\boldsymbol{\omega}_{b,k} s_{b,k}\right\|^2\right]$; n denotes the additive white Gaussian noise (AWGN) following $\mathcal{CN}(0, \sigma_n^2)$. It is assumed that all BSs transmit to users at the same power level. Given perfect CSI regarding the AoD between each BS and its respective user, the SINR expression for user k is given by

$$\begin{aligned}
\eta_k &= \frac{P_{\mathrm{t}} \left| \boldsymbol{h}_{b,k}^{\mathrm{H}} \boldsymbol{\omega}_{b,k} \right|^2}{P_{\mathrm{t}} \sum_{\substack{b'=1 \\ k'=b'}}^{B-1} \left| \boldsymbol{h}_{b',k}^{\mathrm{H}} \boldsymbol{\omega}_{b',k'} \right|^2 + \sigma_n^2} \\
&= \frac{P_{\mathrm{t}} \rho_{b,k}^2(\phi_{b,k}, \theta_{b,k}) \left| \boldsymbol{a}^{\mathrm{H}}(\phi_{b,k}, \theta_{b,k}) \boldsymbol{a}(\phi'_{b,k}, \theta'_{b,k}) \right|^2}{P_{\mathrm{t}} \sum_{\substack{b'=1 \\ k'=b'}}^{B-1} \rho_{b',k}^2(\phi_{b',k}, \theta_{b',k}) \left| \boldsymbol{a}^{\mathrm{H}}(\phi_{b',k}, \theta_{b',k}) \boldsymbol{a}(\phi'_{b',k'}, \theta'_{b',k'}) \right|^2 + \sigma_n^2}.
\end{aligned} \tag{3.6}$$

Based on the optimal steering vector, the product of channel gain and beamforming gain of the URA at BS b in (3.6) can be expended as

$$\begin{aligned}\left|\boldsymbol{h}_{b,k}^{\mathrm{H}}\boldsymbol{\omega}_{b,k}\right|^2 &= \rho_{b,k}^2\left(\phi_{b,k},\theta_{b,k}\right)\left|\boldsymbol{a}^{\mathrm{H}}\left(\phi_{b,k},\theta_{b,k}\right)\boldsymbol{a}\left(\phi_{b,k}',\theta_{b,k}'\right)\right|^2 \\ &= \frac{\rho_{b,k}^2\left(\phi_{b,k},\theta_{b,k}\right)}{N_{\mathrm{t}}^2}\left|\sum_{m_{\mathrm{az}}}^{N_{\mathrm{az}}-1}\sum_{m_{\mathrm{el}}}^{N_{\mathrm{el}}-1} e^{-j\frac{2\pi d}{\lambda}m_{\mathrm{az}}c_{b,k}^{\mathrm{az}}}e^{-j\frac{2\pi d}{\lambda}m_{\mathrm{el}}c_{b,k}^{\mathrm{el}}}\right|^2 \\ &= \frac{\rho_{b,k}^2\left(\phi_{b,k},\theta_{b,k}\right)}{N_{\mathrm{t}}^2}\frac{\sin^2\left(\frac{N_{\mathrm{az}}\pi d}{\lambda}c_{b,k}^{\mathrm{az}}\right)}{\sin^2\left(\frac{\pi d}{\lambda}c_{b,k}^{\mathrm{az}}\right)}\frac{\sin^2\left(\frac{N_{\mathrm{el}}\pi d}{\lambda}c_{b,k}^{\mathrm{el}}\right)}{\sin^2\left(\frac{\pi d}{\lambda}c_{b,k}^{\mathrm{el}}\right)},\end{aligned} \tag{3.7}$$

where $c_{b,k}$ represents the correlation coefficient between the transmit array beam steering vector and the optimal beamforming vector for user k. This coefficient is separately for the azimuth and elevation dimensions as follows

$$c_{b,k}^{\mathrm{az}} = \sin\phi_{b,k}'\sin\theta_{b,k}' - \sin\phi_{b,k}\sin\theta_{b,k}, \tag{3.8}$$

$$c_{b,k}^{\mathrm{el}} = \cos\theta_{b,k}' - \cos\theta_{b,k}. \tag{3.9}$$

3.3 Cell-averaged Downlink SE

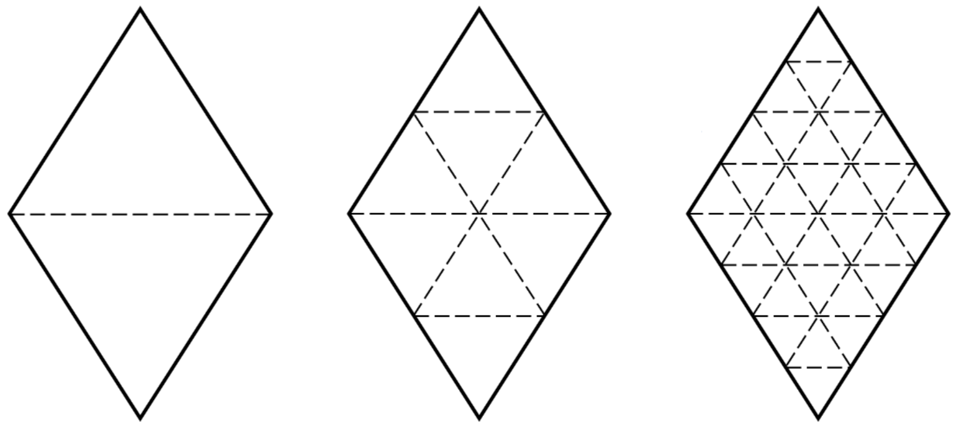

(a) 2 portions (b) 8 portions (c) 32 portions

Fig. 3.2 Division of a sample cell with 2, 8, and 32 equilateral triangles.

To determine the optimal BS antenna height and antenna downtilt, and to apply these parameters uniformly across the entire typical network irrespective of users' position, it is necessary to calculate the downlink SE per user at all possible positions within the network coverage area. As $\phi_{b,k}$ and $\theta_{b,k}$ are both derived from $x_{b,k}$ and $y_{b,k}$, based on the system model defined in Section 3.2, the expression of cell-averaged downlink SE can be expressed according to Shannon's formula as

$$\begin{aligned}\bar{R}_k &= \mathbb{E}_{x,y}[C_k] = \mathbb{E}_{x,y}[\log_2(1+\eta_k)] \\ &= \int_{y_B}\int_{x_B}\cdots\int_{y_1}\int_{x_1}\log_2\big(1+\eta_k(x_1,y_1,\dots,x_B,y_B)\big) \\ &\times\prod_{b=1}^{B} f_{x,y}(x_b,y_b)dx_1dy_1\dots dx_Bdy_B,\end{aligned} \tag{3.10}$$

where C_k is the SE for user k, and $f_{x,y}(x_b,y_b)$ denotes the joint probability density function (PDF) of the random variable x_b and y_b for the cell served by BS b. When users are uniformly distributed, and the elements of the sequence $x_1,y_1,\dots,x_B,y_B$ are independent and identically distributed (i.i.d.), $f_{x,y}(x_b,y_b)$ is constant and of finite support. Due to the complexity of solving the $2B$-tuple integral in (3.10), a numerical approach based on the Riemann sum approximation method is proposed. This method approximates the integral by generating a large number of discrete sample user positions in place of continuous user positions. Firstly, user positions in each cell area are divided with a fine grid. The rhombic cell area is uniformly divided into 2, 8, and 32 equilateral triangles, respectively, using the bisection and quartering method, as illustrated in Fig. 3.2. Three sample user positions are chosen via equally spaced subdivisions in each grid. Secondly, the user SE for each sample position is calculated with the derived expressions above. The average downlink SE for grid g including three sample users is given by

$$\bar{C}_{k_g} = \frac{\Delta S}{3}\left(C_{k_{g,1}} + C_{k_{g,2}} + C_{k_{g,3}}\right), \tag{3.11}$$

where ΔS denotes the area of the grid, and $\left[C_{k_{g,i}}\right]_{i=1,2,3}$ are SEs for sample user positions in grid g. Each pair of integral $\int_{y_b}\int_{x_b} C_k f_{x,y}(x_b, y_b) dx_b dy_b$ in (3.10) is approximated by $\sum_{g=1}^{G} \bar{C}_{k_g} f_{x,y}(x_b, y_b)$, where G is the number of grids in each cell.

3.4 Numerical Results

In this section, the optimal BS antenna height and antenna downtilt are obtained by applying the discrete approximation to the analytical expression for the cell-averaged downlink SE. Monte Carlo simulations are conducted to evaluate the accuracy of the proposed approximation described in Section 3.3. The simulation parameters are outlined in Table 3.1.

Table 3.1 Simulation Settings

Parameter	**Value**
Cell radius, D	15 m
User height, h_{u}	1.5 m
Number of transmit antennas at a URA in azimuth dimension, N_{az}	8
Number of transmit antennas at a URA in elevation dimension, N_{el}	16
Number of receive antennas at a user	1
Operating frequency, $1/\lambda$	80 GHz
Transmit signal-to-noise ratio (SNR), $P_{\mathrm{t}}/\sigma_n^2$	100 dB
Horizontal HPBW, $\varphi_{3\mathrm{dB}}$	65°

Vertical HPBW, $\theta_{3\mathrm{dB}}$	35°
Horizontal SLL, SLL_{az}	25 dB
Vertical SLL, SLL_{el}	20 dB

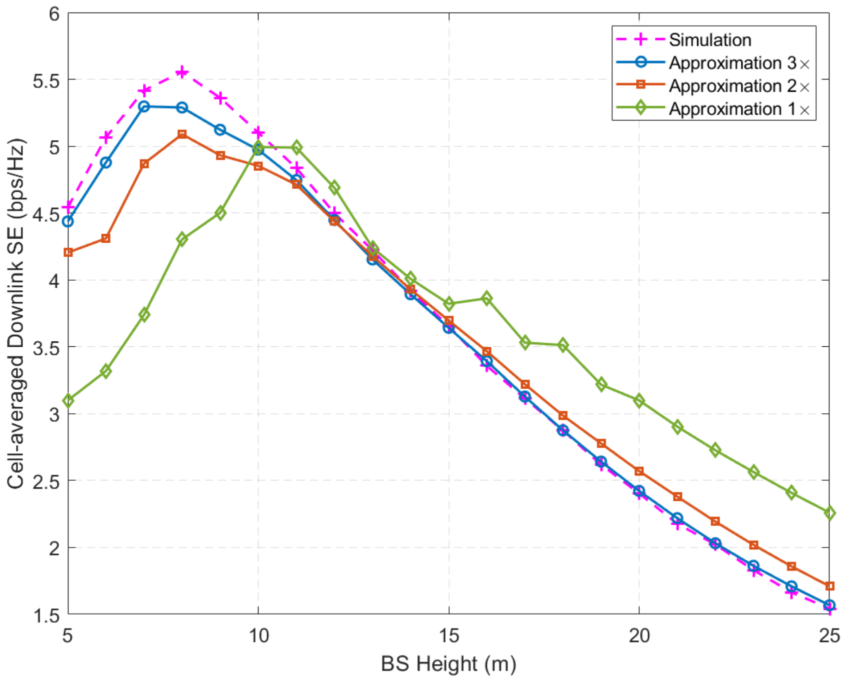

Fig. 3.3 Approximated and simulated cell-averaged downlink SE versus different BS antenna heights for the BS downtilt of 0.5 rad.

The cell-averaged downlink SE for the model system is first evaluated with varying BS antenna heights. Fig. 3.3 shows the average SE for the user in the typical cell versus the BS antenna height of BS antenna downtilt $\alpha = 0.5$ rad (28.65°). Approximate analytical curves are computed by the discrete approximation with 2, 8, and 32 portions, respectively. These three kinds of partitions are presented by approximation 1×, approximation 2×, and approximation 3×, respectively in the figure. The simulated curve is obtained via averaging the instantaneous SE for the target user over 5000 independent random realizations. It is demonstrated that the 32-portion result aligns more closely with the simulation results compared to other partitioning methods. This is attributed to the finer grid, which increases the number of integral steps and produces a more accurate approximation. A slight discrepancy is observed between the approximation result using the 3× method and the simulation result, particularly when the cell-averaged downlink SE peaks at a given BS downtilt. This mismatch can be attributed to the grid area being insufficiently fine.

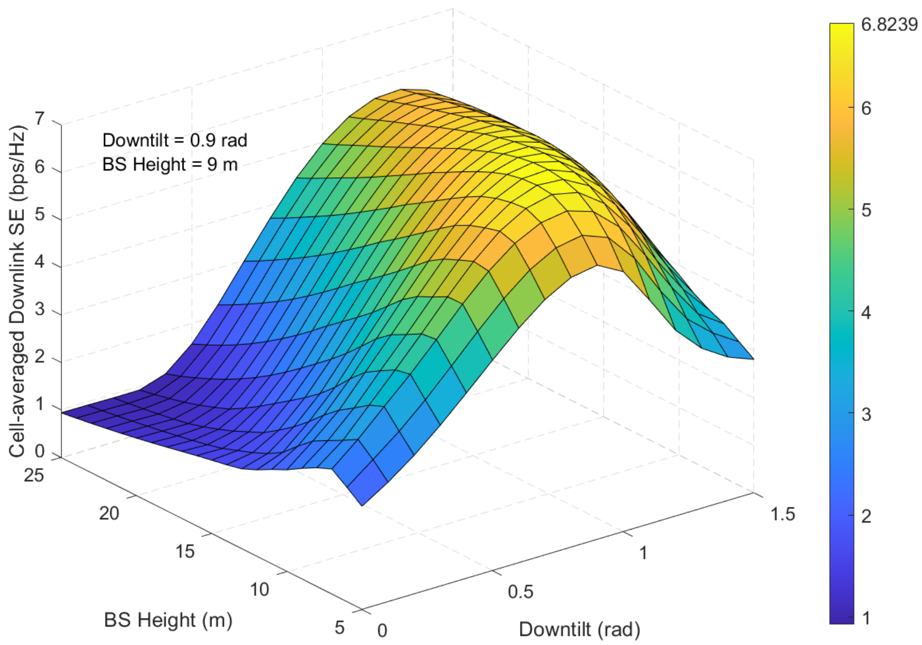

(a) Approximation 3×

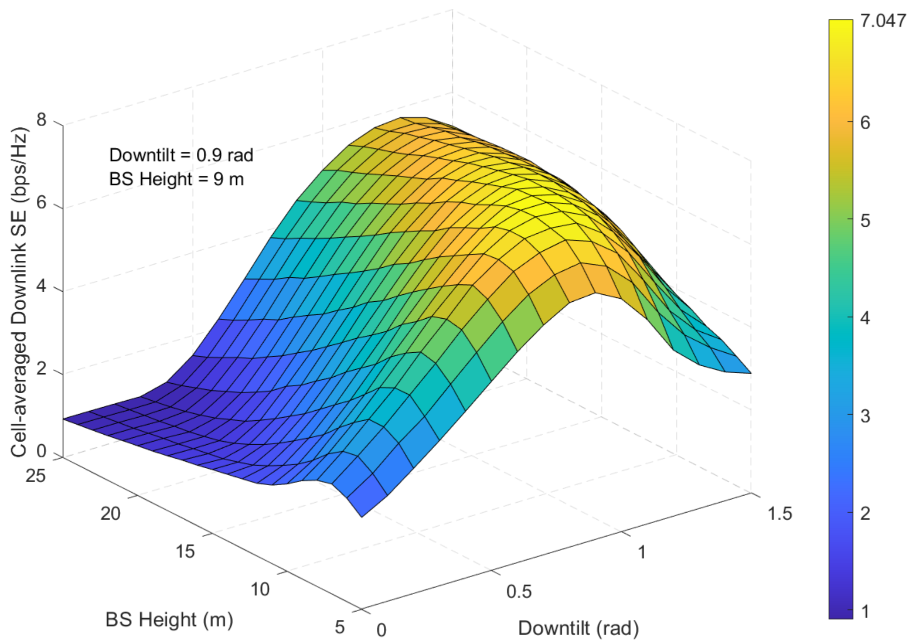

(b) Simulation

Fig. 3.4 Cell-averaged downlink SE against BS antenna height and BS downtilt obtained from the discrete approximation and simulation.

To identify the optimal BS antenna height and downtilt that maximize the cell-averaged downlink SE, cell-averaged downlink SE surface versus the BS antenna height and downtilt is presented in Fig. 3.4. It is observed that a peak value of cell-averaged downlink SE is achieved when BS antenna height h_{b} $= 9$ m and downtilt $\alpha = 0.9$ rad (51.57°). The cell-averaged downlink SE decreases out of the peak since the path loss increases with the growth of the BS antenna height. Moreover, inter-cell interference arises from the decrease of the downtilt because large antenna gains from interfering cells have an impact on the typical cell. In addition, although a large downtilt can provide adequate protection for the intended user from inter-cell interference, the cell edge user is hard to attain an acceptable user SE.

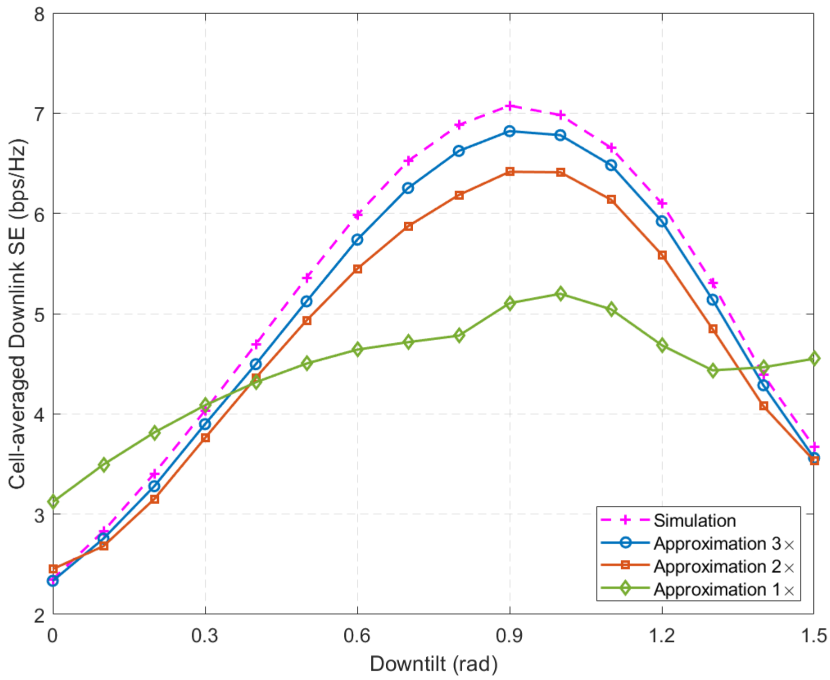

Fig. 3.5 Approximated and simulated cell-averaged downlink SE versus different BS antenna downtilts for the BS antenna height of 9 m.

Table 3.2 Evaluation and Optimization for the Analytical Expressions

	Optimum downtilt (rad)	Maximum average SE loss (%)	Optimal average SE loss (%)
Simulation	0.92	0	0
Approx 3×	0.93	3.242	0.028
Approx 2×	0.95	8.763	0.085
Approx 1×	0.98	26.387	0.453

Fig. 3.5 illustrates a 2D cross-section of Fig. 3.4, showing the optimal BS antenna height and various antenna downtilts. The 2-portion and 8-portion curves are also included for comparison. Table 3.2 provides a more precise extraction from Fig. 3.5, facilitating a detailed evaluation of the analytical expressions and the optimization of the antenna downtilt. It reveals that the difference between the optimal downtilt derived from the approximation 3× and the simulation is only 0.01. When comparing the maximum cell-averaged

downlink SE between the simulation and the discrete approximation, it is observed that the maximum cell-averaged downlink SE of the approximation 3× is 3.242% smaller than that obtained from the simulation. However, when comparing the cell-averaged downlink SE at the optimal downtilt obtained from the simulation and the approximation 3×, it is obvious that the results are almost the same, indicating that the 32-portion discrete approximation is sufficiently accurate for the mm-Wave network. Furthermore, data comparisons among the three types of approximations demonstrate that finer grid resolutions lead to more precise results.

3.5 Summary

In this chapter, the downlink transmission in a mm-Wave network with 3D LSAA is investigated. The BS antenna height and downtilt are jointly optimized to maximize the user SE averaged over all possible locations of the user within the cell coverage area through a quick numerical search. An approximate analysis of the cell-averaged downlink SE is proposed by replacing the continuous distribution of user positions with discrete user positions, utilizing an approximate integration method. Monte Carlo simulations validate the accuracy of discrete approximation. Furthermore, results indicate that an optimized trade-off between the BS antenna height and the BS antenna downtilt can be obtained to sustain an optimal network performance.

Chapter 4

3D Beamforming in Multi-cell Mm-Wave Beamspace MIMO Systems

4.1 Introduction

The work in Chapter 3 investigates the joint impact of BS antenna height and downtilt on a mm-Wave cellular network. Based on the discussions about the proposed system model, certain limitations have been identified, including a simplified beamforming scheme, a complex transceiver design, and a low-efficiency computational approach for determining the average network SE. Narrow beamwidths in mm-Wave frequencies can provide a robust and complementary alternative to small cells by enabling dense spatial multiplexing, thereby facilitating the reuse of spectral resources [93]. The combination of spatial multiplexing and large bandwidth offers the potential for significant improvements in network throughput and SE. The B-MIMO communication designs weights for each beam output and enables data multiplexed onto spatial beams. In general, the number of beams generated from transmitters is smaller than the number of receivers. Implementing B-MIMO communications can reduce the demand for the dimension and quantity of data samples requirements for the BS covariance matrix estimation, thereby lowering the overall computational load [165].

Recently studies have explored B-MIMO to improve the performance of mm-Wave cellular networks. In [56] and [89], reduced-complexity B-MIMO transceivers were simulated in a mm-Wave network. In [97], the authors simulated different beam selection techniques for B-MIMO using ZF precoding to achieve near-optimal performance. The authors in [58] proposed a beam selection algorithm to maximize the sum SE, along with a reduced-dimensional precoder designed to suppress interference. The sum SE and power efficiency of the network with the proposed algorithm is obtained by simulation. In [101], the authors proposed a phase shifter-aided selection mm-Wave network and designed an associated precoding and beam-selection scheme, with simulation results demonstrating the effectiveness of the scheme.

It is noted that the above existing studies only focused on single-cell networks, neglecting the inter-cell interference that occurs in practical multi-cell networks. Moreover, these studies rely solely on simulation results, with no corresponding numerical results provided. Additionally, The BS antenna downtilt has not been investigated in the context of B-MIMO networks. Therefore, it is essential to explore the impact of BS antenna downtilt on the performance of multi-cell multi-user mm-Wave B-MIMO networks, particularly in terms of cell-averaged SE and EE.

In this chapter, the cell-averaged downlink SE of a 3D multi-user mm-Wave cellular network employing a beam-selection method is explored using various precoding schemes. The beam-selection method is intended to operate in conjunction with the DLA, creating a direct correspondence between the number of selected beams and required RF chains, which can enhance the performance of the system with reduced complexity [97]. The system model is based on three adjacent clusters, consistent with that in Chapter 3. It encompasses all possible intra-cell and inter-cell interference, which are typical factors that limit the performance of multi-cell networks. The most commonly used precoding schemes considered include WF precoding and ZF precoding [166], [167]. With the perfect CSI, it is possible to cancel the intra-cell interference completely via ZF precoding. However, it also comes with the enhancement of noise and the loss of energy for the desired signal. WF precoding provides a trade-off between maximizing the desired signal and minimizing interference, but its computational complexity is higher. Analytical expressions of the cell-averaged downlink SE using WF precoding and ZF precoding are first derived, leveraging the beam-selection method. To compute the derived cell-averaged downlink SE, an accurate numerical method utilizing the Riemann sum approximation is proposed to implement the averaging process in the expression. Therein, the coverage area can be divided into infinitesimal equilateral triangle grids to approximate the continuous distribution of user positions by discretizing user positions. The accuracy of the derived analytical expressions is assessed by Monte Carlo simulations. Numerical results show the impact of BS antenna downtilt and BS height on the cell-averaged SE in the proposed mm-Wave cellular network. Furthermore, the performance of the beam-selection method is evaluated by comparing the cell-averaged SE and EE with the full-beam strategy benchmark.

The remainder of this chapter is organized as follows. In Section 4.2, the system model of a mm-Wave B-MIMO network employing the beam-selection method is described. In Section 4.3, analytical expressions of the cell-averaged downlink SE using WF precoding and ZF precoding are derived separately. An accurate numerical approach is proposed to evaluate the expressions. The numerical results are presented in Section 4.4. Finally, this chapter is summarized in Section 4.5.

4.2 System Model

4.2.1 Network and Channel Models

This chapter focuses on downlink transmission in a mm-Wave cellular network, with the network configuration illustrated in Fig. 3.1. Assume that K users, each equipped with a single antenna, are uniformly distributed across the coverage area of each cell. A time-division duplex (TDD) mode is considered to be operated in each cell. To capture the interference from other cells which is possible to affect the intended cell, a three adjacent cluster network with B BSs is considered. Interference generated from further clusters is negligible. The horizontal coverage area of each cell spans an angular range of 120°, and is served by a DLA mounted on the nearest BS, oriented towards the corresponding cell. Specifically, the DLA at the BS can be analytically modeled as a critically sampled URA with antenna element spacing $d \leq \lambda/2$ [164], where the URA has dimensions L_{az} and L_{el} for the azimuth and elevation planes, respectively. This configuration results in a horizontal signal space dimension N_{az} and a vertical signal space dimension N_{el}, representing the number of elements supported by the system in each dimension. These dimensions can be analytically expressed as $N_{\mathrm{az}} = L_{\mathrm{az}}/d$ and $N_{\mathrm{el}} = L_{\mathrm{el}}/d$ [89].

The list of notations that remain consistent with Chapter 3 is summarized in Table 4.1.

Table 4.1 Summary of Notations

Notations	**Definition**
D	Cell radius
h_{b}	The height of a BS
h_{u}	The height of a user
λ	Operating wavelength
N_{t}	Number of antennas at a URA

Assume that a typical user k is served by its home BS b located at the origin, and let the position of user k be denoted by $(x_{b,k}, y_{b,k})$. The received signal for user k associated with BS b is expressed as

$$r_k = \underbrace{\boldsymbol{h}_{b,k}^{\mathrm{H}} \boldsymbol{w}_{b,k} s_{b,k}}_{\text{desired signal}} + \underbrace{\sum_{\substack{k' \neq k \\ k' \in \mathcal{K}_b}} \boldsymbol{h}_{b,k}^{\mathrm{H}} \boldsymbol{w}_{b,k'} s_{b,k'}}_{\text{intra-cell interference}} + \underbrace{\sum_{\substack{b' \neq b \\ b' \in \mathcal{B}}} \sum_{j \in \mathcal{K}_{b'}} \boldsymbol{h}_{b',k}^{\mathrm{H}} \boldsymbol{w}_{b',k} s_{b',j}}_{\text{inter-cell interference}} + n_0, \tag{4.1}$$

where $\mathcal{B} = \{1, \cdots, B\}$ is the set of all BSs in the focused cluster; $\mathcal{K}_b = \{1, \cdots, K\}$ is the set of all users in the coverage area served by BS b; $\boldsymbol{h}_{b,k} \in \mathbb{C}^{N_{\mathrm{t}} \times 1}$ is the downlink channel vector from BS b to user k; $\boldsymbol{w}_{b,k} \in \mathbb{C}^{N_{\mathrm{t}} \times 1}$ denotes the precoding matrix designed by BS b for user k; $s_{b,k}$ represents the independent data symbols transmitted from BS b to user k. The transmitted signal from each BS is subjected to a power constraint P_{t}, i.e. $\mathbb{E}[\|\boldsymbol{x}_b\|^2] \leq P_{\mathrm{t}}$, where $\boldsymbol{x}_b = \sum_{k \in \mathcal{K}_b} \boldsymbol{w}_{b,k} s_{b,k}$ denotes the transmitted signal from BS b; n_0 denotes the AWGN following $\mathcal{CN}(0, \sigma_n^2)$.

Due to the high directional nature of propagation at mm-Wave frequencies, the channel gain of NLOS is significantly weaker compared to LOS signals. Therefore, in mm-Wave channels with LOS components, the impact of NLOS signals can be considered negligible [168]. As a result, this chapter primarily focuses on LOS paths. According to the Saleh-Valenzuela channel model for mm-Wave communications [77], [169], $\boldsymbol{h}_{b,k}$ is expressed as

$$\boldsymbol{h}_{b,k} = \rho_{b,k}(\phi_{b,k}, \theta_{b,k}) \boldsymbol{a}_m(\phi_{b,k}, \theta_{b,k}), \tag{4.2}$$

where $\rho_{b,k}(\phi_{b,k}, \theta_{b,k})$ denotes the complex path loss from BS b to user k, and is given by (3.2); $\phi_{b,k}$ and $\theta_{b,k}$ denote the physical azimuth and elevation AoD at user k, respectively, and are obtained by $\phi_{b,k} = \tan^{-1}(y_{b,k}/x_{b,k})$ and $\theta_{b,k} = \tan^{-1}\left(\frac{h_{\mathrm{b}} - h_{\mathrm{u}}}{\sqrt{x_{b,k}^2 + y_{b,k}^2}}\right)$. $\boldsymbol{a}_m(\phi_{b,k}, \theta_{b,k})$ stands for the transmit array beam steering vector. For the URA at BS b with N_t antenna elements, the beam steering vector can be expressed as [89]

$$\boldsymbol{a}_m(\phi_{b,k},\theta_{b,k}) = \boldsymbol{a}_{m_\mathrm{az}}(\phi_{b,k},\theta_{b,k}) \otimes \boldsymbol{a}_{m_\mathrm{el}}(\phi_{b,k},\theta_{b,k}), \tag{4.3}$$

where

$$\boldsymbol{a}_{m_\mathrm{az}}(\phi_{b,k},\theta_{b,k}) = \frac{1}{\sqrt{N_\mathrm{az}}} e^{-j\pi\left(m_\mathrm{az}-\frac{N_\mathrm{az}-1}{2}\right)\psi_\mathrm{az}}, \tag{4.4}$$

$$\boldsymbol{a}_{m_\mathrm{el}}(\phi_{b,k},\theta_{b,k}) = \frac{1}{\sqrt{N_\mathrm{el}}} e^{-j\pi\left(m_\mathrm{el}-\frac{N_\mathrm{el}-1}{2}\right)\psi_\mathrm{el}}, \tag{4.5}$$

where $m_\mathrm{az} = 0,1,\dots,N_\mathrm{az}-1$, and $m_\mathrm{el} = 0,1,\dots,N_\mathrm{el}-1$ are the antenna element indices. Moreover, $\psi_\mathrm{az} = \frac{d}{\lambda}\sin\phi_{b,k}\sin\theta_{b,k}$ and $\psi_\mathrm{el} = \frac{d}{\lambda}\cos\theta_{b,k}$ represent the spatial frequencies ranging over $\left[-\frac{d}{\lambda},\frac{d}{\lambda}\right]$.

4.2.2 Beam-selection Method in B-MIMO

Spatial sparse happens in mm-Wave frequency bands due to the dominance of LOS channels. In the beamspace domain, beams generated by the BS antenna arrays can fully cover the angular space, enabling the exploitation of the inherent sparsity in mm-Wave LOS channels. By deploying phased arrays at each BS, the conventional spatial channel can be transformed into the beamspace channel [99], and beamforming from each array is fixed with the same direction of AoDs composing a N_t-dimensional spatial signal space. The N_t beams transmitted from a URA, covering the horizontal space, are presented by a unitary beamforming matrix $\boldsymbol{U}_b \in \mathbb{C}^{N_\mathrm{t}\times N_\mathrm{t}}$, which is constructed from steering vectors associated with N_t fixed spatial frequencies. The n-th steering vector is represented as [90], [92]

$$[\boldsymbol{U}_b]_n = \boldsymbol{a}_n(\phi'_{n,k},\theta'_{n,k}), \tag{4.6}$$

where $n = n_{\mathrm{el}} + (n_{\mathrm{az}} - 1)N_{\mathrm{el}}$, $n_{\mathrm{az}} = 1,2,\dots,N_{\mathrm{az}}$ and $n_{\mathrm{el}} = 1,2,\dots,N_{\mathrm{el}}$; the spatial frequencies follow $\sin\phi'_{n,k}\sin\theta'_{n,k} = \frac{2n_{\mathrm{az}}}{N_{\mathrm{az}}} - 1$ and $\cos\theta'_{n,k} = \frac{2n_{\mathrm{el}}}{N_{\mathrm{el}}} - 1$.

When transmitting signals to users in a cell, the minimum requirement of the number of beams for spatial multiplexing is equal to the number of users. In order to ensure that the users can be fully covered, a mask with at least 4 beams is typically utilized, i.e. $N_{\mathrm{s}} = 4$ beams that have the most dominant entries in the channel of users are selected from each URA according to the spatial frequencies. The beams selected from the URA on BS b for user k are represented by choosing a subset of N_{s} rows of $\boldsymbol{U}_b$ as $\widetilde{\boldsymbol{U}}_{b,k} \in \mathbb{C}^{N_{\mathrm{t}}\times N_{\mathrm{s}}}$. Then the beamspace channel matrix with selected beams is given by

$$\widetilde{\boldsymbol{h}}_{b,k} = \widetilde{\boldsymbol{U}}_{b,k}^{\mathrm{H}}\boldsymbol{h}_{b,k}. \tag{4.7}$$

4.3 Cell-averaged SE Analysis in Mm-Wave Cellular Networks

In this section, the expressions for the cell-averaged SE in mm-Wave MIMO systems using WF precoding and ZF precoding are presented. Meanwhile, an accurate approximation method is proposed to enable efficient numerical evaluation of these expressions.

4.3.1 Cell-averaged SE Expressions Using WF Precoding and ZF Precoding

It is assumed that each user in this mm-Wave cellular network is allocated equal transmit power from its serving BS. Both WF precoding and ZF precoding are considered for implementation in the network, respectively. The precoding vector corresponding to the selected beams for the user k served by BS b is given by [166]

$$\widetilde{\boldsymbol{w}}_{b,k} = \gamma_b \widetilde{\boldsymbol{f}}_{b,k}, \tag{4.8}$$

where

$$\widetilde{\boldsymbol{f}}_{b,k} = \begin{cases} \widetilde{\boldsymbol{h}}_{b,k}\left(\widetilde{\boldsymbol{h}}_{b,k}^{\mathrm{H}}\widetilde{\boldsymbol{h}}_{b,k} + \frac{\sigma_n^2 K}{P_t}\right)^{-1}, & \text{for WF} \\ \widetilde{\boldsymbol{h}}_{b,k}\left(\widetilde{\boldsymbol{h}}_{b,k}^{\mathrm{H}}\widetilde{\boldsymbol{h}}_{b,k}\right)^{-1}, & \text{for ZF} \end{cases}, \tag{4.9}$$

and

$$\gamma_b = \sqrt{\frac{P_t}{\sum_{k' \in \mathcal{K}_b} \zeta_s \widetilde{\boldsymbol{f}}_{b,k}^{\mathrm{H}} \widetilde{\boldsymbol{f}}_{b,k}}} = \begin{cases} \sqrt{\frac{P_t}{\sum_{k' \in \mathcal{K}_b} \zeta_s \widetilde{\boldsymbol{h}}_{b,k}^{\mathrm{H}} \widetilde{\boldsymbol{h}}_{b,k}\left(\widetilde{\boldsymbol{h}}_{b,k}^{\mathrm{H}}\widetilde{\boldsymbol{h}}_{b,k} + \frac{\sigma_n^2 K}{P_t}\right)^{-2}}}, & \text{for WF} \\ \sqrt{\frac{P_t}{\sum_{k' \in \mathcal{K}_b} \zeta_s \left(\widetilde{\boldsymbol{h}}_{b,k}^{\mathrm{H}}\widetilde{\boldsymbol{h}}_{b,k}\right)^{-1}}}, & \text{for ZF} \end{cases}, \tag{4.10}$$

where $\zeta_s = \mathbb{E}\left[s_{b,k} s_{b,k}^{\mathrm{H}}\right]$ is correlation matrix of $s_{b,k}$.

Assuming the perfect CSI of the channel vector is applied between each BS and its serving user, the SINR expression of user k is given by

$$\eta_k = \begin{cases} \dfrac{\frac{P_\mathrm{t}}{K}\left|\widetilde{\boldsymbol{h}}_{b,k}^{\mathrm{H}}\widetilde{\boldsymbol{w}}_{b,k}\right|^2}{\frac{P_\mathrm{t}}{K}\sum_{\substack{k' \neq k \\ k' \in \mathcal{K}_b}}\left|\widetilde{\boldsymbol{h}}_{b,k}^{\mathrm{H}}\widetilde{\boldsymbol{w}}_{b,k'}\right|^2 + \frac{P_\mathrm{t}}{K}\sum_{\substack{b' \neq b \\ b' \in \mathcal{B}}}\sum_{j \in \mathcal{K}_{b'}}\left|\widetilde{\boldsymbol{h}}_{b',k}^{\mathrm{H}}\widetilde{\boldsymbol{w}}_{b',j}\right|^2 + \sigma_n^2}, & \text{for WF} \\ \dfrac{\frac{P_\mathrm{t}}{K}\left|\widetilde{\boldsymbol{h}}_{b,k}^{\mathrm{H}}\widetilde{\boldsymbol{w}}_{b,k}\right|^2}{\frac{P_\mathrm{t}}{K}\sum_{\substack{b' \neq b \\ b' \in \mathcal{B}}}\sum_{j \in \mathcal{K}_{b'}}\left|\widetilde{\boldsymbol{h}}_{b',k}^{\mathrm{H}}\widetilde{\boldsymbol{w}}_{b',j}\right|^2 + \sigma_n^2}, & \text{for ZF} \end{cases}, \tag{4.11}$$

where $\widetilde{\boldsymbol{w}}_{b,k}$ denotes the beam-selected precoding vector from BS b to user k; $\widetilde{\boldsymbol{h}}_{b,k}$ denotes the beam-selected channel vector from BS b to user k. The product of channel gain in (4.9) and (4.10) can be expended as

$$
\begin{aligned}
&\tilde{\boldsymbol{h}}_{b,k}^{\mathrm{H}}\tilde{\boldsymbol{h}}_{b,k} \\
&= \left|\rho_{b,k}\left(\phi_{b,k},\theta_{b,k}\right)\right|^2 \sum_{n\in\mathcal{N}_{b,k}} \left|A_{b,n,k}\right|^2 \\
&= \rho_{b,k}^2\left(\phi_{b,k},\theta_{b,k}\right) \sum_{n\in\mathcal{N}_{b,k}} \left|\tilde{\boldsymbol{a}}_n^{\mathrm{H}}\left(\phi'_{n,k},\theta'_{n,k}\right)\boldsymbol{a}_m\left(\phi_{b,k},\theta_{b,k}\right)\right|^2 \\
&= \rho_{b,k}^2\left(\phi_{b,k},\theta_{b,k}\right) \\
&\times \sum_{n\in\mathcal{N}_{b,k}} \frac{1}{N_{\mathrm{t}}^2}\left|\sum_{m_{\mathrm{az}}=0}^{N_{\mathrm{az}}-1}\sum_{m_{\mathrm{el}}=0}^{N_{\mathrm{el}}-1} e^{-j\pi\left(m_{\mathrm{az}}-\frac{N_{\mathrm{az}}-1}{2}\right)c_{n,k}^{\mathrm{az}}} e^{-j\pi\left(m_{\mathrm{el}}-\frac{N_{\mathrm{el}}-1}{2}\right)c_{n,k}^{\mathrm{el}}}\right|^2 \\
&= \frac{\rho_{b,k}^2\left(\phi_{b,k},\theta_{b,k}\right)}{N_{\mathrm{t}}^2} \sum_{n\in\mathcal{N}_{b,k}} \frac{\sin^2\left(\frac{\pi d}{2\lambda}N_{\mathrm{az}}c_{n,k}^{\mathrm{az}}\right)}{\sin^2\left(\frac{\pi d}{2\lambda}c_{n,k}^{\mathrm{az}}\right)} \frac{\sin^2\left(\frac{\pi d}{2\lambda}N_{\mathrm{el}}c_{n,k}^{\mathrm{el}}\right)}{\sin^2\left(\frac{\pi d}{2\lambda}c_{n,k}^{\mathrm{el}}\right)},
\end{aligned}
\tag{4.12}
$$

where $\mathcal{N}_{b,k} = \{1,\cdots,N_s\}$ is the set of selected beams from BS b to user k; $c_{n,k}^{\mathrm{az}}$ and $c_{n,k}^{\mathrm{el}}$ are the correlation coefficient between the transmit array steering vector and the selected beam steering vector. For BS b and its associated user k, it is expressed in the azimuth dimension and elevation dimension, respectively, as

$$
c_{n,k}^{\mathrm{az}} = \sin\phi'_{n,k}\sin\theta'_{n,k} - \sin\phi_{b,k}\sin\theta_{b,k}, \tag{4.13}
$$

$$
c_{n,k}^{\mathrm{el}} = \cos\theta'_{n,k} - \cos\theta_{b,k}. \tag{4.14}
$$

As $\phi_{b,k}$ and $\theta_{b,k}$ are both derived from $x_{b,k}$ and $y_{b,k}$, based on the system model defined in Section 4.2, the expression of cell-averaged downlink SE can be expressed according to Shannon's formula as

$$
\begin{aligned}
R_k &= \mathbb{E}_{x,y}[C_k] = \mathbb{E}_{x,y}[\log_2(1+\eta_k)] \\
&= \frac{1}{\Delta S}\int_{y_{b,k}}\int_{x_{b,k}} \log_2(1+\eta_k) f\left(x_{b,k},y_{b,k}\right) dx_{b,k}dy_{b,k},
\end{aligned}
\tag{4.15}
$$

where C_k is the downlink SE for user k; ΔS denotes the cell coverage area; $f\left(x_{b,k},y_{b,k}\right)$ denotes the PDF of the random variable $x_{b,k}$ and $y_{b,k}$ for user k

served by BS b. When users are uniformly distributed, and $x_{b,k}$ and $y_{b,k}$ are i.i.d., $f(x_{b,k}, y_{b,k})$ is constant and of finite support.

4.3.2 An Accurate Numerical Method

To facilitate fast numerical evaluation of the cell-averaged downlink SE, an accurate numerical method based on the Riemann sum approximation [162] is proposed to implement the averaging process in (4.15). The user position in each rhombic cell area is equally divided into G triangle grids, (4.15) can be approximated by

$$R_k = \frac{1}{3G}\sum_{g=1}^{G}\sum_{i=1}^{3} C_{k,g,i}, \tag{4.16}$$

where $C_{k,g,i}$ denotes the downlink SE for the user located at the vertex of grid g, $g = 1, \cdots, G$. G is the number of grids, which determines the accuracy of this approximation.

Algorithm 4.1: The Coordination of User Position Generation.	
1:	Initialize $\boldsymbol{x}_q = [x_1^q, \cdots, x_{Q_0+1}^q]$ and $\boldsymbol{y}_q = [y_1^q, \cdots, y_{Q_0+1}^q]$. Let $Q = Q_0$.
2:	**Repeat**
3:	Calculate $\boldsymbol{x}'_q = \boldsymbol{x}_q(1{:}\,Q-2) + S_{\mathrm{x}}$ and $\boldsymbol{y}'_q = \boldsymbol{y}_q(1{:}\,Q-1) + S_{\mathrm{y}}$. Let $\boldsymbol{x}_q = \boldsymbol{x}'_q$ and $\boldsymbol{y}_q = \boldsymbol{y}'_q$. $Q = Q - 1$.
4:	**Until** when $Q = 1$.

The coordination of user position in a cell can be obtained by Algorithm 4.1, where Q_0 denotes the sample size of the user along the boundary of a cell and is computed as $Q_0 = \log_2(G) - 1$; S_{x} and S_{y} denote the sample step along x-axis and y-axis, respectively, and are given by $S_{\mathrm{x}} = D/2Q_0$ and $S_{\mathrm{y}} = \sqrt{3}D/4Q_0$. The computational complexity of the algorithm is $\mathcal{O}(Q_0)$.

4.4 Numerical Results

In this section, the performance of the multi-cell multi-user mm-Wave network is evaluated in terms of the cell-averaged SE and EE using WF precoding and ZF precoding schemes. Additionally, the proposed numerical computation method is validated by comparing it with simulation results. The impact of BS antenna downtilts and BS heights on network performance is also examined.

4.4.1 Validation of System Model Analysis

The results of the cell-averaged downlink SE for different SNR from numerical analysis and Monte Carlo simulations are first compared to validate the accuracy of deductions and the approximation method. Each Monte Carlo simulation is performed with 1×10^4 independent random realizations. In each realization, a mm-Wave network following the system model defined in Section 4.2 is simulated. Unless otherwise specified, the simulation parameters are set in Table 4.2.

Table 4.2 Simulation Settings

Parameter	**Value**
Number of active cells, B	7
Cell radius, D	30 m
BS height, h_{b}	10 m
User height, h_{u}	1.5 m
Number of transmit antennas at a URA in azimuth dimension, N_{az}	16

Number of transmit antennas at a URA in elevation dimension, N_{el}	32
Number of users in a cell, K	4
Operating frequency, $1/\lambda$	80 GHz
Transmit power, P_{t}	30 dBm
Horizontal HPBW, $\varphi_{3\mathrm{dB}}$	65°
Vertical HPBW, $\theta_{3\mathrm{dB}}$	35°
Horizontal SLL, SLL_{az}	25 dB
Vertical SLL, SLL_{el}	20 dB
Number of grids, G	210

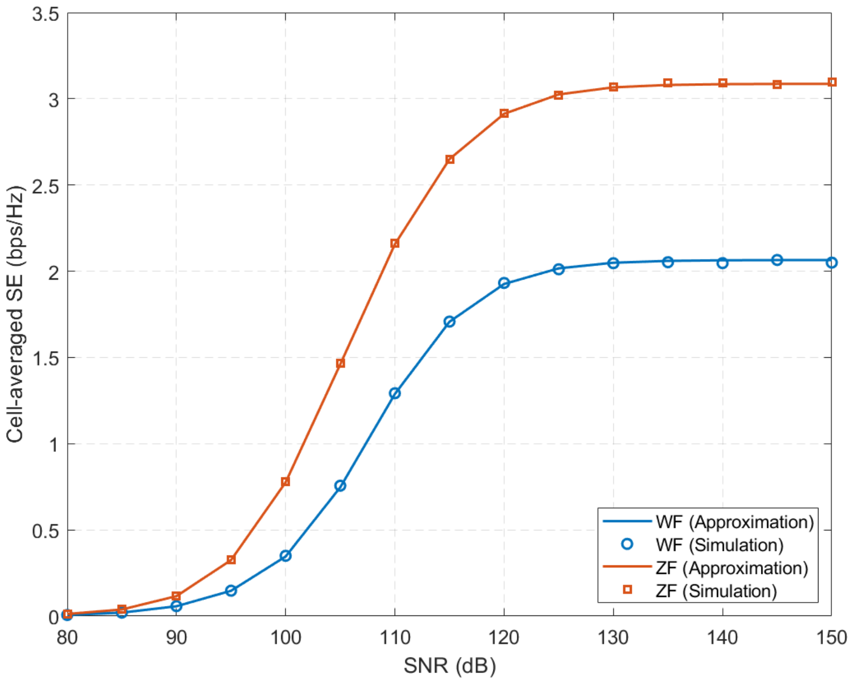

Fig. 4.1 Cell-averaged downlink SE for a mm-Wave network with WF precoding and ZF precoding versus SNR in analysis and simulation.

In Fig. 4.1, the cell-averaged downlink SE with WF precoding and ZF precoding are depicted in analysis and simulation. The BS antenna downtilt is set as $\alpha = \frac{\pi}{8}$ rad. The analysis shows that the analytical results closely align with the simulation outcomes, confirming the accuracy of the derivations and the effectiveness of the proposed approximation method. Comparing curves for different precoding schemes, it is demonstrated that the cell-averaged SE with both precoding schemes monotonically increase. The cell-averaged SE for the ZF precoding scheme is larger than that of the WF precoding.

4.4.2 Impact of BS Antenna Downtilts and BS Heights

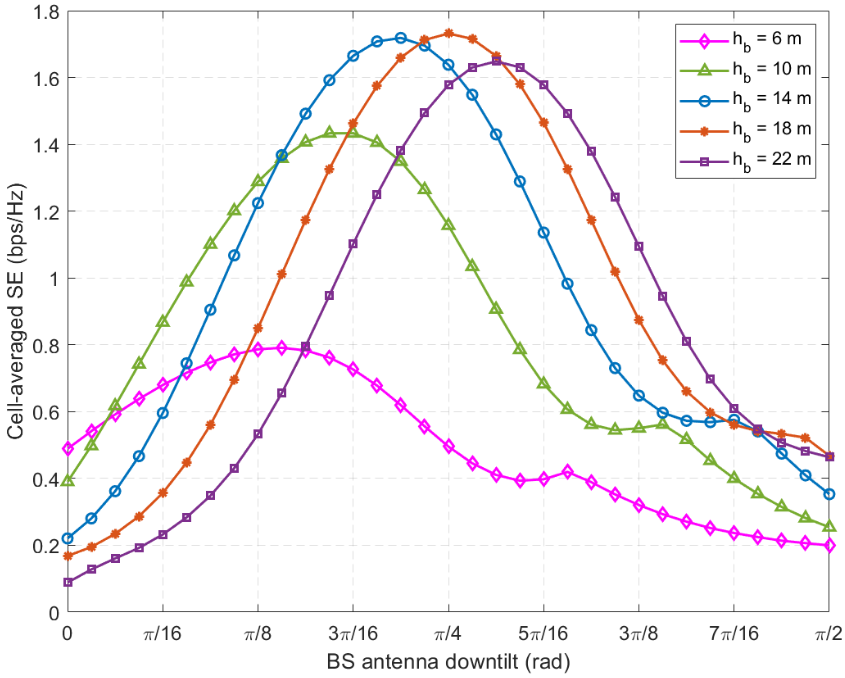

(a) WF precoding networks

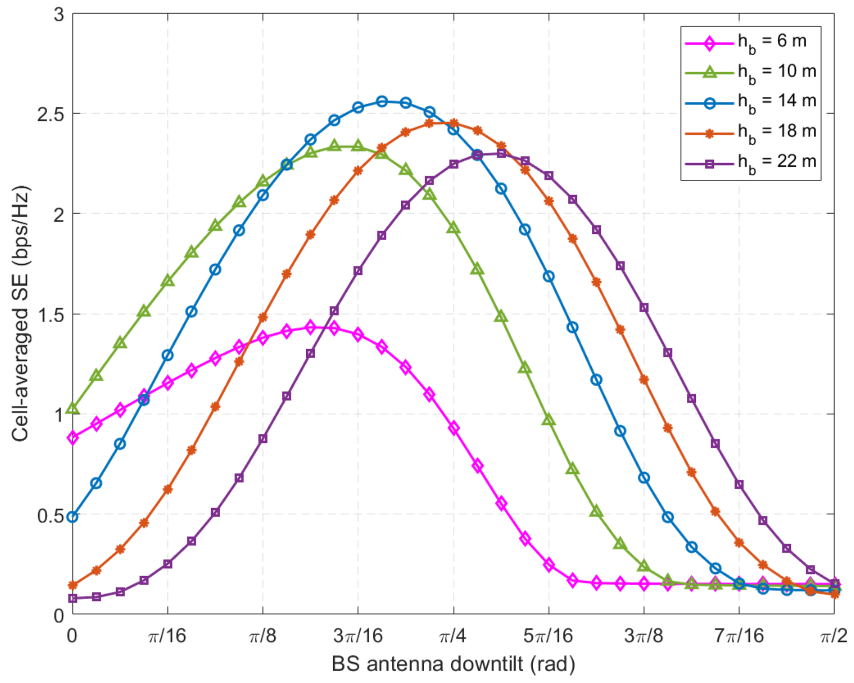

(b) ZF precoding networks

Fig. 4.2 Cell-averaged downlink SE with (a) WF precoding and (b) ZF precoding versus BS antenna downtilt for different BS heights.

In Fig. 4.2, the relationship between BS antenna downtilt and BS height is investigated at SNR = 110 dB. Subfigure (a) illustrates the performance using WF precoding, and subfigure (b) shows the performance using ZF precoding. For both precoding schemes, the cell-averaged SE initially increases with downtilt, reaching a peak before decreasing. As BS height increases, the optimal downtilt also increases due to interference. The maximum cell-averaged SE rises with increasing BS height, peaking at approximately 18 m for WF precoding networks and 14 m for ZF precoding networks. Notably, two peaks are observed in the WF precoding networks, which is not the case for ZF precoding networks. This difference occurs since the overlap among intra-cell beams is reduced as the downtilt approaches $\frac{\pi}{2}$ rad, resulting in the mitigation of intra-cell interference in WF precoding networks. The first peak is significantly higher than the second, as excessive downtilt fails to provide sufficient signal strength to users.

4.4.3 Evaluation of the Beam-selection Method

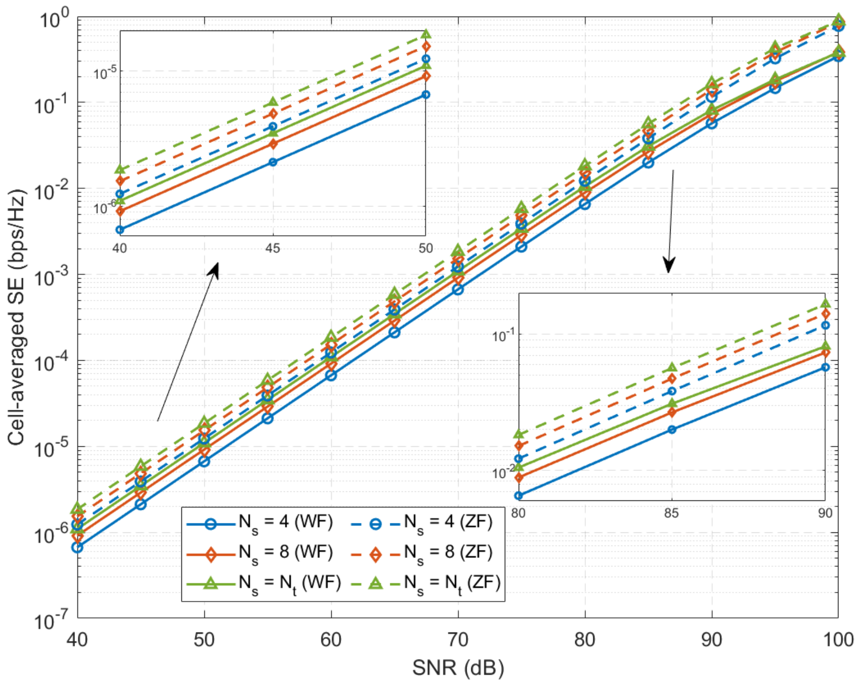

(a) Cell-averaged SE versus SNR

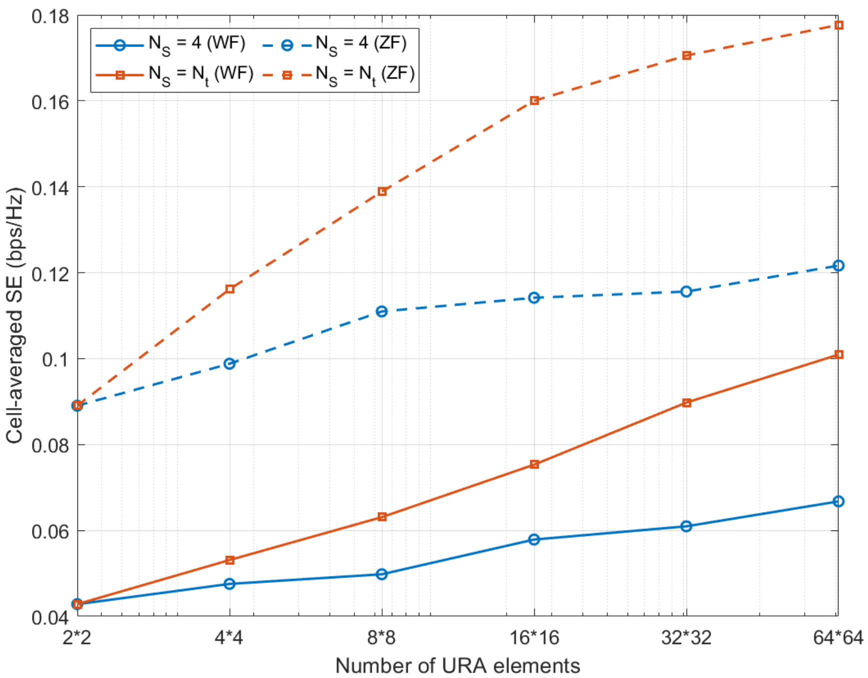

(b) Cell-averaged SE versus URA element number

Fig. 4.3 Evaluation of beam-selection method in WF precoding and ZF precoding networks, comparing the cell-averaged SE based on varying (a) SNR and (b) number of URA elements at $\alpha = \frac{\pi}{8}$ rad.

An analysis of the beam-selection method is presented in Fig. 4.3. In Fig. 4.3(a), the cell-averaged SE of the 4-beam mask strategy is compared with that of the 8-beam mask strategy to illustrate the impact of selecting different numbers of beams. A full-beam strategy is also provided as a benchmark for comparison. It is indicated that at low SNR, the cell-averaged SE with the 4-beam mask strategy can achieve at least 80% of the performance of the 8-beam mask strategy and 70% of that of the full-beam strategy. At high SNR, the 4-beam mask strategy attains at least 85% of the performance of the 8-beam mask strategy and 75% of the full-beam strategy. These results demonstrate the strong efficiency of the 4-beam mask approach.

In Fig. 4.3(b), the impact of the number of URA elements is analyzed at SNR = 90 dB. The URA is assumed to maintain a square configuration, with the number of elements in each dimension ranging from 2 to 64. It is observed that the cell-averaged SE of the 4-beam mask strategy increases monotonically with the number of URA elements, as large size arrays reduce the need for sharing beams among multiple users within each cell. Furthermore, the performance gap between the 4-beam mask and full-beam strategies widens as the number of URA elements grows, due to the greater disparity in the number of active URA elements. Additionally, with larger BS antenna arrays, the cell-averaged SE of the 4-beam mask strategy approaches that of the full-beam strategy more closely in WF precoding networks compared to ZF precoding networks. This is because intra-cell interference in the WF precoding networks can be significantly mitigated by reducing the number of shared beams.

4.4.4 EE for Beam-selection Methods and BS Antenna Downtilting Schemes

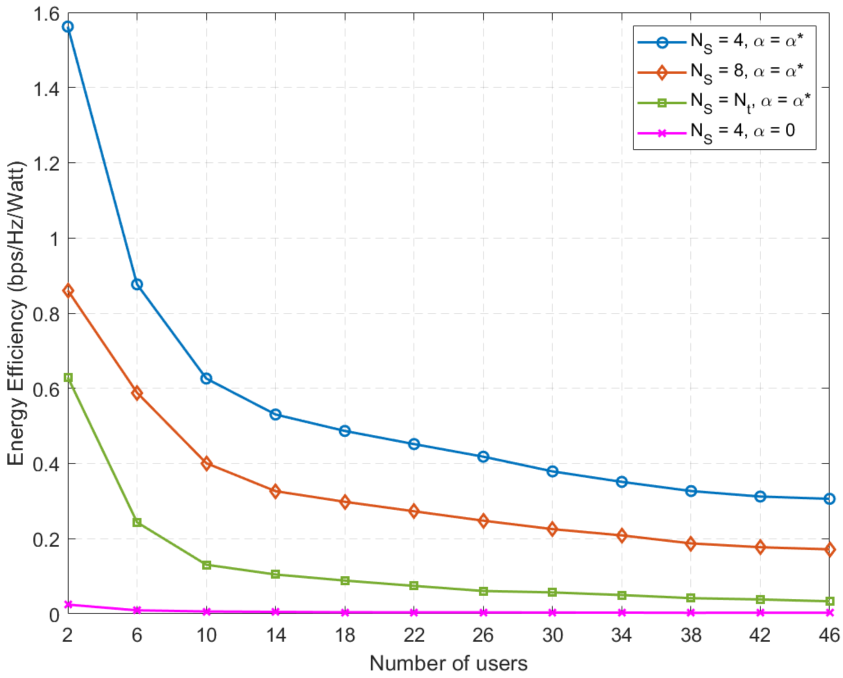

Fig. 4.4 Cell-averaged EE with WF precoding versus the number of users for different beam-selection schemes and BS antenna downtilting schemes.

To access the trade-off between performance and complexity in the practical implementation, specifically regarding the number of selected beams required, the EE of WF precoding mm-Wave networks with different beam-selection schemes is illustrated in Fig. 4.4. The cell-averaged EE is defined in [170] and is expressed as

$$EE = \frac{R_k(\alpha)}{P_{\mathrm{t}} + N_s^{\mathrm{T}} P_{\mathrm{e}}}, \tag{4.17}$$

where N_s^{T} denotes the total number of beams selected from a URA for the users it serves; P_{e} is the power consumed by each URA element, accounting for mixers, digital-to-analog converters, and transmit filters. Practical values for parameters in (4.17) is given by $P_{\mathrm{t}} = 15$ dBm and $P_{\mathrm{e}} = 34.4$ mW [171].

By employing the optimal BS antenna downtilt in the mm-Wave network, it is observed that the cell-averaged EE decreases as the number of users per cell increases. When comparing different beam-selection strategies, the 4-beam mask strategy demonstrates greatly higher cell-averaged EE than the 8-beam mask and full-beam strategies, particularly in scenarios with fewer users, thereby striking an excellent balance among low complexity, cost-efficiency, and high performance.

Additionally, a 4-beam mask strategy network with $\alpha = 0$ is provided as a benchmark to assess the impact of BS antenna downtilt on beam-selected mm-Wave networks. It is evident that the cell-averaged EE in the network with the optimal BS antenna downtilt is significantly enhanced compared to that without a practicable BS antenna downtilt.

4.5 Summary

In this chapter, a downlink mm-Wave communication in multi-user cellular networks utilizing WF and ZF precoding schemes is investigated. A beam-selection method is employed to reduce the number of RF chains required in mm-Wave B-MIMO system transceivers, while maintaining high network performance. To facilitate the computation efficiency, an accurate numerical approximation method is proposed to implement the analytical cell-averaging expressions. The results indicate that the cell-averaged SE of mm-Wave networks using ZF precoding outperforms those using WF precoding. Additionally, adjusting the BS antenna downtilt and BS height has a significant impact on the cell-averaged SE. Furthermore, the evaluation of the beam-selection method demonstrates that the 4-beam mask strategy can achieve the cell-averaged SE comparable to higher-beam and full-beam strategies, while offering considerably better EE. This shows that the beam-selection method provides an effective trade-off between network performance and system complexity.

Chapter 5

Joint Precoding and BS Antenna Downtilting Optimization in Mm-Wave Cellular Networks

5.1 Introduction

In the previous two chapters, the impact of the BS antenna downtilt for a 3D MIMO downlink transmission in a mm-Wave cellular network is investigated by deriving analytical expressions for the network downlink SE. The results show that a significant improvement on the SE can be achieved by the BS antenna design. The maximum SEs were obtained with the optimal BS antenna downtilts from previous chapters. However, these results were achieved via quick numerical searches based on the sweeping method. As noted in Section 2.1, few existing works focus on optimizing BS antenna downtilt, and none have proposed efficient approaches for optimizing BS antenna downtilt in mm-Wave cellular networks. Therefore, this chapter aims to develop a more systematic and tractable approach for BS antenna downtilt optimization. In addition, the transmit power level optimization is addressed as part of power control, given that the beam selection method in Chapter 4 also affects power allocation.

In this chapter, a joint optimization algorithm for precoding and BS antenna downtilting is proposed as a means of enhancing the network SE. A multi-user mm-Wave cellular network is introduced, where each cell is equipped with a URA to enable the 3D MIMO downlink transmission. The optimization problem is then formulated to maximize the sum SE. Due to the complexity of the optimization problem, an AO technique is utilized to decompose the joint optimization problem into two sub-problems [172]. In order to address the nonconvexity of each sub-problem, a FP approach is applied to decouple the problem by leveraging the LDT and the QT [109], [110]. Given the complexity of solving the BS antenna downtilting problem by the FP approach, it is instead translated into a BS antenna gaining optimization problem. A closed-form expression of the optimal BS antenna downtilt is then derived based on the obtained optimal BS antenna gain. The simulation results evaluate the feasibility and convergence of the proposed joint optimization algorithm. Comparative analysis with various benchmark schemes demonstrates that the proposed algorithm significantly enhances the network sum SE.

The remainder of this chapter is organized as follows. In Section 5.2, the system model of a mm-Wave 3D MIMO network is outlined, and the network sum SE maximization problem is formulated. In Section 5.3, the proposed joint optimization algorithm, developed utilizing the AO technique, is presented alongside an analysis of its convergence and computational complexity. The simulation results and discussions are demonstrated in Section 5.4. Finally, this chapter is summarized in Section 5.5.

5.2 System Model and Problem Formulation

5.2.1 System Model

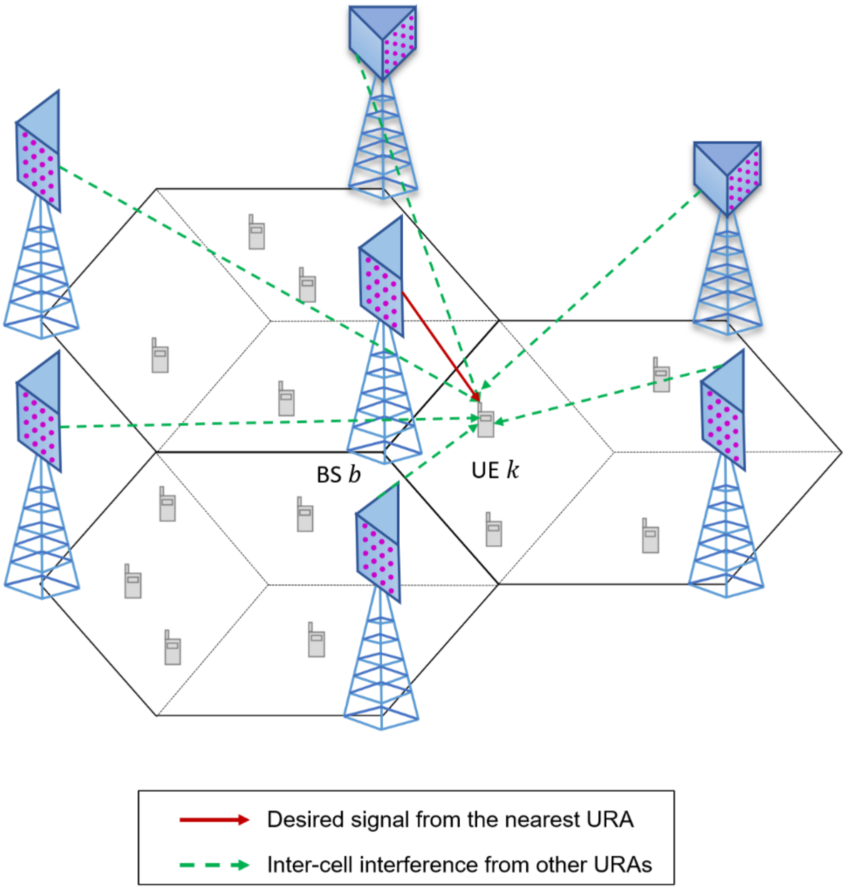

Fig. 5.1 A multi-user mmWave network for downlink communications.

The system model adopted is on the basis of the one presented in Chapter 4. As illustrated in Fig. 5.1, a multi-user mm-Wave cellular network comprising B rhombic cells is proposed. A BS equipped with three URAs is located at the vertex of each cell. The horizontal area for each cell spans an angular range of 120°. Therefore, the received signal of a user is only supplied by URAs facing the user within the fan-shaped area, wherein the nearest URA provides the desired signal, and the other URAs provide inter-cell interference. The list of notations that remain consistent with previous chapters is summarized in Table 5.1.

Table 5.1 Summary of Notations

Notations	Definition
D	Cell radius
h_{b}	The height of a URA
h_{u}	The height of a user
N_{az}	Number of antennas at a URA in azimuth dimension
N_{el}	Number of antennas at a URA in elevation dimension
N_{t}	Number of antennas at a URA
K	Number of users in a cell
λ	Operating wavelength
φ	Phase
SLL_{az}	The maximum attenuation in the horizontal plane
SLL_{el}	The maximum attenuation in the vertical plane

The beamspace channel vector with q selected beams from URA b is denoted by $\boldsymbol{h}_{b,k} \in \mathbb{C}^{q\times 1}$ and expressed as [173]

$$\boldsymbol{h}_{b,k} = \rho_{b,k}\boldsymbol{a}_m^{\mathrm{H}}\left(\phi_{b,k}^t, \theta_{b,k}^t\right)\boldsymbol{a}_m\left(\phi_{b,k}^r, \theta_{b,k}^r\right), \tag{5.1}$$

where $\boldsymbol{a}_m$ is the transmit array beam steering vector controls the direction of 3D beamforming and is presented as (4.3); $\phi_{b,k}^t, \theta_{b,k}^t, \phi_{b,k}^r, \theta_{b,k}^r$ represents the azimuth and elevation angles of departure and arrival. $\rho_{b,k}$ is the complex path loss from URA b to user k and is presented as [56]

$$\rho_{b,k} = \frac{\lambda e^{j\varphi}}{4\pi}\sqrt{\frac{G_{b,k}}{r_{b,k}^2 + (h_{\mathrm{b}} - h_{\mathrm{u}})^2}}, \tag{5.2}$$

where $r_{b,k}$ represents the distance between URA b and user k in the ground plane; $G_{b,k}$ denotes the antenna gain from any antenna element in the URA b to user k and is written in dBi scale as [53]

$$G_{b,k}^{\mathrm{dBi}} = -\min\left\{\left[\min\left(G_{b,k}^{\mathrm{az}}, SLL_{\mathrm{az}}\right) + \min\left(G_{b,k}^{\mathrm{el}}, SLL_{\mathrm{el}}\right)\right], SLL_{\mathrm{az}}\right\}, \tag{5.3}$$

where $G_{b,k}^{\mathrm{az}} = 12\left(\frac{\phi_{b,k}^{r}}{\phi_{3\mathrm{dB}}}\right)^2$, $G_{b,k}^{\mathrm{el}} = 12\left(\frac{\theta_{b,k}^{r}-\alpha_{b,k}}{\phi_{3\mathrm{dB}}}\right)^2$, and $\alpha_{b,k}$ denotes the electrical tilt of antennas at URA b to user k.

Assuming a user k is served by the nearest URAs b, the received signal for user k is expressed as

$$R_k = \boldsymbol{h}_{b,k}^{\mathrm{H}}\boldsymbol{w}_{b,k}s_{b,k} + \sum_{z\in\mathcal{Z}}\sum_{\substack{j\neq k\\ j\in\mathcal{K}_z}} \boldsymbol{h}_{z,k}^{\mathrm{H}}\boldsymbol{w}_{z,k}s_{z,j} + n_0, \tag{5.4}$$

where $\mathcal{Z} = \{1,2,\cdots,Z\}$ denotes the set of active URAs covering user k and Z is the number of active URAs covering user k; $\mathcal{K} = \{1,2,\cdots,K\}$ denotes the set of users in each cell with an active URA; $s_{b,k}$ represents the independent data symbols transmitted from URA b to user k; n_0 is the AWGN following $\mathcal{CN}(0,\sigma_n^2)$. $\boldsymbol{w}_{b,k}$ denotes the precoding vector optimized by URA b for user k. The transmitted signal from URA b is subject to a power budget constraint P_{t}, which is expressed as

$$\textstyle\sum_{k\in\mathcal{K}_b} \mathrm{Tr}\left(\boldsymbol{w}_{b,k}\boldsymbol{w}_{b,k}^{\mathrm{H}}\right) \leq P_{\mathrm{t}}\ . \tag{5.5}$$

The instantaneous SE for user k is expressed as

$$\begin{aligned}\eta_{b,k} &= \log\left(1 + SINR_{b,k}\right)\\ &= \log\left(1 + \frac{\left|\boldsymbol{h}_{b,k}^{\mathrm{H}}\boldsymbol{w}_{b,k}\right|^2}{\sum_{z\in\mathcal{Z}}\sum_{\substack{j\neq k\\ j\in\mathcal{K}_z}}\left|\boldsymbol{h}_{z,k}^{\mathrm{H}}\boldsymbol{w}_{z,j}\right|^2 + \sigma_n^2}\right).\end{aligned} \tag{5.6}$$

5.2.2 Problem Formulation

The sum SE is a critical network performance metric that qualifies the total data that can be transmitted over the given wireless channel bandwidth. In 3D MIMO systems, optimizing the sum SE is essential for enhancing mobile broadband systems, as it enables higher transmission rates and improves spectrum utilization. To improve the reliability of communication and maximize the total transmitted data over a bandwidth, this chapter focuses on the instantaneous network sum SE maximization through the optimization of both the precoding vector and BS antenna downtilt, subject to the maximum transmit power constraint and BS antenna downtilt angle range constraint. $\boldsymbol{w} = \{\boldsymbol{w}_{b,k} | \forall b \in \mathcal{B}, \forall k \in \mathcal{K}_b\}$ and $\boldsymbol{\alpha} = \{\alpha_{b,k} | \forall b \in \mathcal{B}, \forall k \in \mathcal{K}_b\}$ are denoted as the set of precoding matrices of all BS URAs and the set of antenna-downtilting matrices of all BS URAs, respectively; $\mathcal{B}$ denotes the set of all URAs. The optimization problem for maximizing the network sum SE is formulated as

$$
\begin{aligned}
(\mathcal{P}1) \quad & \max_{\boldsymbol{w},\boldsymbol{\alpha}} \quad \sum_{b=1}^{B} \sum_{k=1}^{K} \eta_{b,k} \\
& \text{s.t.} \quad \text{C1:} \ \sum_{k \in \mathcal{K}_b} \left\| \boldsymbol{w}_{b,k} \right\|^2 \le P_{\text{t}}, \forall b \in \mathcal{B}, \\
& \qquad\ \ \text{C2:} \ 0 \le \alpha_{b,k} \le \frac{\pi}{2}, \forall b \in \mathcal{B}, \forall k \in \mathcal{K}_b,
\end{aligned} \tag{5.7}
$$

where the constraint function C1 is due to the maximum transmit power budget and C2 stands for the bounds of BS antenna downtilts.

The interference in SINR expression in (5.6) is cross-mode and cross-layered coupled. Therefore, the problem presented in (5.7) is a highly non-convex nonlinear programming (NLP) problem, which is known to be NP-hard. Solving the global optimum solution to the NLP problems is particularly challenging. On the one hand, the combinatorial problem framework leads to the requirement of a comprehensive search with exponential complexity; On the other hand, the occurrence possibility of multiple maxima within the search range increases the difficulty of finding the maximum value. Hence in the following section, a tractable optimization algorithm which is on the basis of the AO technique is proposed to address this problem by separately and iteratively obtaining the optimized $\boldsymbol{w}$ and $\boldsymbol{\alpha}$.

5.3 Optimization Algorithm

The main idea of the proposed optimization algorithm is utilizing the AO technique by means of an iterative procedure and breaking the joint optimization problem down into two sub-problems. For each sub-problem, an FP approach is applied to decouple problem $(\mathcal{P}1)$ by using the LDT and the QT. The iterative procedure can improve the network sum SE by optimizing $\boldsymbol{w}$ and $\boldsymbol{\alpha}$ separately in each iteration round, that is to say, $\boldsymbol{w}$ is optimized by a given $\boldsymbol{\alpha}$; then fixing $\boldsymbol{w}$, $\boldsymbol{\alpha}$ can be optimized utilizing the same method. The network sum SE converges to the global optimum solution after an appropriate iteration algorithm.

5.3.1 Reformulation of Logarithms

Since (5.6) is a non-decreasing concave logarithmic function, the LDT is applied to move the SINR ratio outside the logarithm. After the transformation, the objective function in $(\mathcal{P}1)$ is expressed as the following equivalent function,

$$\mathcal{F}(\boldsymbol{w},\boldsymbol{\alpha},\boldsymbol{\beta}) = \sum_{b=1}^{B}\sum_{k=1}^{K}\left[\log\left(1+\beta_{b,k}\right) - \beta_{b,k} + \frac{\left(1+\beta_{b,k}\right)SINR_{b,k}}{SINR_{b,k}+1}\right], \quad (5.8)$$

where $\boldsymbol{\beta} = \left\{\beta_{b,k} | \forall b \in \mathcal{B}, \forall k \in \mathcal{K}_b\right\}$ denotes the set of auxiliary variables introduced for SINR decoupling. The optimal $\beta_{b,k}$ can be obtained as $\beta_{b,k}^{*} = SINR_{b,k}$ by setting $\frac{\partial \mathcal{F}}{\partial \beta_{b,k}} = 0$ for given $\boldsymbol{w}$ and $\boldsymbol{\alpha}$. Since the variables that need to be optimized, i.e. $\boldsymbol{w}$ and $\boldsymbol{\alpha}$, are only involved in the item $\frac{(1+\beta_{b,k})SINR_{b,k}}{SINR_{b,k}+1}$ in (5.8), the optimization problem $(\mathcal{P}1)$ can be simplified as

$$(\mathcal{P}2) \quad \max_{\boldsymbol{w},} \quad \sum_{b=1}^{B}\sum_{k=1}^{K}\frac{\left(1+\beta_{b,k}\right)SINR_{b,k}}{SINR_{b,k}+1}$$

$$\text{s.t.} \quad \text{C1, C2.} \tag{5.9}$$

At this point, the complex logarithm operation in (5.7) has been transformed into a sum-of-functions ratio problem, which is easier to be dealt with by the QT. Although the logarithm is eliminated after applying LDT, problem $(\mathcal{P}2)$ remains non-linear and non-convex, making direct solutions both time-consuming and computationally expensive. To address this, the AO technique is utilized to simplify the complexity of the multi-variable problem $(\mathcal{P}2)$, thereby improving computational efficiency and making this constrained optimization problem more tractable. The following two subsections provide details on how to decouple the variables $\boldsymbol{w}$ and $\boldsymbol{\alpha}$ by fixing one variable and solving the other.

5.3.2 Precoding Optimization

This subsection focuses on addressing the problem $(\mathcal{P}2)$ over the precoding variables $\boldsymbol{w}$ for a given $\boldsymbol{\alpha}$. The precoding optimization problem can be written as

$$(\mathcal{P}2.1\text{a}) \quad \max_{\boldsymbol{w}} \quad \mathcal{F}_1(\boldsymbol{w})=\sum_{b=1}^{B}\sum_{k=1}^{K}\frac{\left(1+\beta_{b,k}\right)\left|\boldsymbol{h}_{b,k}^{\mathrm{H}}\boldsymbol{w}_{b,k}\right|^2}{\sum_{z\in\mathcal{Z}}\sum_{j\in\mathcal{K}_z}\left|\boldsymbol{h}_{z,k}^{\mathrm{H}}\boldsymbol{w}_{z,j}\right|^2+\sigma_n^2}$$

$$\text{s.t.} \quad \text{C1.} \tag{5.10}$$

Applying the QT, $\mathcal{F}_1(\boldsymbol{w})$ can be reformulated as

$$\begin{aligned}\mathcal{F}_{1\text{a}}(\boldsymbol{w},\boldsymbol{\gamma})=\sum_{b=1}^{B}\sum_{k=1}^{K}\Bigg[&2\sqrt{1+\beta_{b,k}}\,\Re\left\{\gamma_{b,k}^{\dagger}\boldsymbol{h}_{b,k}^{\mathrm{H}}\boldsymbol{w}_{b,k}\right\}\\&-\left|\gamma_{b,k}\right|^2\left(\sum_{z\in\mathcal{Z}}\sum_{j\in\mathcal{K}_z}\left|\boldsymbol{h}_{z,k}^{\mathrm{H}}\boldsymbol{w}_{z,j}\right|^2+\sigma_n^2\right)\Bigg],\end{aligned} \tag{5.11}$$

where $\boldsymbol{\gamma}$ denotes the collection of auxiliary variables $\{\gamma_{b,k} | \forall b \in \mathcal{B}, \forall k \in \mathcal{K}_b\}$. The optimization problem $(\mathcal{P}2.1\text{a})$ then can be rewritten to a biconvex problem as

$$(\mathcal{P}2.1\text{b}) \quad \max_{\boldsymbol{w},\boldsymbol{\gamma}} \quad \mathcal{F}_{1\text{a}}(\boldsymbol{w},\boldsymbol{\gamma})$$
$$\text{s.t.} \quad \text{C1}. \tag{5.12}$$

After Giving a fixed $\boldsymbol{w}$, applying $\beta_{b,k} = \beta_{b,k}^*$, and setting $\frac{\partial \mathcal{F}_{1\text{a}}(\boldsymbol{\gamma})}{\partial \gamma_{b,k}} = 0$, the optimal $\gamma_{b,k}$ is derived as

$$\gamma_{b,k}^* = \frac{\sqrt{1+\beta_{b,k}}\boldsymbol{h}_{b,k}^{\text{H}}\boldsymbol{w}_{b,k}}{\sum_{z\in\mathcal{Z}}\sum_{j\in\mathcal{K}_z}\left|\boldsymbol{h}_{z,k}^{\text{H}}\boldsymbol{w}_{z,j}\right|^2 + \sigma_n^2}. \tag{5.13}$$

Then (5.11) is a convex function after applying $\gamma_{b,k}^*$. The Lagrangian function of it can be expressed as

$$\begin{aligned}\mathcal{L}_{1\text{a}}(\boldsymbol{w},\boldsymbol{\omega}) = \sum_{b=1}^{B}\sum_{k=1}^{K}\Bigg[& 2\sqrt{1+\beta_{b,k}}\Re\{\gamma_{b,k}^{\dagger}\boldsymbol{h}_{b,k}^{\text{H}}\boldsymbol{w}_{b,k}\} \\ & - \left|\gamma_{b,k}\right|^2\left(\sum_{z\in\mathcal{Z}}\sum_{j\in\mathcal{K}_z}\left|\boldsymbol{h}_{z,k}^{\text{H}}\boldsymbol{w}_{z,j}\right|^2 + \sigma_n^2\right)\Bigg] \\ & + \sum_{b=1}^{B}\omega_b\left(\sum_{k=1}^{K}\left\|\boldsymbol{w}_{b,k}\right\|^2 - P_{\text{t}}\right),\end{aligned} \tag{5.14}$$

where $\boldsymbol{\omega} = [\omega_1, \omega_2, \cdots, \omega_b]$ and ω_b denotes the Lagrange multiplier associated with C1 for URA b. The optimal ω_b can be determined according to complementary slackness as

$$\omega_b^* = \min\left\{\omega_b \geq 0 \colon \sum_{k=1}^{K}\left\|\boldsymbol{w}_{b,k}(\omega_b)\right\|^2 \leq P_{\text{t}}\right\}. \tag{5.15}$$

For efficient computation, the sub-gradient method is applied to search for ω_b^*. Then by setting $\frac{\partial \mathcal{L}_{1\mathrm{a}}(\boldsymbol{w})}{\partial \boldsymbol{w}_{b,k}} = 0$, the optimal $\boldsymbol{w}_{b,k}$ can be obtained as

$$\boldsymbol{w}_{b,k}^* = \sqrt{1+\beta_{b,k}}\gamma_{b,k}\left(\sum_{z\in\mathcal{Z}}\sum_{j\in\mathcal{K}_z}\left|\gamma_{z,k}\right|^2\boldsymbol{h}_{b,j}\boldsymbol{h}_{b,j}^{\mathrm{H}} + \omega_b\boldsymbol{I}_q\right)^{-1}\boldsymbol{h}_{b,k}. \quad (5.16)$$

5.3.3 BS Antenna Downtilting Optimization

This subsection focuses on addressing the problem $(\mathcal{P}2)$ over the BS antenna downtilting variable $\boldsymbol{\alpha}$ for a given $\boldsymbol{w}$. Given $\boldsymbol{w}$**,** the BS antenna downtilting optimization problem can be written as

$$(\mathcal{P}2.2\mathrm{a}) \quad \max_{\boldsymbol{\alpha}} \quad \mathcal{F}_2(\boldsymbol{\alpha}) = \sum_{b=1}^{B}\sum_{k=1}^{K}\frac{(1+\beta_{b,k})\left|\boldsymbol{h}_{b,k}^{\mathrm{H}}(\alpha_{b,k})\boldsymbol{w}_{b,k}\right|^2}{\sum_{z\in\mathcal{Z}}\sum_{j\in\mathcal{K}_z}\left|\boldsymbol{h}_{z,k}^{\mathrm{H}}(\alpha_{z,j})\boldsymbol{w}_{z,j}\right|^2 + \sigma_n^2}$$

$$\mathrm{s.t.} \quad \mathrm{C2}. \quad (5.17)$$

From (5.3), it can be seen that α is contained within more than one complicated operations for the minimum value finding, which is hard to be transformed by the FP approach. Consequently, the BS antenna downtilting optimization problem is translated into the BS antenna gaining optimization problem, $(\mathcal{P}2.2\mathrm{a})$ then can be rewritten as the

$$(\mathcal{P}2.2\mathrm{b}) \quad \max_{\boldsymbol{g}} \quad \mathcal{F}_2(\boldsymbol{g}) = \sum_{b=1}^{B}\sum_{k=1}^{K}\frac{(1+\beta_{b,k})g_{b,k,k}(\alpha_{b,k})\left|\mathcal{A}_{b,k,k}\right|^2}{\sum_{z\in\mathcal{Z}}\sum_{j\in\mathcal{K}_z}g_{z,k,j}(\alpha_{z,j})\left|\mathcal{A}_{z,k,j}\right|^2 + \sigma_n^2}$$

$$\mathrm{s.t.} \quad \mathrm{C3}: 10^{-\frac{SLL_{\mathrm{az}}}{20}} \le g_{b,k,k} \le 1, \forall b\in\mathcal{B}, \forall k\in\mathcal{K}_b, \quad (5.18)$$

where $g_{b,k,k} = \sqrt{G_{b,k,k}}$; $\mathcal{A}_{b,k,k} = \left(\varrho_{b,k}\boldsymbol{a}_m^{\mathrm{H}}(\phi_{b,k}^t,\theta_{b,k}^t)\boldsymbol{a}_m(\phi_{b,k}^r,\theta_{b,k}^r)\right)^{\mathrm{H}}\boldsymbol{w}_{b,k}$ and $\mathcal{A}_{z,k,j} = \left(\varrho_{z,k}\boldsymbol{a}_m^{\mathrm{H}}(\phi_{z,k}^t,\theta_{z,k}^t)\boldsymbol{a}_m(\phi_{z,k}^r,\theta_{z,k}^r)\right)^{\mathrm{H}}\boldsymbol{w}_{z,j}$, $\varrho_{b,k} = \frac{\lambda e^{j\varphi}}{4\pi\sqrt{r_{b,k}^2+(h_{\mathrm{b}}-h_{\mathrm{u}})^2}}$.

Applying the QT, $\mathcal{F}_2(\boldsymbol{g})$ can be reformulated as

$$\begin{aligned}\mathcal{F}_{2\mathrm{a}}(\boldsymbol{g},\boldsymbol{\varepsilon}) = \sum_{b=1}^{B}\sum_{k=1}^{K}\Bigg[&2\sqrt{1+\beta_{b,k}}\Re\left\{\varepsilon_{b,k}^{\dagger}\sqrt{g_{b,k,k}}\mathcal{A}_{b,k,k}\right\}\\ &-\left|\varepsilon_{b,k}\right|^{2}\left(\sum_{z\in\mathcal{Z}}\sum_{j\in\mathcal{K}_z} g_{z,k,j}\left|\mathcal{A}_{z,k,j}\right|^{2}+\sigma_n^2\right)\Bigg],\end{aligned} \tag{5.19}$$

where $\boldsymbol{\varepsilon}$ denotes the collection of auxiliary variables $\{\varepsilon_{b,k}|\forall b\in\mathcal{B},\forall k\in\mathcal{K}_b\}$. The optimization problem $(\mathcal{P}2.2\mathrm{b})$ then can be rewritten to a biconvex problem as

$$\begin{aligned}(\mathcal{P}2.2\mathrm{c})\quad &\max_{\boldsymbol{g},\boldsymbol{\varepsilon}} \quad \mathcal{F}_{2\mathrm{a}}(\boldsymbol{g},\boldsymbol{\varepsilon})\\ &\mathrm{s.t.}\quad \mathrm{C3}.\end{aligned} \tag{5.20}$$

Given a fixed $\boldsymbol{w}$ and setting $\frac{\partial\mathcal{F}_{2a}(\boldsymbol{\varepsilon})}{\partial\varepsilon_{b,k}}=0$, the optimal $\varepsilon_{b,k}$ is obtained as

$$\varepsilon_{b,k}^{*} = \frac{\sqrt{\left(1+\beta_{b,k}\right)g_{b,k,k}}\left|\mathcal{A}_{b,k,k}\right|}{\sum_{z\in\mathcal{Z}}\sum_{j\in\mathcal{K}_z} g_{z,k,j}\left|\mathcal{A}_{z,k,j}\right|^{2}+\sigma_n^2}. \tag{5.21}$$

Due to the quadratic term in $\mathrm{C3}$, $(\mathcal{P}2.2\mathrm{c})$ with respect to $g_{b,k,k}$ can be characterized as quadratically constrained quadratic program and is rewritten as

$$\begin{aligned}(\mathcal{P}2.2\mathrm{d})\quad &\max_{\boldsymbol{g}} \quad \mathcal{F}_{2\mathrm{b}}(\boldsymbol{g}) = \sum_{b=1}^{B}\sum_{k=1}^{K} -g_{b,k,k}\mathcal{N}_b + 2\Re\left(\sqrt{g_{b,k,k}}\mathcal{M}_b\right)\\ &\mathrm{s.t.}\quad \mathrm{C3},\end{aligned} \tag{5.22}$$

where $\mathcal{N}_b = \sum_{z\in\mathcal{Z}}\sum_{j\in\mathcal{K}_z}\left|\varepsilon_{z,j}\right|^2\sum_{k\in\mathcal{K}_b}\left|\mathcal{A}_{b,j,k}\right|^2$ and $\mathcal{M}_b = \sum_{k\in\mathcal{K}_b}\sqrt{1+\beta_{b,k}}\left|\varepsilon_{b,k}\mathcal{A}_{b,k,k}\right|$. It is obvious that $\mathcal{F}_{2\mathrm{b}}$ is a quadratic convex function of $\boldsymbol{g}$ since $\mathcal{N}_b$ is positive. Furthermore, $\mathrm{C3}$ can be separated to two sub-constraints as $\mathrm{C3a}$: $g_{b,k,k}\geq 10^{-\frac{SLL_{\mathrm{az}}}{20}}$ and $\mathrm{C3b}$: $g_{b,k,k}\leq 1$, each of both is convex quadratic constraint. As a result, $(\mathcal{P}2.2\mathrm{d})$ is a convex problem. Now a

Lagrange dual problem of $(\mathcal{P}2.2\mathrm{d})$ can be generated via Lagrange dual decomposition as

$$
\begin{aligned}
(\mathcal{P}2.2\mathrm{e}) \quad \min_{\boldsymbol{\mu},\boldsymbol{\nu}} \quad & \mathscr{g}_{2\mathrm{b}}(\boldsymbol{\mu},\boldsymbol{\nu}) = \sup_{\boldsymbol{g}} \mathcal{L}_{2\mathrm{b}}(\boldsymbol{g},\boldsymbol{\mu},\boldsymbol{\nu}), \\
\text{s.t.} \quad & \mu_{b,k} \geq 0, \forall b \in \mathcal{B}, \forall k \in \mathcal{K}_b, \\
& \nu_{b,k} \geq 0, \forall b \in \mathcal{B}, \forall k \in \mathcal{K}_b,
\end{aligned} \tag{5.23}
$$

where $\boldsymbol{\mu} = \{\mu_{b,k} | \forall b, k\}$ and $\boldsymbol{\nu} = \{\nu_{b,k} | \forall b, k\}$, $\mu_{b,k}$ and $\nu_{b,k}$denote the Lagrange multipliers for the constraint $\mathrm{C3a}$ and $\mathrm{C3b}$, respectively. $\mathcal{L}(\boldsymbol{g},\boldsymbol{\mu},\boldsymbol{\nu})$ represents the Lagrangian function of $\mathcal{F}_{2\mathrm{b}}$ and is expressed as

$$
\begin{aligned}
\mathcal{L}_{2\mathrm{b}}(\boldsymbol{g},\boldsymbol{\mu},\boldsymbol{\nu}) = \sum_{b=1}^{B} \sum_{k=1}^{K} \Big[& -g_{b,k,k}\mathcal{N}_b + 2\Re\left(\sqrt{g_{b,k,k}}\mathcal{M}_b\right) \\
& - \mu_{b,k}\left(g_{b,k,k} - 10^{-\frac{SLL_{\mathrm{az}}}{20}}\right) + \nu_{b,k}\left(g_{b,k,k} - 1\right)\Big].
\end{aligned} \tag{5.24}
$$

It can be confirmed that $\mathcal{L}_{2\mathrm{b}}(\boldsymbol{g},\boldsymbol{\mu},\boldsymbol{\nu})$ is a convex function, thus $\mathscr{g}_{2\mathrm{b}}(\boldsymbol{\mu},\boldsymbol{\nu})$ is a concave problem. In addition, $\boldsymbol{g}$ satisfies the Slater's condition. Therefore, it can be stated that the strong duality holds, e.g., the optimal value of $(\mathcal{P}2.2\mathrm{d})$ and $(\mathcal{P}2.2\mathrm{e})$ are the same [174]. Consequently, $(\mathcal{P}2.2\mathrm{d})$ can be equivalently solved by $(\mathcal{P}2.2\mathrm{e})$. For given $\boldsymbol{\mu}$ and $\boldsymbol{\nu}$, the optimal $\boldsymbol{g}$ can be obtained by setting $\frac{\partial \mathcal{L}_{2\mathrm{b}}(\boldsymbol{g})}{\partial \boldsymbol{g}_{b,k,k}} = 0$ as

$$
g_{b,k,k}^{*} = \frac{\Re\{\mathcal{M}_b\}}{\mathcal{N}_b + \mu_{b,k} - \nu_{b,k}}. \tag{5.25}
$$

The optimal $\mu_{b,k}$ and $\nu_{b,k}$ are determined by

$$
\{\mu_{b,k}^{*}, \nu_{b,k}^{*}\} = \min\left\{\mu_{b,k} - \nu_{b,k} | \, \mu_{b,k}, \nu_{b,k} \geq 0, 10^{-\frac{SLL_{\mathrm{az}}}{20}} \leq g_{b,k,k} \leq 1\right\}, \tag{5.26}
$$

and can be efficiently computed by the sub-gradient method according to $\mathrm{C3}$.

To obtain the optimal BS antenna downtilt $\alpha_{b,k}$, (5.3) is required to be written subject to C3 as

$$G_{b,k}^{\text{dBi}} = \begin{cases} -G_{b,k}^{\text{az}} - G_{b,k}^{\text{el}}, & \text{if } -\phi^{\text{az}} \leq \phi_{b,k}^{r} \leq \phi^{\text{az}}, \\ & \quad -\theta^{\text{el}} \leq \theta_{b,k}^{r} \leq \theta^{\text{el}} \\ -G_{b,k}^{\text{az}} - SLL_{\text{el}}, & \text{if } -\phi^{\text{az-el}} \leq \phi_{b,k}^{r} \leq \phi^{\text{az-el}}, \\ & \quad \theta_{b,k}^{r} \leq -\theta^{\text{el}} \cup \theta_{b,k}^{r} \geq \theta^{\text{el}} \end{cases}. \tag{5.27}$$

where $\phi^{\text{az}} = \phi_{3dB}\sqrt{\frac{SLL_{\text{az}}}{12}}$, $\theta^{\text{el}} = \theta_{3dB}\sqrt{\frac{SLL_{\text{el}}}{12}}$, and $\phi^{\text{az-el}} = \phi_{3dB}\sqrt{\frac{SLL_{\text{az}}-SLL_{\text{el}}}{12}}$. Applying $g_{b,k,k} = g_{b,k,k}^{*}$, the optimal $\alpha_{b,k}$ then can be computed as

$$\alpha_{b,k}^{*} = \begin{cases} \theta_{b,k}^{r} \pm \theta_{3dB}\sqrt{\dfrac{-10\log\left(g_{b,k,k}\right) - G_{b,k}^{\text{az}}}{12}}, & \text{if } -\phi^{\text{az}} \leq \phi_{b,k}^{r} \leq \phi^{\text{az}}, \\ & \quad -\theta^{\text{el}} \leq \theta_{b,k}^{r} \leq \theta^{\text{el}} \\ \text{any value in } \left[0, \dfrac{\pi}{2}\right], & \text{if } -\phi^{\text{az-el}} \leq \phi_{b,k}^{r} \leq \phi^{\text{az-el}}, \\ & \quad \theta_{b,k}^{r} \leq -\theta^{\text{el}} \cup \theta_{b,k}^{r} \geq \theta^{\text{el}} \end{cases}. \tag{5.28}$$

5.3.4 Convergence and Complexity Analysis

Algorithm 5.1: Optimization Iterative Framework.

1: Initialize values for precoding vector $\boldsymbol{w}$ and BS antenna gain $\boldsymbol{g}$ as $\boldsymbol{w}_{b,k} = \frac{\boldsymbol{h}_{b,k}}{\|\boldsymbol{h}_{b,k}\|}$ and $10^{-\frac{SLL_{\text{az}}}{20}} \leq g_{b,k,k} \leq 1$.

2: Set $\tau = 0$;

3: **Repeat**

4: Step 1: Update $\boldsymbol{\beta}^{*} = \left\{SINR_{b,k} \mid \forall b \in \mathcal{B}, \forall k \in \mathcal{K}_b\right\}$;

5: Step 2: Update $\boldsymbol{\gamma}^{*}$ by (5.13);

6: Step 3: Update $\boldsymbol{w}^{*}$ by (5.16);

7: Step 4: Update $\boldsymbol{\varepsilon}^{*}$ by (5.21);

8: Step 5: Update $\boldsymbol{g}^{*}$ by (5.25);

9: Step 6: Update $\boldsymbol{\alpha}^{*}$ by (5.28);

10: Set $\tau = \tau + 1$;

11: **until** $\mathcal{F}$ in function (5.8) converges as $\left|\left(\mathcal{F}^{(\tau)} - \mathcal{F}^{(\tau-1)}\right)/\mathcal{F}^{(\tau-1)}\right| \leq \epsilon$, where $\epsilon \to 0$.

The details of the proposed optimization algorithm are summarized in Algorithm 5.1. It combines the two subsections above into a joint algorithm that iteratively alternates between the optimization of the precoding vector and the BS antenna downtilting. In each iterative loop, after updating the precoding vector, the BS antenna gain is adjusted accordingly based on the new precoding vector. Due to the non-decreasing network sum SE function provided after each iteration, Algorithm 5.1 can be guaranteed to converge. The iterative loop is repeated until $\mathcal{F}_1$ remains nearly constant, i.e. $\epsilon \to 0$. The final goal is to drive the result to the upper bound of the feasible set of the network sum SE in (5.7).

The computational complexity of the proposed algorithm is determined by the number of iterations required and the complexity of updating each variable. The complexity of solving $\boldsymbol{\beta}$, $\boldsymbol{\gamma}$, and $\boldsymbol{\varepsilon}$ are $\mathcal{O}\left(BK(N_{\mathrm{t}} + BKq)\right)$. Let T_ω, T_μ, and T_ν represent the number of iterations for searching $\boldsymbol{\omega}$, $\boldsymbol{\mu}$, and $\boldsymbol{\nu}$**,** respectively. For the subproblem precoding optimization, the complexity of updating $\boldsymbol{w}$ is $\mathcal{O}(T_\omega B^2 K^2)$; for the subproblem BS antenna downtilting optimization, the complexity of updating $\boldsymbol{\alpha}$ is $\mathcal{O}\left(T_\mu T_\nu B^2 K^2\right)$. Define T_τ being the total number of the required iterations in Algorithm 5.1, the overall complexity of the proposed algorithm is $\mathcal{O}\left(T_\tau\left[B^2K^2\left(q + T_\omega + T_\mu T_\nu\right) + BKN_{\mathrm{t}}\right]\right)$.

5.4 Simulation Results

Table 5.2 Simulation Settings

Parameter	**Value**
Number of active URAs, B	9
Cell radius, D	50 m

BS height, h_{b}	10 m
User height, h_{u}	1.5 m
Number of transmit antennas at a URA in azimuth dimension, N_{az}	16
Number of transmit antennas at a URA in elevation dimension, N_{el}	32
Number of users in a cell, K	1
Number of receive antennas at a user	1
Operating frequency, $1/\lambda$	28 GHz
Transmit power, P_{t}	30 dBm
Horizontal HPBW, $\varphi_{3\mathrm{dB}}$	65°
Vertical HPBW, $\theta_{3\mathrm{dB}}$	10°
Horizontal SLL, SLL_{az}	25 dB
Vertical SLL, SLL_{el}	20 dB
Number of selected beams for each channel, q	4

In this section, the performance of the proposed algorithm is evaluated by simulations. The impact of the number of URA elements, transmit power of URA, and BS height on the mm-Wave cellular network based on the proposed algorithm is analyzed. The performance of various benchmark schemes is also presented to demonstrate the significance of the joint optimization approach in the proposed algorithm. Based on the illustration in Fig. 5.1 from Section 5.2.1, a 3D mm-Wave cellular network system including 9 cells is considered for simulation. Selected channels are generated from $B = 9$ URAs across 7 BSs. Unless otherwise specified, the simulation parameters are set in Table 5.2.

The proposed algorithm is compared with the following benchmark schemes to evaluate the performance:

1. Precoding optimization: Fixing the BS antenna downtilt at $\alpha_{b,k} = \frac{\pi}{4}$ rad. The proposed algorithm is only applied for the precoding optimization.

2. BS antenna downtilting optimization: Fixing the precoding vector at $\boldsymbol{w}_{b,k} = \frac{\boldsymbol{h}_{b,k}}{\|\boldsymbol{h}_{b,k}\|}$. The proposed algorithm is only applied for the BS antenna downtilting optimization.
3. No elevation beamforming: The proposed algorithm is applied without elevation beamforming considered.

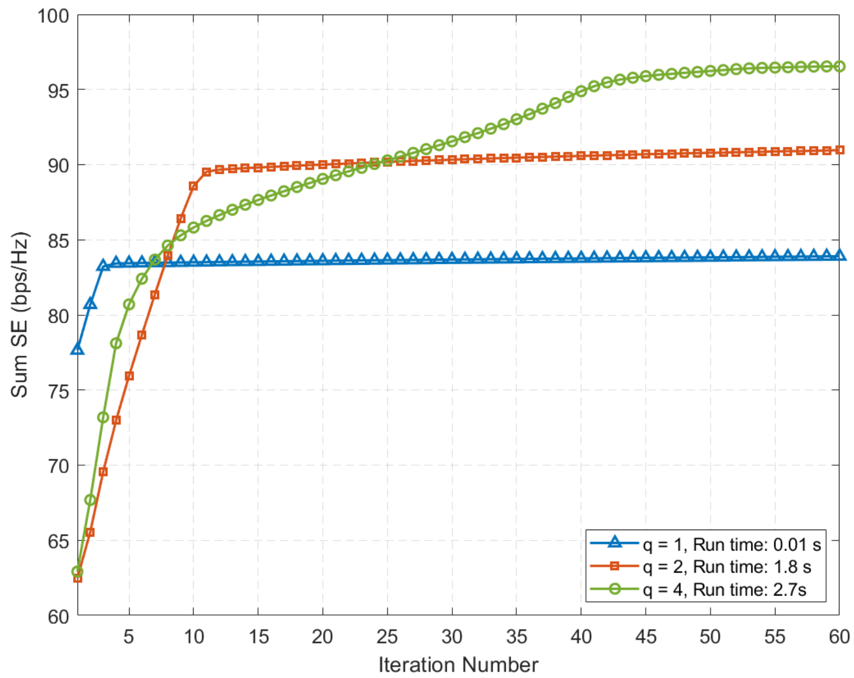

Fig. 5.2 Convergence of the proposed algorithm for different numbers of selected beams.

In Fig. 5.2, the convergence of the proposed algorithm for different numbers of selected beams is illustrated. It demonstrates that the network sum SE monotonically climbs over iterations and can converge to a stable value, which shows the feasibility of the proposed algorithm. Comparing the sum SE for different numbers of selected beams in a channel, it can be seen that the sum SE converges faster with fewer selected beams. Convergence of the network sum SE for the 1-beam selection scheme is reached within 4 iterations, whereas the 4-beam selection scheme requires 55 iterations to achieve convergence. However, when selecting more beams in a channel, the maximum sum SE at the joint optimal precoding vector and BS antenna downtilt is enhanced, and the time required to achieve it is highly acceptable.

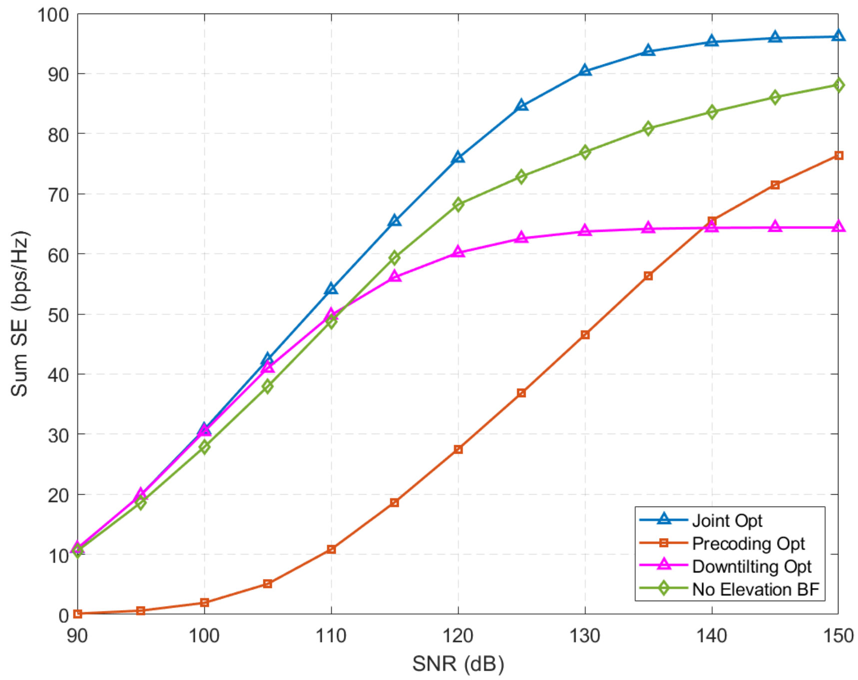

Fig. 5.3 Sum SE of a mm-Wave cellular network versus SNR for the proposed algorithm and different benchmark schemes.

The comparison among the proposed algorithm and the benchmark schemes is presented in Fig. 5.3. It illustrates that the sum SE of the proposed algorithm and benchmark schemes monotonically increase, with the sum SE of the proposed algorithm converging to a deterministic constant at a high SNR. The proposed algorithm outperforms the other schemes. Specifically, the sum SE of the proposed algorithm achieves an increase of 9% compared to the precoding optimization, and of 50% compared to the BS antenna downtilting optimization. In addition, the impact of the BS antenna downtilt on the mm-Wave cellular network sum SE is demonstrated. Inappropriate BS antenna downtilt adjustment reduces the desired signal while increasing inter-cell interference due to the narrow vertical beamwidth.

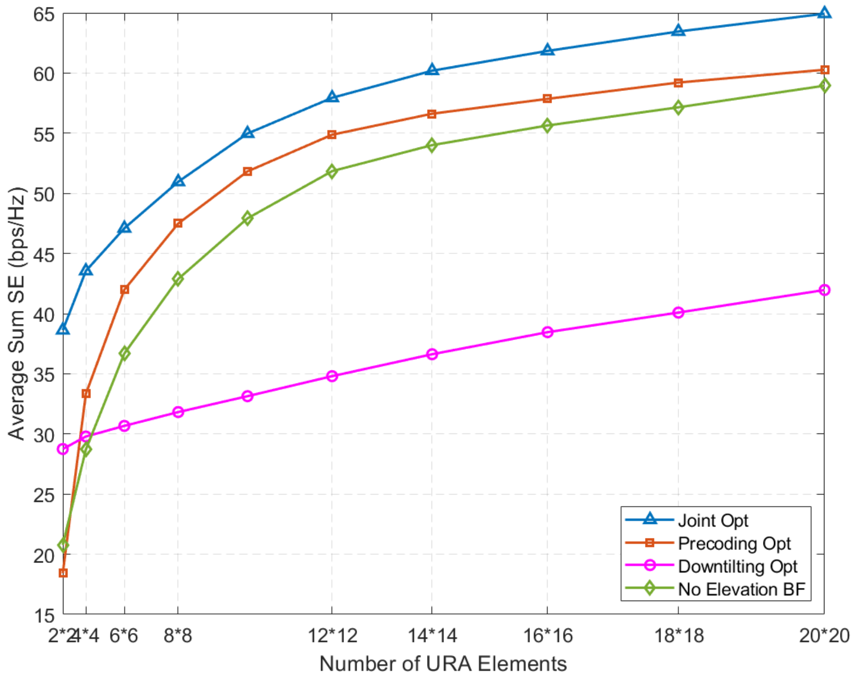

Fig. 5.4 Network average sum SE versus the number of URA elements for the proposed algorithm and different benchmark schemes.

In Fig. 5.4, the impact of the number of URA elements on the average sum SE is investigated. The curves are obtained by averaging the instantaneous sum SE for the network over 1×10^4 independent random realizations. The shape of URA is maintained as square, with the number of elements in each dimension ranging from 2 to 20. It is observed that the network sum SE goes up as the increase of the number of URA elements. This is because the increase in URA antenna elements enhances the beam selection accuracy, thereby boosting the desired signal while reducing interference. Furthermore, the proposed algorithm consistently outperforms other benchmark schemes in terms of the sum SE, which illustrates the efficacy of the proposed algorithm.

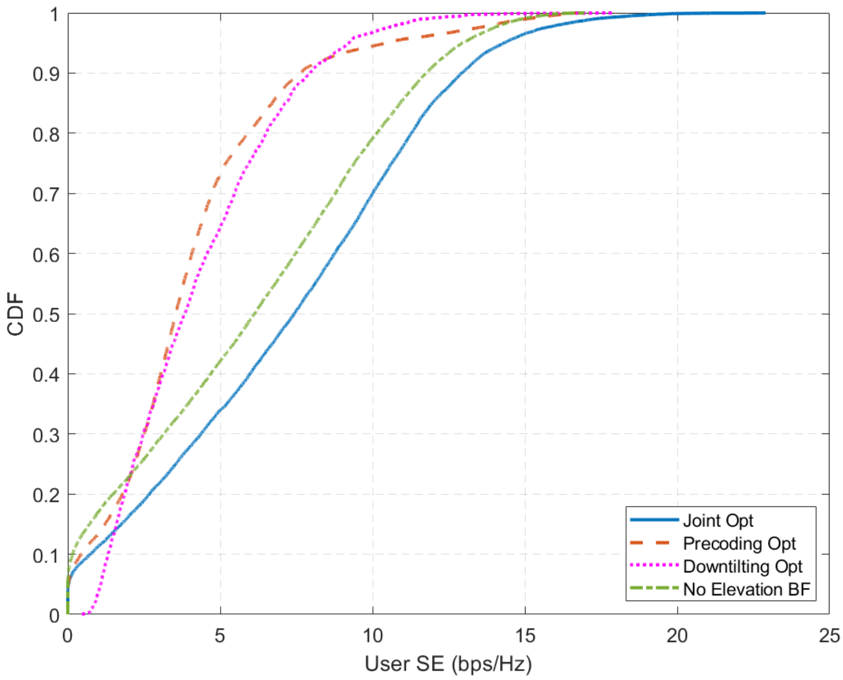

Fig. 5.5 Comparison of users' SE CDF over the coverage area for the proposed algorithm and various benchmark schemes.

Finally, the cumulative distribution function (CDF) of SE per user over the coverage area in the mm-Wave cellular network is presented in Fig. 5.5. It is evident that by applying the proposed algorithm, the upper limit of users' maximum SE and the probability of users experiencing high SE both significantly increase compared to other benchmark schemes. With precoding optimized, the probability of users with low SE decreases further through the application and optimization of the BS antenna downtilting. Moreover, it can be seen that applying the elevation beamforming reduces the probability of users experiencing low SE. This occurs as cell-edge users, who typically fall within the low SE region, benefit from narrow vertical beams that mitigate inter-cell interference. However, the proposed algorithm achieves a higher probability of users experiencing low SE than the BS antenna downtilting optimization alone, since unoptimized precoding reduces the desired signal for a cell-edge user while also suppressing inter-cell interference for users at the edges of neighboring cells.

5.5 Summary

In this chapter, based on the multi-cell mm-Wave downlink transmission model presented in Chapter 4, a sum SE maximization problem for the mm-Wave cellular network is formulated under the constraints of transmit power and the adjustable range of downtilt angles. To address the complex intractable NLP problem, a joint optimization algorithm is then developed by decomposing the original problem into two sub-problems and employing the AO technique combined with the FP approach to obtain closed-form expressions for the optimal precoding vector and BS antenna downtilt. Simulation results indicate the feasibility of the proposed algorithm by showing the convergence of the network sum SE. Furthermore, the proposed algorithm demonstrates its effectiveness in enhancing the sum SE, as evidenced by comparisons with various benchmark schemes. This highlights the benefits of joint optimization and elevation beamforming.

Chapter 6

Impact of 3D Antenna Radiation Pattern on Heterogeneous Cellular Networks

6.1 Introduction

HTCN, which consists of multiple tiers of BSs, such as macro-cell, pico-cell, and femto-cell BSs, is a key technology of the 5G mobile networks [66], [175]. In HTCNs, MBSs typically provide outdoor coverage and support high-speed users, while SBSs provide high capacity to indoor users and outdoor cell-edge users [176]. However, small cells lead to more cell-edge areas, making the aggregate interference environment and the corresponding interference management more complicated in HTCNs than in conventional single-tier cellular networks [177].

HTCNs have been modeled and analyzed using tools from SG on a 2D plane, where beamforming adjusts only the azimuth angle of a beam while the elevation angle is fixed [19], [142], [178], [179]. However, as the BS density increases and the BS-to-user distances decrease in HTCNs, the heights of BSs and users can no longer be ignored [180]. Under a 3D channel model, 3D beamforming that adjusts the beam angle in both the horizontal and vertical planes can be used to enhance the received signal and mitigate interference by steering a main beam of the BS radiation pattern to an intended user [7], [158].

In this chapter, the impact of the BS antenna vertical pattern and downtilt on the downlink spatially-averaged coverage probability, cell-edge average coverage probability, ASE, and EE of a two-tier HTCN comprising MBSs and SBSs is investigated. The optimal BS antenna downtilts of both tiers that maximize the downlink spatially-averaged coverage probability, ASE, and EE are derived. Furthermore, useful insights into the 3D deployment of BSs in HTCNs are provided based on the analytical and simulation results.

6.1.1 Related Works and Motivation

SG has been widely explored to evaluate the performance of cellular networks. In [155], the authors analyzed the downlink coverage probability of a single-tier cellular network leveraging SG, where the locations of BSs and users were modeled following independent HPPPs. For HTCNs, due to the differences in transmit power and BS antenna height between MBSs and SBSs, a bias value needs to be added to the received signal of users in the small-cell tier to balance the load between the macro-cell and small-cell tiers in HTCNs [181]. The authors in [142] showed that adding a positive bias to the received power from SBSs in an HTCN can improve the coverage probability, average ergodic rate, and minimum average user throughput even though the SINR of some cell-edge users decreases. The authors in [149] optimized the cell association bias and traffic offloading fraction to maximize the rate coverage in an HTCN. The authors in [182] optimized the cell association bias to maximize the mean downlink SINR in multi-antenna HTCNs. In [183], the EE of a multi-tier HTCN was maximized by considering potentially different BS heights and multi-antenna transmission. In [184], the impact of beamforming alignment errors on the coverage probability in a millimeter-wave HTCN was investigated using different path loss models, whereas the BS vertical antenna pattern was not taken into account, and the antenna gain was assumed to be constant. The authors in [141] analyzed the coverage probability and average SE with the minimum biased transmission distance scheme in an HTCN. In 3D HTCNs, as the heights of MBSs are larger than SBSs, the traffic in the small-cell tier is overloaded when adopting the minimum 3D transmission distance-based user association scheme. Therefore, a bias in terms of 3D transmission distance towards users located at the small-cell edge is considered to offload these users to the macro-cell tier [143].

Recently, 3D beamforming has been proposed to improve the performance of HTCNs [185]–[187]. In [185], a beamforming angle selection scheme was proposed to restrain intra-cell and inter-cell interference in a downlink multi-cell HTCN. In [186], the authors proposed an interference coordination algorithm by leveraging the statistical CSI and MBS antenna downtilting to balance the ergodic rate and traffic load among different tiers. The authors in [187] simulated the impact of the pico-cell antenna downtilt and vertical beamwidth on the coverage probability and ASE of an HTCN by leveraging the maximum average SIR user association scheme. The impact of pico-cell BS antenna downtilt, antenna vertical beamwidth, and pico-cell density on the coverage probability and SE of a two-tier HTCN was investigated in [188], while the impact of the number of dipole antenna elements and SBS antenna downtilt on the ASE and average user SE were studied in [189]. It is noted that in the aforementioned works, the effect of BS antenna downtilt was studied either via Monte Carlo simulations with high computational complexity or by numerically solving an intractable optimization problem. The authors in [16] modeled a two-tier HTCN using the SG and maximized the EE of the HTCN by optimizing the MBSs' antenna downtilts for different femto-cell BS densities, whereas the BS heights and antenna downtilts in the small-cell tier were ignored.

In summary, the existing works have not studied the BS antenna downtilts across all tiers of an HTCN, thus missing the opportunity to further enhance the HTCN performance, e.g., the downlink coverage probability, ASE, or EE, by jointly optimizing the BS antenna downtilts in different tiers.

6.1.2 Contributions

In this chapter, the joint optimization of the BS antenna downtilts across different tiers is investigated to enhance the downlink spatially-averaged coverage probability, ASE, and EE in a 3D two-tier HTCN comprising MBSs and SBSs. The locations of multi-antenna MBSs and SBSs are modeled using two independent HPPPs, and variations in BS heights and BS radiation patterns are modeled. The main contributions of this work are summarized as follows.

Spatially-averaged coverage probability, ASE, and EE analysis for 3D two-tier HTCNs:

A 3D system model for a two-tier HTCN with multi-antenna BSs is proposed, where the BS antenna downtilts and BS antenna heights of both tiers are modeled, and each user is served by the BS whose antennas have the shortest biased distance to the user (i.e., the SBS antenna-to-user distance is scaled by a positive bias for cell-association decisions). Assuming that BS antennas in each tier have the same downtilt and height, the expressions for the per-tier association probability are derived, representing the probability that a user is associated with a BS of a certain tier, and the downlink coverage probability of a user conditional on being associated with a certain tier. Based on these two expressions, expressions for the downlink spatially-averaged coverage probability, ASE, and EE as functions of the BS antenna downtilts, heights, and densities for both tiers, and the SBS association bias are obtained. Moreover, to facilitate fast numerical evaluation, an accurate approximation for the integral parts in the spatially-averaged coverage probability expression is proposed. The accuracy of the derived analytical expressions is validated by Monte Carlo simulations. The analytical results provide useful guidance for optimizing the BS antenna downtilts, heights, and densities in 3D two-tier HTCNs.

Cell-edge coverage probability case study:

Based on the derived expressions for the downlink spatially-averaged coverage probability, the lower bound average coverage probability for cell-edge users is obtained for a 3D two-tier HTCN with unbiased association and equal path loss components. In this scenario, a closed-form expression for the cell-edge average coverage probability is derived, offering valuable insights into the practical configuration of BS transmit power, antenna downtilts, heights, and densities for both macro-cell and small-cell tiers.

Joint optimization of MBS and SBS antenna downtilts for maximizing the downlink spatially-averaged coverage probability:

The optimal pair of MBS and SBS antenna downtilts that maximize the downlink spatially-averaged coverage probability is calculated by taking the partial derivative of the derived spatially-averaged coverage probability expression with respect to the MBS (SBS) antenna downtilt, respectively, then letting the partial derivative equal zero and solving the resulting equation for the MBS (SBS) antenna downtilt. The bisection method is used to find the solutions of partial derivative equations, where a restriction on the MBS (SBS) main beam downtilt values is imposed according to the side lobe level and solves the equations iteratively. The solution of each equation is the stationary point of the spatially-averaged coverage probability with respect to the BS antenna downtilt. As the stationary point could be the maximum, the minimum, or the saddle point, a second derivative test is proposed to verify the uniqueness and the type of the stationary point to guarantee that the obtained solution corresponds to the maximum coverage probability. The optimal pair of MBS and SBS antenna downtilts are obtained for different SBS heights and densities. The corresponding downlink spatially-averaged coverage probability, ASE, and EE are compared to the benchmark schemes that do not consider the BS antenna downtilts.

The remainder of this chapter is organized as follows. In Section 6.2, the system model of 3D HTCNs is presented. In Section 6.3, the expressions of the downlink spatially-averaged coverage probability, cell-edge average coverage probability, ASE, and EE are derived as functions of antenna downtilts of MBSs and SBSs. The method for finding the optimal pair of MBS and SBS antenna downtilts is proposed in Section 6.4. The numerical and simulation results are presented in Section 6.5. Finally, this chapter is summarized in Section 6.6.

6.2 System Model

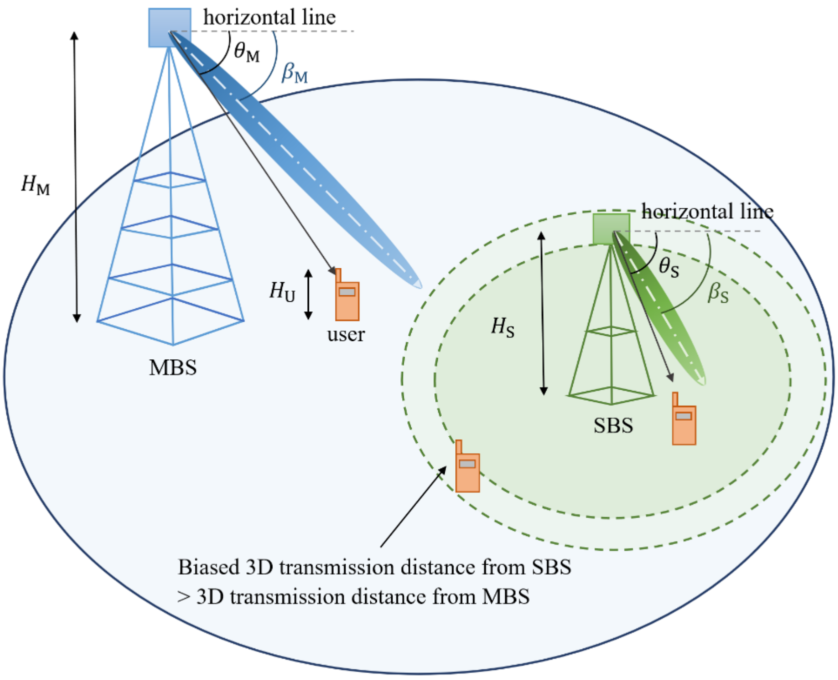

Fig. 6.1 A two-tier HTCN consisting of MBSs and SBSs with the minimum biased 3D transmission distance user association scheme.

A two-tier HTCN consisting of MBSs and SBSs is considered, as shown in Fig. 6.1. MBSs and SBSs are distributed on the ground following two independent HPPPs, Φ_{M} and Φ_{S}, with densities λ_{M} and λ_{S}, respectively. It is assumed that the BSs of the same tier have identical transmit power and height, where the MBS transmit power and SBS transmit power are denoted by P_{M} and P_{S}, respectively, and the MBS and SBS heights are denoted by H_{M} and H_{S}, respectively. Users are distributed in the network area following another independent HPPP Φ_{U}. Each user has a single antenna with the same height of H_{U}. Given that the largest received signal power-based user association scheme may lead to a heavy load for high-power MBSs in a heterogeneous network, and the smallest path loss-based user association scheme ignores the tier-specific user association bias that has been widely considered for load balancing in heterogeneous networks [190], the shortest biased transmission distance-based user association strategy is adopted. It has been shown in [143] that this strategy can achieve the same coverage probability as the largest received signal power-based user association strategy by adjusting the tier-specific user association bias. Specifically, each user is associated with the BS that has the shortest biased transmission distance from the BS antenna to the user antenna, where the SBS antenna-to-user antenna distance is scaled by a positive bias, $B_{\mathrm{S}} > 1$, for use in cell-association decisions. Each MBS and each SBS have access to all the sub-channels of the network. It is assumed that each MBS is partitioned into s equal sectors, each covering an azimuth angular spread of $\frac{2\pi}{s}$ and being regarded as a macro-cell. The total number of sub-channels is divided into s orthogonal subsets of equal size, which are allocated to s sectors of an MBS.

The downlink adopts OFDMA in each cell, hence there is no intra-cell interference. It is assumed that each link sees independent Rayleigh fading with a unit average power gain. The path loss from MBS i ($i \in \Phi_{\mathrm{M}}$) or SBS j ($j \in \Phi_{\mathrm{S}}$) to a user is given respectively by

$$L_i^{\mathrm{M}} = \left(\left(d_i^{\mathrm{M}}\right)^2 + h_{\mathrm{M}}^2\right)^{-\frac{\alpha_{\mathrm{M}}}{2}}, \tag{6.1}$$

$$L_j^{\mathrm{S}} = \left(\left(d_j^{\mathrm{S}}\right)^2 + h_{\mathrm{S}}^2\right)^{-\frac{\alpha_{\mathrm{S}}}{2}}, \tag{6.2}$$

where $d_i^{\mathrm{M}}\left(d_j^{\mathrm{S}}\right)$ is the horizontal distance between a user and MBS i (SBS j); $h_{\mathrm{M}} = H_{\mathrm{M}} - H_{\mathrm{U}}$ and $h_{\mathrm{S}} = H_{\mathrm{S}} - H_{\mathrm{U}}$ denote the height difference between an MBS and a user and that between an SBS and a user, respectively, and are both assumed to be positive; α_{M} and α_{S} represent the path loss exponent for the macro-cell and small-cell tiers, respectively.

According to 3GPP [53] and existing works [191], [192], the antenna gain (in dBi) of each antenna equipped at MBS i or SBS j is given respectively by

$$G_i^{\mathrm{M}} = G_{\mathrm{M_h}} + G_{\mathrm{M_v}}\left(\theta_i^{\mathrm{M}}, \beta_{\mathrm{M}}\right) + G_{\mathrm{M_m}}, \tag{6.3}$$

$$G_j^{\mathrm{S}} = G_{\mathrm{S_h}} + G_{\mathrm{S_v}}\left(\theta_j^{\mathrm{S}}, \beta_{\mathrm{S}}\right) + G_{\mathrm{S_m}}, \tag{6.4}$$

where $G_{\mathrm{M_h}}$ and $G_{\mathrm{S_h}}$ are the horizontal gain of an MBS antenna and an SBS antenna, respectively; $G_{\mathrm{M_v}}\left(\theta_i^{\mathrm{M}}, \beta_{\mathrm{M}}\right)$ and $G_{\mathrm{S_v}}\left(\theta_j^{\mathrm{S}}, \beta_{\mathrm{S}}\right)$ denote the vertical pattern of an antenna at MBS i and SBS j, respectively; $\theta_i^{\mathrm{M}} = \tan^{-1}\left(\frac{h_{\mathrm{M}}}{d_i^{\mathrm{M}}}\right)$ and $\theta_j^{\mathrm{S}} = \tan^{-1}\left(\frac{h_{\mathrm{S}}}{d_j^{\mathrm{S}}}\right)$ are the physical AoD from MBS i or SBS j to a user, respectively; β_{M} and β_{S} are the electrical downtilts of antennas at MBSs and SBSs, respectively; $G_{\mathrm{M_m}}$ and $G_{\mathrm{S_m}}$ are the maximum antenna gains of MBS and SBS antennas, respectively.

Assuming that each antenna element is a dipole, the vertical pattern of an antenna at MBS i and SBS j can be approximated by [53] and [59]

$$G_{\mathrm{M_v}}\left(\theta_i^{\mathrm{M}}, \beta_{\mathrm{M}}\right) = \max\left[-12\left(\frac{\theta_i^{\mathrm{M}} - \beta_{\mathrm{M}}}{\theta_{\mathrm{3dB}}}\right)^2, SLL_{\mathrm{M}}\right], \tag{6.5}$$

$$G_{\mathrm{S_v}}\left(\theta_j^{\mathrm{S}}, \beta_{\mathrm{S}}\right) = \max\left[10\log_{10}\left|\cos^{n_{\mathrm{S}}}\left(\theta_j^{\mathrm{S}} - \beta_{\mathrm{S}}\right)\right|, SLL_{\mathrm{S}}\right], \tag{6.6}$$

where θ_{3dB} is the HPBW of the MBS antenna radiation pattern; n_{S} is a parameter determined by the beamwidth of the SBS antenna radiation pattern [59]; SLL_{M} and SLL_{S} are the sidelobe levels in the vertical plane of the MBS antenna pattern and the SBS antenna pattern, respectively.

Since the horizontal radiation pattern of antennas is symmetric, sectorizing all MBSs to modify the antenna patterns does not have significant impacts on the SIR of the desired user. It is assumed that the antenna patterns for all BSs are omni-directional in the horizontal plane, and the horizontal antenna gain from an MBS antenna equals to that from s sectors with the same sub-channel. Based on these assumptions, the effective density of interfering sectors from other MBSs to an MBS user is set as $\frac{\lambda_{\mathrm{M}}}{s}$, and the effective MBS distribution is denoted as an HPPP Φ'_{M} with density $\frac{\lambda_{\mathrm{M}}}{s}$ [16].

Without loss of generality, a typical user located at the origin of the 2D ground plane is considered [142], [193]. The SIR of the typical user served by MBS i or SBS j in an arbitrary sub-channel is respectively expressed as

$$SIR_i^{\mathrm{M}} = \frac{g_i^{\mathrm{M}} P_{\mathrm{M}} L_i^{\mathrm{M}} G_i^{\mathrm{M}}}{I_k^{\mathrm{M}} + I_{\mathrm{S}}^{\mathrm{M}}}, \tag{6.7}$$

$$SIR_j^{\mathrm{S}} = \frac{g_j^{\mathrm{S}} P_{\mathrm{S}} L_j^{\mathrm{S}} G_j^{\mathrm{S}}}{I_l^{\mathrm{S}} + I_{\mathrm{M}}^{\mathrm{S}}}, \tag{6.8}$$

where

$$I_k^{\mathrm{M}} = \sum_{k \in \Phi'_{\mathrm{M}} \setminus \{i\}} g_k^{\mathrm{M}} P_{\mathrm{M}} L_k^{\mathrm{M}} G_k^{\mathrm{M}},$$

$$I_{\mathrm{S}}^{\mathrm{M}} = \sum_{l \in \Phi_{\mathrm{S}}} g_l^{\mathrm{M}} P_{\mathrm{S}} L_l^{\mathrm{M}} G_l^{\mathrm{M}},$$

$$I_l^{\mathrm{S}} = \sum_{l \in \Phi_{\mathrm{S}} \setminus \{j\}} g_l^{\mathrm{S}} P_{\mathrm{S}} L_l^{\mathrm{S}} G_l^{\mathrm{S}},$$

$$I_{\mathrm{M}}^{\mathrm{S}} = \sum_{k \in \Phi'_{\mathrm{M}}} g_k^{\mathrm{S}} P_{\mathrm{M}} L_k^{\mathrm{S}} G_k^{\mathrm{S}},$$

denote the macro-cell tier interference and small-cell tier interference to the typical user served by MBS i, and the small-cell tier interference and macro-cell tier interference to the typical user served by SBS j, respectively; g_i^{M} and g_j^{S} denote the Rayleigh fading power gains of the links from MBS i ($\forall i \in \Phi_{\mathrm{M}}$) and SBS j ($\forall i \in \Phi_S$) to the typical user, respectively, each following an independent and identical exponential distribution exp(1).

6.2.1 Tier Association

The coverage probability averaged over the spatial domain of the two-tier HTCN is defined as the probability that the SIR of the typical user is greater than a given threshold τ, and can be expressed as

$$p_{\mathrm{c}} = \mathcal{P}_{\mathrm{M}}\mathcal{A}_{\mathrm{M}} + \mathcal{P}_{\mathrm{S}}\mathcal{A}_{\mathrm{S}}, \tag{6.9}$$

where $\mathcal{P}_{\mathrm{M}}$ and $\mathcal{P}_{\mathrm{S}}$ are the spatially-averaged coverage probability conditional on the typical user being associated with an MBS or an SBS, respectively; $\mathcal{A}_{\mathrm{M}}$ and $\mathcal{A}_{\mathrm{S}}$ are the probability that the typical user is associated with an MBS or an SBS, respectively.

Let d_{M} and d_{S} denote the horizontal distances from the typical user to the nearest MBS and the nearest SBS, respectively. For use in the cell-association decision making, the biased distance from the closest MBS's antenna or the closest SBS's antenna to the typical user's antenna is written respectively as

$$D_{\mathrm{M}} = \sqrt{d_{\mathrm{M}}^2 + h_{\mathrm{M}}^2}, \tag{6.10}$$

$$D_{\mathrm{S}} = B_{\mathrm{S}}\sqrt{d_{\mathrm{S}}^2 + h_{\mathrm{S}}^2}. \tag{6.11}$$

If $d_{\mathrm{M}} < d_{\mathrm{S}}$, then the typical user is associated with the closest MBS; otherwise, the typical user is associated with the closest SBS. Accordingly, the spatially-averaged probability that the typical user is associated with an MBS is expressed as

$$\mathcal{A}_{\mathrm{M}} = \mathbb{E}_{d_{\mathrm{M}}}[\Pr(D_{\mathrm{M}} < D_{\mathrm{S}})] = \mathbb{E}_{d_{\mathrm{M}}}\left[\Pr\left(d_{\mathrm{S}}^2 > \frac{d_{\mathrm{M}}^2 + h_{\mathrm{M}}^2}{B_{\mathrm{S}}^2} - h_{\mathrm{S}}^2\right)\right]. \tag{6.12}$$

Let $\mathcal{R}_{\mathrm{M}} = \frac{d_{\mathrm{M}}^2 + h_{\mathrm{M}}^2}{B_{\mathrm{S}}^2} - h_{\mathrm{S}}^2$, then $\Pr(D_{\mathrm{M}} < D_{\mathrm{S}}) = 1$ if $\mathcal{R}_{\mathrm{M}} \leq 0$; if $\mathcal{R}_{\mathrm{M}} > 0$, it is obtained as

$$\begin{aligned}\mathcal{A}_{\mathrm{M}} &= \mathbb{E}_{d_{\mathrm{M}}}\left[\Pr\left(d_{\mathrm{S}} > \sqrt{\mathcal{R}_{\mathrm{M}}}\right)\right] \\ &= \mathbb{E}_{d_{\mathrm{M}}}\left[e^{-\lambda_{\mathrm{S}}\pi\mathcal{R}_{\mathrm{M}}}\right] \\ &= \int_0^{\gamma_{\mathrm{M}}} f_{d_{\mathrm{M}}}(r)dr + \int_{\gamma_{\mathrm{M}}}^{\infty} e^{-\lambda_{\mathrm{S}}\pi\mathcal{R}_{\mathrm{M}}} f_{d_{\mathrm{M}}}(r)dr \\ &= 1 - e^{-\lambda_{\mathrm{M}}\pi\gamma_{\mathrm{M}}^2} + e^{-\pi\left[\lambda_{\mathrm{M}}\gamma_{\mathrm{M}}^2 + \lambda_{\mathrm{S}}\left(\frac{\gamma_{\mathrm{M}}^2 + h_{\mathrm{M}}^2}{B_{\mathrm{S}}^2} - h_{\mathrm{S}}^2\right)\right]},\end{aligned} \quad (6.13)$$

where the second line of (6.13) is obtained using the null probability of an HPPP on a 2D plane [142], [155], $f_{d_{\mathrm{M}}}(r) = 2\pi\lambda_{\mathrm{M}} r e^{-\lambda_{\mathrm{M}}\pi r^2}$ is the PDF of d_{M} [155], and

$$\gamma_{\mathrm{M}} = \begin{cases} \sqrt{h_{\mathrm{S}}^2 B_{\mathrm{S}}^2 - h_{\mathrm{M}}^2}, & \text{if } h_{\mathrm{S}}^2 B_{\mathrm{S}}^2 \geq h_{\mathrm{M}}^2 \\ 0, & \text{if } h_{\mathrm{S}}^2 B_{\mathrm{S}}^2 < h_{\mathrm{M}}^2 \end{cases}. \quad (6.14)$$

Similarly, the spatially-averaged probability that the typical user is associated with the closest SBS is obtained as

$$\mathcal{A}_{\mathrm{S}} = 1 - \mathrm{e}^{-\lambda_{\mathrm{S}}\pi\gamma_{\mathrm{S}}^2} + \mathrm{e}^{-\pi\left[\lambda_{\mathrm{S}}\gamma_{\mathrm{S}}^2 + \lambda_{\mathrm{M}}\left((\gamma_{\mathrm{S}}^2 + h_{\mathrm{S}}^2)B_{\mathrm{S}}^2 - h_{\mathrm{M}}^2\right)\right]}, \quad (6.15)$$

where

$$\gamma_{\mathrm{S}} = \begin{cases} \sqrt{\left(\frac{h_{\mathrm{M}}}{B_{\mathrm{S}}}\right)^2 - h_{\mathrm{S}}^2}, & \text{if } \left(\frac{h_{\mathrm{M}}}{B_{\mathrm{S}}}\right)^2 \geq h_{\mathrm{S}}^2 \\ 0, & \text{if } \left(\frac{h_{\mathrm{M}}}{B_{\mathrm{S}}}\right)^2 < h_{\mathrm{S}}^2 \end{cases}. \quad (6.16)$$

6.3 Performance Analysis

In this section, the downlink spatially-averaged coverage probability, cell-edge average coverage probability, ASE, and EE are derived as functions of the MBS antenna downtilt and the SBS antenna downtilt for a 3D HTCN.

6.3.1 Spatially-averaged Coverage Probability

The spatially-averaged coverage probability conditional on the typical user being associated with an MBS is given by

$$\begin{aligned}
\mathcal{P}_{\mathrm{M}} &= \mathbb{E}_{d_i^{\mathrm{M}}}\left[\Pr\left(\mathrm{SIR}_i^{\mathrm{M}} > \tau\right)\right] \\
&= \int_0^{\infty} \left[\Pr\left(\mathrm{SIR}_i^{\mathrm{M}} > \tau\right)\right] f_{d_i^{\mathrm{M}}}(x)\mathrm{d}x \\
&= \int_0^{\infty} \left[\Pr\left[\frac{g_i^{\mathrm{M}} P_{\mathrm{M}} L_i^{\mathrm{M}} G_i^{\mathrm{M}}}{I_k^{\mathrm{M}} + I_{\mathrm{S}}^{\mathrm{M}}} > \tau\right]\right] f_{d_i^{\mathrm{M}}}(x)\mathrm{d}x \\
&= \int_0^{\infty} \left[\Pr\left[g_i^{\mathrm{M}} > \tau \frac{I_k^{\mathrm{M}} + I_{\mathrm{S}}^{\mathrm{M}}}{P_{\mathrm{M}} L_i^{\mathrm{M}} G_i^{\mathrm{M}}}\right]\right] f_{d_i^{\mathrm{M}}}(x)\mathrm{d}x \\
&= \int_0^{\infty} \left[\mathbb{E}_{I_k^{\mathrm{M}}, I_{\mathrm{S}}^{\mathrm{M}}}\left[\Pr\left(g_i^{M} > \frac{\tau\left(I_k^{\mathrm{M}} + I_{\mathrm{S}}^{\mathrm{M}}\right)}{P_{\mathrm{M}} L_i^{\mathrm{M}} G_i^{\mathrm{M}}}\right)\right]\right] f_{d_i^{\mathrm{M}}}(x)\mathrm{d}x \\
&\overset{(a)}{=} \int_0^{\infty} \left[\mathbb{E}_{I_k^{\mathrm{M}}, I_{\mathrm{S}}^{\mathrm{M}}}\left[\exp\left(-\tau \frac{I_k^{\mathrm{M}} + I_{\mathrm{S}}^{\mathrm{M}}}{P_{\mathrm{M}} L_i^{\mathrm{M}} G_i^{\mathrm{M}}}\right)\right]\right] f_{d_i^{\mathrm{M}}}(x)\mathrm{d}x \\
&= \int_0^{\infty} \mathcal{L}_{I_k^{\mathrm{M}}} \mathcal{L}_{I_{\mathrm{S}}^{\mathrm{M}}} f_{d_i^{\mathrm{M}}}(x)\mathrm{d}x,
\end{aligned} \tag{6.17}$$

where (a) follows $g_i^{\mathrm{M}} \sim \exp(1)$, $\mathcal{L}_{I_k^{\mathrm{M}}}$ and $\mathcal{L}_{I_{\mathrm{S}}^{\mathrm{M}}}$ are the Laplace transforms of I_k^{M} and $I_{\mathrm{S}}^{\mathrm{M}}$, respectively. Utilizing the definition of Laplace transform yields, $\mathcal{L}_{I_k^{\mathrm{M}}}$ and $\mathcal{L}_{I_{\mathrm{S}}^{\mathrm{M}}}$ can be calculated as

$$\begin{aligned}
\mathcal{L}_{I_k^{\mathrm{M}}} &= \mathbb{E}_{I_{\mathrm{M}}}\left[e^{-\frac{\tau}{P_{\mathrm{M}} L_i^{\mathrm{M}} G_i^{\mathrm{M}}} I_k^{\mathrm{M}}}\right] \\
&= \mathbb{E}_{\Phi'_{\mathrm{M}}}\left[\exp\left(-\frac{\tau}{P_{\mathrm{M}} L_i^{\mathrm{M}} G_i^{\mathrm{M}}} \sum_{k \in \Phi'_{\mathrm{M}} \setminus \{i\}} g_k^{\mathrm{M}} P_{\mathrm{M}} L_k^{\mathrm{M}} G_k^{\mathrm{M}}\right)\right] \\
&\overset{(b)}{=} \exp\left[\frac{-2\pi\lambda_{\mathrm{M}}}{s} \int_x^{\infty} \left\{1 - \mathcal{L}_{g_{\mathrm{M}}}\left(\frac{\tau L_k^{\mathrm{M}} G_k^{\mathrm{M}}}{L_i^{\mathrm{M}} G_i^{\mathrm{M}}}\right)\right\} d_k^{\mathrm{M}} \mathrm{d}d_k^{\mathrm{M}}\right] \\
&= \exp\left[\frac{-2\pi\lambda_{\mathrm{M}}}{s} \int_x^{\infty} \frac{d_k^{\mathrm{M}}}{1 + \mathcal{K}_k^{\mathrm{M}} \frac{G_i^{\mathrm{M}}}{G_k^{M}}} \mathrm{d}d_k^{M}\right],
\end{aligned} \tag{6.18}$$

$$\begin{aligned}
\mathcal{L}_{I_{\mathrm{S}}^{\mathrm{M}}} &= \mathbb{E}_{I_{\mathrm{M}}}\left[e^{-\frac{\tau}{P_{\mathrm{M}} L_i^{\mathrm{M}} G_i^{\mathrm{M}}} I_{\mathrm{S}}^{\mathrm{M}}}\right] \\
&= \mathbb{E}_{\Phi_{\mathrm{S}}}\left[\exp\left(-\frac{\tau}{P_{\mathrm{M}} L_i^{\mathrm{M}} G_i^{\mathrm{M}}} \sum_{l \in \Phi_{\mathrm{S}}} g_l^{\mathrm{M}} P_{\mathrm{S}} L_l^{\mathrm{M}} G_j^{\mathrm{M}}\right)\right] \\
&= \exp\left[-2\pi\lambda_{\mathrm{S}} \int_{W_{\mathrm{M}}}^{\infty} \left\{1 - \mathcal{L}_{g_{\mathrm{S}}}\left(\frac{\tau P_{\mathrm{S}} L_l^{\mathrm{M}} G_l^{\mathrm{M}}}{P_{\mathrm{M}} L_i^{\mathrm{M}} G_i^{\mathrm{M}}}\right)\right\} d_l^{\mathrm{M}} \mathrm{d} d_l^{\mathrm{M}}\right] \\
&= \exp\left[-2\pi\lambda_{\mathrm{S}} \int_{W_{\mathrm{M}}}^{\infty} \frac{d_l^{\mathrm{M}}}{1 + \mathcal{K}_{\mathrm{S}}^{\mathrm{M}} \frac{G_i^{\mathrm{M}}}{G_l^{\mathrm{M}}}} \mathrm{d} d_l^{\mathrm{M}}\right],
\end{aligned} \tag{6.19}$$

where (b) follows from the probability generating functional of the PPP [194]; $\mathcal{K}_k^{\mathrm{M}} = \frac{L_i^{\mathrm{M}}}{\tau L_k^{\mathrm{M}}}$ and $\mathcal{K}_{\mathrm{S}}^{\mathrm{M}} = \frac{P_{\mathrm{M}} L_i^{\mathrm{M}}}{\tau P_{\mathrm{S}} L_l^{\mathrm{M}}}$; W_{M} is the minimum horizontal distance from the typical user to an interfering MBS. Since the serving MBS is the nearest MBS in the shortest biased transmission distance cell-association scheme, according to (6.12), W_{M} is given by

$$W_{\mathrm{M}} = \begin{cases} \sqrt{\dfrac{x^2 + h_{\mathrm{M}}^2}{B_{\mathrm{S}}^2} - h_{\mathrm{S}}^2}, & \text{if } x \geq \gamma_{\mathrm{M}} \\ 0, & \text{if } x < \gamma_{\mathrm{M}} \end{cases}. \tag{6.20}$$

Let t represent the tier index that the typical user is associated with. When the typical user is associated with the macro-cell tier, the PDF of d_i^{M} is expressed as

$$\begin{aligned}
f_{d_i^{\mathrm{M}}}(x) &= \frac{\mathrm{d}\{\Pr[x < d_i^{\mathrm{M}}]\}}{\mathrm{d}x} \\
&= \frac{\Pr[x < d_{\mathrm{M}}, t = \mathrm{M}]}{\Pr[t = \mathrm{M}] \cdot \mathrm{d}x},
\end{aligned} \tag{6.21}$$

where $\Pr[t = \mathrm{M}] = \mathcal{A}_{\mathrm{M}}$ follows from the definition of $\mathcal{A}_{\mathrm{M}}$, and

$$\Pr[x < d_{\mathrm{M}}, t = \mathrm{M}] = \int_x^{\infty} \Pr[D_{\mathrm{M}} < D_{\mathrm{S}}] f_{d_{\mathrm{M}}}(r)\,\mathrm{d}r. \tag{6.22}$$

Inserting (6.22) into (6.21), the PDF of d_i^{M} can be written as

$$f_{d_i^{\mathrm{M}}}(x) = \begin{cases} \frac{2\pi\lambda_{\mathrm{M}}}{\mathcal{A}_{\mathrm{M}}} x e^{-\lambda_{\mathrm{M}}\pi x^2}, & \text{if } x < \gamma_{\mathrm{M}} \\ \frac{2\pi\lambda_{\mathrm{M}}}{\mathcal{A}_{\mathrm{M}}} x e^{-\pi\left[x^2\left(\lambda_{\mathrm{M}}+\frac{\lambda_{\mathrm{S}}}{B_{\mathrm{S}}^2}\right)+Z_{\mathrm{M}}\right]}, & \text{if } x \geq \gamma_{\mathrm{M}} \end{cases} \quad (6.23)$$

where $Z_{\mathrm{M}} = \lambda_{\mathrm{S}}\left(\left(\frac{h_{\mathrm{M}}}{B_{\mathrm{S}}}\right)^2 - h_{\mathrm{S}}^2\right)$.

Similarly, the spatially-averaged coverage probability conditional on the typical user being associated with an SBS is obtained as

$$\begin{aligned} \mathcal{P}_{\mathrm{S}} &= \mathbb{E}_{d_j^{\mathrm{S}}}\left[\Pr\left(\mathrm{SIR}_j^{\mathrm{S}} > \tau\right)\right] \\ &= \int_0^\infty \left[\Pr\left(\mathrm{SIR}_j^{\mathrm{S}} > \tau\right)\right] f_{d_j^{\mathrm{S}}}(y)\mathrm{d}y \\ &= \int_0^\infty \mathcal{L}_{I_l^{\mathrm{S}}}\mathcal{L}_{I_{\mathrm{M}}^{\mathrm{S}}} f_{d_j^{\mathrm{S}}}(y)\mathrm{d}y. \end{aligned} \quad (6.24)$$

where $\mathcal{L}_{I_l^{\mathrm{S}}}$ and $\mathcal{L}_{I_{\mathrm{M}}^{\mathrm{S}}}$ are the Laplace transforms of I_l^{S} and $I_{\mathrm{M}}^{\mathrm{S}}$ respectively, and can be calculated by

$$\mathcal{L}_{I_l^{\mathrm{S}}} = \exp\left[-2\pi\lambda_{\mathrm{S}} \int_y^\infty \frac{d_l^{\mathrm{S}}}{1 + \mathcal{K}_l^{\mathrm{S}} \frac{G_j^{\mathrm{S}}}{G_l^{\mathrm{S}}}} \mathrm{d}d_l^{\mathrm{S}}\right], \quad (6.25)$$

$$\mathcal{L}_{I_{\mathrm{M}}^{\mathrm{S}}} = \exp\left[\frac{-2\pi\lambda_{\mathrm{M}}}{s} \int_{W_{\mathrm{S}}}^\infty \frac{d_k^{\mathrm{S}}}{1 + \mathcal{K}_{\mathrm{M}}^{\mathrm{S}} \frac{G_j^{\mathrm{S}}}{G_k^{\mathrm{S}}}} \mathrm{d}d_k^{\mathrm{S}}\right], \quad (6.26)$$

where $\mathcal{K}_l^{S} = \frac{L_j^{\mathrm{S}}}{\tau L_l^{\mathrm{S}}}$ and $\mathcal{K}_{\mathrm{M}}^{\mathrm{S}} = \frac{P_S L_j^{\mathrm{S}}}{\tau P_{\mathrm{M}} L_k^{\mathrm{S}}}$; W_{S} is the minimum horizontal distance from the typical user to an interfering SBS and is given by

$$W_{\mathrm{S}} = \begin{cases} \sqrt{(y^2 + h_{\mathrm{S}}^2)B_{\mathrm{S}}^2 - h_{\mathrm{M}}^2}, & \text{if } y \geq \gamma_{\mathrm{S}} \\ 0, & \text{if } y < \gamma_{\mathrm{S}} \end{cases}. \tag{6.27}$$

In addition, the PDF of d_j^{S} is expressed as

$$f_{d_j^{\mathrm{S}}}(y) = \begin{cases} \dfrac{2\pi\lambda_{\mathrm{S}}}{\mathcal{A}_{\mathrm{S}}} y e^{-\lambda_{\mathrm{S}}\pi y^2}, & \text{if } y < \gamma_{\mathrm{S}} \\ \dfrac{2\pi\lambda_{\mathrm{S}}}{\mathcal{A}_{\mathrm{S}}} y e^{-\pi[y^2(\lambda_{\mathrm{S}}+\lambda_{\mathrm{M}}B_{\mathrm{S}}^2)+Z_{\mathrm{S}}]}, & \text{if } y \geq \gamma_{\mathrm{S}} \end{cases}, \tag{6.28}$$

where $Z_{\mathrm{S}} = \lambda_{\mathrm{M}}(h_{\mathrm{S}}^2 B_{\mathrm{S}}^2 - h_{\mathrm{M}}^2)$.

To simplify the numerical calculation for the conditional spatially-averaged coverage probabilities, the Gaussian quadrature method is leveraged to approximate the integral parts [195]. Letting $\mathcal{F}(x) = \mathcal{L}_{I_k^{\mathrm{M}}}\mathcal{L}_{I_{\mathrm{S}}^{\mathrm{M}}} f_{d_i^{\mathrm{M}}}(x)$, (6.17) can be approximated by

$$\begin{aligned} \mathcal{P}_{\mathrm{M}} &= \int_0^{\infty} \mathcal{F}(x)\mathrm{d}x \\ &\overset{(c)}{=} \frac{\zeta}{2}\int_{-1}^{1} \mathcal{F}\left(\frac{\zeta}{2}\omega + \frac{\zeta}{2}\right)\mathrm{d}\omega \\ &= \frac{\zeta}{2}\int_{-1}^{1} \frac{\mathcal{F}\left(\frac{\zeta}{2}\omega + \frac{\zeta}{2}\right)\sqrt{1-\omega^2}}{\sqrt{1-\omega^2}}\mathrm{d}\omega \\ &\overset{(d)}{\approx} \frac{\zeta\pi}{2Q}\left[\sum_{q=1}^{Q} \mathcal{F}\left(\frac{\zeta}{2}\omega_q + \frac{\zeta}{2}\right)\sqrt{1-\omega_q^2}\right], \end{aligned} \tag{6.29}$$

where $\zeta \to \infty$ denotes the largest possible distance from the typical user, $\omega_q = \frac{2}{\zeta}\cos\left(\frac{2q-1}{2Q}\pi\right) - 1, q = 1, \ldots, Q$, and Q is the sample size, which determines the accuracy of this approximation, (c) is obtained by substituting $x = \frac{\zeta}{2}\omega + \frac{\zeta}{2}$ into the integral of the first line, and (d) follows from Chebyshev-Gauss quadrature [195].

Letting $\mathcal{G}(d_k^{\mathrm{M}}) = \frac{d_k^{\mathrm{M}}}{1+\left(\mathcal{K}_{\mathrm{M}} P_{\mathrm{M}} L_k^{\mathrm{M}} G_k^{\mathrm{M}}\right)^{-1}}$ and $\mathcal{H}(d_l^{\mathrm{M}}) = \frac{d_l^{\mathrm{M}}}{1+\left(\mathcal{K}_{\mathrm{M}} P_{\mathrm{S}} L_l^{\mathrm{M}} G_l^{\mathrm{M}}\right)^{-1}}$, where $\mathcal{K}_{\mathrm{M}} = \frac{\tau}{P_{\mathrm{M}} L_i^{\mathrm{M}} G_i^{\mathrm{M}}}$, (6.18) and (6.19) can be written as

$$\begin{aligned}
\mathcal{L}_{I_k^{\mathrm{M}}} &= \exp\left[\frac{-2\pi\lambda_{\mathrm{M}}}{s}\int_x^{\zeta} \mathcal{G}(d_k^{\mathrm{M}})\mathrm{d}d_k^{\mathrm{M}}\right] \\
&= \exp\left[\frac{-\pi\lambda_{\mathrm{M}}}{s}(\zeta - x)\int_{-1}^{1} \mathcal{G}\left(\frac{\zeta - x}{2}u_{\mathrm{M}} + \frac{\zeta + x}{2}\right)\mathrm{d}u_{\mathrm{M}}\right] \\
&= \exp\left\{\frac{-\pi^2\lambda_{\mathrm{M}}}{sC}(\zeta - x)\sum_{c=1}^{C}\left[\mathcal{G}\left(\frac{\zeta - x}{2}u_c^C + \frac{\zeta + x}{2}\right)\sqrt{1 - (u_c^C)^2}\right]\right\},
\end{aligned} \tag{6.30}$$

$$\begin{aligned}
\mathcal{L}_{I_{\mathrm{S}}^{\mathrm{M}}} &= \exp\left[-2\pi\lambda_{\mathrm{S}}\int_{W_{\mathrm{M}}}^{\zeta} \mathcal{H}(d_l^{\mathrm{M}})\mathrm{d}d_l^{\mathrm{M}}\right] \\
&= \exp\left[-\pi\lambda_{\mathrm{S}}(\zeta - W_{\mathrm{M}})\int_{-1}^{1} \mathcal{H}\left(\frac{\zeta - W_{\mathrm{M}}}{2}v_{\mathrm{M}} + \frac{\zeta + W_{\mathrm{M}}}{2}\right)\mathrm{d}v_{\mathrm{M}}\right] \\
&= \exp\left\{\frac{-\pi^2\lambda_{\mathrm{S}}}{N}(\zeta - W_{\mathrm{M}})\sum_{o=1}^{O}\left[\mathcal{H}\left(\frac{\zeta - W_{\mathrm{M}}}{2}v_o^O + \frac{\zeta + W_{\mathrm{M}}}{2}\right)\sqrt{1 - (v_o^O)^2}\right]\right\},
\end{aligned} \tag{6.31}$$

where $u_c^C = \frac{2}{\zeta - x}\cos\left(\frac{2c-1}{2C}\pi\right) - \frac{\zeta + x}{\zeta - x}, c = 1, \dots, C$, and C is the sample size; $v_o^O = \frac{2}{\zeta - W_{\mathrm{M}}}\cos\left(\frac{2o-1}{2O}\pi\right) - \frac{\zeta + W_{\mathrm{M}}}{\zeta - W_{\mathrm{M}}}, o = 1, \dots, O$, and O is the sample size.

The approximation of $\mathcal{P}_{\mathrm{S}}$ can be derived following the same steps.

6.3.2 Cell-edge Average Coverage Probability

In this subsection, the average coverage probability for cell-edge users is investigated under special and practical scenarios. Assuming the horizontal distance between a cell-edge user and its associated BS is significantly greater than the BS antenna height, i.e. $d_i^M \gg h_{\mathrm{M}}$ and $d_j^S \gg h_{\mathrm{S}}$, the vertical pattern in (6.5) and (6.6) are asymptotic given by

$$G_i^{\mathrm{M}} = G_k^{\mathrm{M}} = G_k^{\mathrm{S}} \sim \max\left[-12\left(\frac{-\beta_{\mathrm{M}}}{\theta_{3\mathrm{dB}}}\right)^2, SLL_{\mathrm{M}}\right], \tag{6.32}$$

$$G_j^S = G_l^S = G_l^M \sim \max[10\log_{10}|\cos^{n_S}(-\beta_{\mathrm{S}})|, SLL_{\mathrm{S}}], \tag{6.33}$$

Considering a special case that applying unbiased association ($B_{\mathrm{S}} = 1$) and equal path loss components ($\alpha_{\mathrm{M}} = \alpha_{\mathrm{S}} = \alpha$), the cell-edge average coverage probability conditional on a typical cell-edge user associated with an MBS is given by

$$\begin{aligned}\mathcal{P}_{\mathrm{M}}(1,\alpha) &= \mathbb{E}_{d_i^{\mathrm{M}}}\left[\Pr\left(\mathrm{SIR}_i^{\mathrm{M}} > \tau\right)\right] \\ &= \int_{E_{\min}^{\mathrm{M}}}^{\infty} \left[\Pr\left(\mathrm{SIR}_i^{\mathrm{M}} > \tau\right)\right] f_{d_i^{\mathrm{M}}}(x)\mathrm{d}x \\ &= \int_{E_{\min}^{\mathrm{M}}}^{\infty} \mathcal{L}_{I_k^{\mathrm{M}}}\mathcal{L}_{I_{\mathrm{S}}^{\mathrm{M}}} f_{d_i^{\mathrm{M}}}(x)\mathrm{d}x,\end{aligned} \tag{6.34}$$

where $E_{\min}^{\mathrm{M}}$ denotes the minimum distance between a cell-edge user and its associated MBS;

$$\mathcal{L}_{I_k^{\mathrm{M}}} = \exp\left[-\frac{2\pi\lambda_{\mathrm{M}}}{s}\int_x^{\infty}\frac{d_k^{\mathrm{M}}}{1+\varepsilon_k^{\mathrm{M}}\frac{L_i^{\mathrm{M}}}{L_k^{\mathrm{M}}}}\mathrm{d}d_k^{\mathrm{M}}\right], \tag{6.35}$$

$$\mathcal{L}_{I_{\mathrm{S}}^{\mathrm{M}}} = \exp\left[-2\pi\lambda_{\mathrm{S}}\int_{W_{\mathrm{M}}}^{\infty}\frac{d_l^{\mathrm{M}}}{1+\varepsilon_{\mathrm{S}}^{\mathrm{M}}\frac{L_i^{\mathrm{M}}}{L_l^{\mathrm{M}}}}\mathrm{d}d_l^{\mathrm{M}}\right], \tag{6.36}$$

where $\varepsilon_k^{\mathrm{M}} = \frac{1}{\tau}$ and $\varepsilon_{\mathrm{S}}^{\mathrm{M}} = \frac{P_{\mathrm{M}}G_i^{\mathrm{M}}}{\tau P_{\mathrm{S}}G_l^{\mathrm{M}}}$. When $B_{\mathrm{S}} = 1$, according to (6.14) and (6.23), $f_{d_i^{\mathrm{M}}}(x) = \frac{2\pi\lambda_{\mathrm{M}}}{\mathcal{A}_{\mathrm{M}}} x e^{-\pi[x^2(\lambda_{\mathrm{M}}+\lambda_{\mathrm{S}})+\lambda_{\mathrm{S}}(h_{\mathrm{M}}^2-h_{\mathrm{S}}^2)]}$. Assuming $\alpha = 2$, $\mathcal{L}_{I_k^{\mathrm{M}}}$ and $\mathcal{L}_{I_{\mathrm{M}}^{\mathrm{S}}}$ can be further simplified as

$$\mathcal{L}_{I_k^{\mathrm{M}}} = \exp\left[-\frac{2\pi\lambda_{\mathrm{M}}}{s}\int_x^{\infty}\frac{d_k^{\mathrm{M}}}{1+\varepsilon_k^{\mathrm{M}}L_i^{\mathrm{M}}((d_k^{\mathrm{M}})^2+h_{\mathrm{M}}^2)}\mathrm{d}d_k^{\mathrm{M}}\right], \tag{6.37}$$

$$\mathcal{L}_{I_{\mathrm{S}}^{\mathrm{M}}} = \exp\left[-2\pi\lambda_{\mathrm{S}}\int_{W_{\mathrm{M}}}^{\infty}\frac{d_l^{\mathrm{M}}}{1+\varepsilon_{\mathrm{S}}^{\mathrm{M}}L_i^{\mathrm{M}}((d_k^{\mathrm{M}})^2+h_{\mathrm{S}}^2)}\mathrm{d}d_l^{\mathrm{M}}\right]. \tag{6.38}$$

According to (6.14) and (6.20), when $B_{\mathrm{S}} = 1$, $W_{\mathrm{M}} = \sqrt{x^2 + h_{\mathrm{M}}^2 - h_{\mathrm{S}}^2}$. Then the integral components of $\mathcal{L}_{I_k^{\mathrm{M}}}$ and $\mathcal{L}_{I_{\mathrm{S}}^{\mathrm{M}}}$ can be readily computed, after which $\mathcal{L}_{I_i^{\mathrm{M}}}$ and $\mathcal{L}_{I_{\mathrm{S}}^{\mathrm{M}}}$ are expressed as

$$\begin{aligned}\mathcal{L}_{I_k^{\mathrm{M}}} &= \exp\left[-\frac{\pi\lambda_{\mathrm{M}}}{s\varepsilon_i^{\mathrm{M}}(x^2+h_{\mathrm{M}}^2)}\ln\left[\frac{1+\varepsilon_k^{\mathrm{M}}(\zeta^2+h_{\mathrm{M}}^2)(x^2+h_{\mathrm{M}}^2)}{1+\varepsilon_k^{\mathrm{M}}(x^2+h_{\mathrm{M}}^2)^2}\right]\right] \\ &= \left(\frac{1+\varepsilon_k^{\mathrm{M}}(\zeta^2+h_{\mathrm{M}}^2)(x^2+h_{\mathrm{M}}^2)}{1+\varepsilon_k^{\mathrm{M}}(x^2+h_{\mathrm{M}}^2)^2}\right)^{-\frac{\pi\lambda_{\mathrm{M}}}{s\varepsilon_k^{\mathrm{M}}(x^2+h_{\mathrm{M}}^2)}},\end{aligned} \tag{6.39}$$

$$\begin{aligned}\mathcal{L}_{I_{\mathrm{S}}^{\mathrm{M}}} &= \exp\left[-\frac{\pi\lambda_{\mathrm{S}}}{\varepsilon_{\mathrm{S}}^{\mathrm{M}}(x^2+h_{\mathrm{M}}^2)}\ln\left[\frac{1+\varepsilon_{\mathrm{S}}^{\mathrm{M}}(\zeta^2+h_{\mathrm{S}}^2)(x^2+h_{\mathrm{M}}^2)}{1+\varepsilon_{\mathrm{S}}^{\mathrm{M}}(x^2+h_{\mathrm{M}}^2)^2}\right]\right] \\ &= \left(\frac{1+\varepsilon_{\mathrm{S}}^{\mathrm{M}}(\zeta^2+h_{\mathrm{S}}^2)(x^2+h_{\mathrm{M}}^2)}{1+\varepsilon_{\mathrm{S}}^{\mathrm{M}}(x^2+h_{\mathrm{M}}^2)^2}\right)^{-\frac{\pi\lambda_{\mathrm{S}}}{\varepsilon_{\mathrm{S}}^{\mathrm{M}}(x^2+h_{\mathrm{M}}^2)}}.\end{aligned} \tag{6.40}$$

It is obvious that $\varepsilon_k^{\mathrm{M}}(\zeta^2+h_{\mathrm{M}}^2)(x^2+h_{\mathrm{M}}^2)$, $\varepsilon_k^{\mathrm{M}}(x^2+h_{\mathrm{M}}^2)^2$, $\varepsilon_{\mathrm{S}}^{\mathrm{M}}(\zeta^2+h_{\mathrm{S}}^2)(x^2+h_{\mathrm{M}}^2)$, and $\varepsilon_{\mathrm{S}}^{\mathrm{M}}(x^2+h_{\mathrm{M}}^2)^2$ are all significantly greater than 1. According to the Cauchy-Schwarz inequality [196] and the Chebyshev's inequality [197], (6.34) is lower bounded by

$$\begin{aligned}\mathcal{P}_{\mathrm{M}}(1,2) \geq \frac{1}{(\zeta-E_{\min}^{\mathrm{M}})^2}&\int_{E_{\min}^{\mathrm{M}}}^{\zeta}\left(\frac{\zeta^2+h_{\mathrm{M}}^2}{x^2+h_{\mathrm{M}}^2}\right)^{-\frac{\pi\lambda_{\mathrm{M}}}{s\varepsilon_k^{\mathrm{M}}(x^2+h_{\mathrm{M}}^2)}}\mathrm{d}x \\ &\times\int_{E_{\min}^{\mathrm{M}}}^{\zeta}\left(\frac{\zeta^2+h_{\mathrm{S}}^2}{x^2+h_{\mathrm{M}}^2}\right)^{-\frac{\pi\lambda_{\mathrm{S}}}{\varepsilon_{\mathrm{S}}^{\mathrm{M}}(x^2+h_{\mathrm{M}}^2)}}\mathrm{d}x\int_{E_{\min}^{\mathrm{M}}}^{\zeta}f_{d_i^{\mathrm{M}}}(x)\mathrm{d}x,\end{aligned} \tag{6.41}$$

In this expression, the double integral in (6.41) is reduced to 3 single integrals, with the resulting integrand being straightforward to compute.

Similarly, the cell-edge average coverage probability conditional on a typical cell-edge user associated with an SBS is lower bounded by

$$\begin{aligned}\mathcal{P}_{\mathrm{S}}(1,2) \geq & \frac{1}{\left(-E_{\min}^{\mathrm{S}}\right)^2} \int_{E_{\min}^{\mathrm{S}}}^{\zeta} \left(\frac{\zeta^2 + h_{\mathrm{S}}^2}{x^2 + h_{\mathrm{S}}^2}\right)^{-\frac{\pi\lambda_{\mathrm{S}}}{\varepsilon_l^{\mathrm{S}}(x^2+h_{\mathrm{S}}^2)}} \mathrm{d}y \\ & \times \int_{E_{\min}^{\mathrm{S}}}^{\zeta} \left(\frac{\zeta^2 + h_{\mathrm{M}}^2}{x^2 + h_{\mathrm{S}}^2}\right)^{-\frac{\pi\lambda_{\mathrm{M}}}{s\varepsilon_{\mathrm{M}}^{\mathrm{S}}(x^2+h_{\mathrm{S}}^2)}} \mathrm{d}y \int_{E_{\min}^{\mathrm{S}}}^{\zeta} f_{d_j^{\mathrm{S}}}(y)\mathrm{d}y,\end{aligned} \tag{6.42}$$

where $\varepsilon_l^{\mathrm{S}} = \frac{1}{\tau}$, $\varepsilon_{\mathrm{M}}^{\mathrm{S}} = \frac{P_{\mathrm{S}}G_j^{\mathrm{S}}}{\tau P_{\mathrm{M}}G_k^{\mathrm{S}}}$, and $f_{d_j^{\mathrm{S}}}(y) = \frac{2\pi\lambda_{\mathrm{S}}}{\mathcal{A}_{\mathrm{S}}} y e^{-\pi\left[y^2(\lambda_{\mathrm{S}}+\lambda_{\mathrm{M}})+\lambda_{\mathrm{M}}\left(h_{\mathrm{S}}^2-h_{\mathrm{M}}^2\right)\right]}$.

Considering a practical HTCN with reasonable parameter values, it can be verified that $\mathcal{L}_{I_k^{\mathrm{M}}}$, $\mathcal{L}_{I_{\mathrm{S}}^{\mathrm{M}}}$, $\mathcal{L}_{I_l^{\mathrm{S}}}$, and $\mathcal{L}_{I_{\mathrm{M}}^{\mathrm{S}}}$ are always extremely close to 1. Consequently, (6.34) and (6.42) can be further simplified as

$$\begin{aligned}\mathcal{P}_{\mathrm{M}}(1,2) &\approx \int_{E_{\min}^{\mathrm{M}}}^{\zeta} f_{d_i^{\mathrm{M}}}(x)\mathrm{d}x \\ &= \int_{E_{\min}^{\mathrm{M}}}^{\infty} \frac{2\pi\lambda_{\mathrm{M}}}{\mathcal{A}_{\mathrm{M}}} x e^{-\pi\left[x^2(\lambda_{\mathrm{M}}+\lambda_{\mathrm{S}})+\lambda_{\mathrm{S}}\left(h_{\mathrm{M}}^2-h_{\mathrm{S}}^2\right)\right]}\mathrm{d}x \\ &= \frac{\lambda_{\mathrm{M}}}{\mathcal{A}_{\mathrm{M}}(\lambda_{\mathrm{M}}+\lambda_{\mathrm{S}})}\begin{bmatrix} e^{-\pi\left[\zeta^2(\lambda_{\mathrm{M}}+\lambda_{\mathrm{S}})+\lambda_{\mathrm{S}}\left(h_{\mathrm{M}}^2-h_{\mathrm{S}}^2\right)\right]} \\ -e^{-\pi\left[\left(E_{\min}^{\mathrm{M}}\right)^2(\lambda_{\mathrm{M}}+\lambda_{\mathrm{S}})+\lambda_{\mathrm{S}}\left(h_{\mathrm{M}}^2-h_{\mathrm{S}}^2\right)\right]}\end{bmatrix},\end{aligned} \tag{6.43}$$

$$\begin{aligned}\mathcal{P}_{\mathrm{S}}(1,2) &\approx \int_{E_{\min}^{\mathrm{S}}}^{\zeta} f_{d_j^{\mathrm{S}}}(y)\mathrm{d}y \\ &= \int_{E_{\min}^{\mathrm{S}}}^{\zeta} \frac{2\pi\lambda_{\mathrm{S}}}{\mathcal{A}_{\mathrm{S}}} y e^{-\pi\left[y^2(\lambda_{\mathrm{S}}+\lambda_{\mathrm{M}})+\lambda_{\mathrm{M}}\left(h_{\mathrm{S}}^2-h_{\mathrm{M}}^2\right)\right]}\mathrm{d}y \\ &= \frac{\lambda_{\mathrm{S}}}{\mathcal{A}_{\mathrm{S}}(\lambda_{\mathrm{S}}+\lambda_{\mathrm{M}})}\begin{bmatrix} e^{-\pi\left[\zeta^2(\lambda_{\mathrm{S}}+\lambda_{\mathrm{M}})+\lambda_{\mathrm{M}}\left(h_{\mathrm{S}}^2-h_{\mathrm{M}}^2\right)\right]} \\ -e^{-\pi\left[\left(E_{\min}^{\mathrm{S}}\right)^2(\lambda_{\mathrm{S}}+\lambda_{\mathrm{M}})+\lambda_{\mathrm{M}}\left(h_{\mathrm{S}}^2-h_{\mathrm{M}}^2\right)\right]}\end{bmatrix}.\end{aligned} \tag{6.44}$$

These expressions are especially simple and fully in closed form. In particular, the cell-edge average coverage probability for each tier is now independent of the BS antenna gain and BS transmit power under unbiased association. This indicates that adjusting BS antenna downtilts and BS transmit power has no impact on cell-edge users, since the desired signal and interference offset each other at the cell edge in a practical HTCN. The average coverage probability of cell-edge users is primarily affected by BS densities and BS heights.

6.3.3 Area Spectral Efficiency

The ASE evaluates the SE of the two-tier HTCN per unit area [198] (in bps/Hz/km^2) and is given by [199]

$$ASE = (\lambda_{\mathrm{M}}\mathcal{P}_{\mathrm{M}}\mathcal{A}_{\mathrm{M}} + \lambda_{\mathrm{S}}\mathcal{P}_{\mathrm{S}}\mathcal{A}_{\mathrm{S}}) \log_2(1+\tau). \tag{6.45}$$

6.3.4 Energy Efficiency

The EE can be quantified by inverting the Energy Consumption Rating and is expressed as [143]

$$EE = \frac{ASE}{\lambda_{\mathrm{M}} P_{\mathrm{M}}^{\mathrm{T}} + \lambda_{\mathrm{S}} P_{\mathrm{S}}^{\mathrm{T}}}, \tag{6.46}$$

where $P_{\mathrm{M}}^{\mathrm{T}}$ and $P_{\mathrm{S}}^{\mathrm{T}}$ denote the total power consumed by an MBS and an SBS, respectively, and can be calculated according to models in [200]–[202] by

$$P_{\mathrm{M}}^{\mathrm{T}} = s(\kappa_{\mathrm{M}a} P_{\mathrm{M}} + P_{\mathrm{M}c}), \tag{6.47}$$

$$P_{\mathrm{S}}^{\mathrm{T}} = \kappa_{\mathrm{S}a} P_{\mathrm{S}} + P_{\mathrm{S}c}, \tag{6.48}$$

where $\kappa_{\mathrm{M}a}$ and $\kappa_{\mathrm{S}a}$ present the load-dependent transmit power consumption of the power amplifier, feed losses, and cooling in the macro-cell tier and small-cell tier, respectively; $P_{\mathrm{M}c}$ and $P_{\mathrm{S}c}$ are the independent transmit power consumption related to signal processing, battery backup, and cooling unit components.

6.4 Optimization of the MBS and SBS Antenna Downtilt Pair

In this section, the MBS and SBS antenna downtilt pair optimization problem is formulated and solved.

6.4.1 Problem Formulation and Solution

The spatially-averaged coverage probability is maximized by optimizing the electrical downtilts of antennas at MBSs and SBSs, i.e., β_{M} and β_{S}. The optimization problem is formulated as

$$\begin{aligned} \max_{\beta_{\mathrm{M}},\beta_{\mathrm{S}}} \quad & p_{\mathrm{c}} \\ \text{s.t.} \quad & 0 \leq \beta_{\mathrm{M}} \leq \frac{\pi}{2}, \\ & 0 \leq \beta_{\mathrm{S}} \leq \frac{\pi}{2}. \end{aligned} \tag{6.49}$$

This problem can be addressed by calculating the partial derivative of the spatially-averaged coverage probability with respect to the independent variable β_{M} and β_{S}, respectively [203]. The maximum point $(\beta_{\mathrm{M}}^*, \beta_{\mathrm{S}}^*)$ is one of the stationary points of $p_{\mathrm{c}}(\beta_{\mathrm{M}}, \beta_{\mathrm{S}})$ by working out $\frac{\partial p_{\mathrm{c}}}{\partial \beta_{\mathrm{M}}}$ and $\frac{\partial p_{\mathrm{c}}}{\partial \beta_{\mathrm{S}}}$, and setting both to zero. According to (6.9), variables β_{M} and β_{S} only have impact on $\mathcal{P}_{\mathrm{M}}$ and $\mathcal{P}_{\mathrm{S}}$. Therefore, the optimal BS antenna downtilt pair is obtained from following equations:

$$\begin{aligned} \{\beta_{\mathrm{M}}^*, \beta_{\mathrm{S}}^*\} = \Bigg\{ & \arg_{\beta_{\mathrm{M}}} \left\{ \mathcal{A}_{\mathrm{M}} \frac{\partial \mathcal{P}_{\mathrm{M}}}{\partial \beta_{\mathrm{M}}} + \mathcal{A}_{\mathrm{S}} \frac{\partial \mathcal{P}_{\mathrm{S}}}{\partial \beta_{\mathrm{M}}} = 0 \right\}, \\ & \arg_{\beta_{\mathrm{S}}} \left\{ \mathcal{A}_{\mathrm{M}} \frac{\partial \mathcal{P}_{\mathrm{M}}}{\partial \beta_{\mathrm{S}}} + \mathcal{A}_{\mathrm{S}} \frac{\partial \mathcal{P}_{\mathrm{S}}}{\partial \beta_{\mathrm{S}}} = 0 \right\} \Bigg\}, \end{aligned} \tag{6.50}$$

where

$$\begin{aligned} \frac{\partial \mathcal{P}_{\mathrm{M}}}{\partial \beta_{\mathrm{M}}} &= \int_0^\infty \left[\frac{\partial}{\partial \beta_{\mathrm{M}}} \mathcal{L}_{I_k^{\mathrm{M}}} \mathcal{L}_{I_{\mathrm{S}}^{\mathrm{M}}} \right] f_{d_i^{\mathrm{M}}}(x) \mathrm{d}x \\ &= \int_0^\infty \left[\mathcal{L}_{I_k^{\mathrm{M}}} \mathcal{L}_{I_{\mathrm{S}}^{\mathrm{M}}} \left(\mathcal{L}'_{I_k^{\mathrm{M}}|\beta_{\mathrm{M}}} + \mathcal{L}'_{I_{\mathrm{S}}^{\mathrm{M}}|\beta_{\mathrm{M}}} \right) \right] f_{d_i^{\mathrm{M}}}(x) \mathrm{d}x, \end{aligned} \tag{6.51}$$

$$\begin{aligned}\frac{\partial \mathcal{P}_{\mathrm{S}}}{\partial \beta_{\mathrm{M}}} &= \int_{0}^{\infty}\left[\frac{\partial}{\partial \beta_{\mathrm{M}}}\mathcal{L}_{I_l^{\mathrm{S}}}\mathcal{L}_{I_{\mathrm{M}}^{\mathrm{S}}}\right] f_{d_j^{\mathrm{S}}}(y)\mathrm{d}y \\ &= \int_{0}^{\infty}\left[\mathcal{L}_{I_l^{\mathrm{S}}}\mathcal{L}_{I_{\mathrm{M}}^{\mathrm{S}}}\mathcal{L}'_{I_{\mathrm{M}}^{\mathrm{S}}|\beta_{\mathrm{M}}}\right] f_{d_j^{\mathrm{S}}}(y)\mathrm{d}y,\end{aligned} \tag{6.52}$$

$$\begin{aligned}\frac{\partial \mathcal{P}_{\mathrm{M}}}{\partial \beta_{\mathrm{S}}} &= \int_{0}^{\infty}\left[\frac{\partial}{\partial \beta_{\mathrm{S}}}\mathcal{L}_{I_k^{\mathrm{M}}}\mathcal{L}_{I_{\mathrm{S}}^{\mathrm{M}}}\right] f_{d_i^{\mathrm{M}}}(x)\mathrm{d}x \\ &= \int_{0}^{\infty}\left[\mathcal{L}_{I_k^{\mathrm{M}}}\mathcal{L}_{I_{\mathrm{S}}^{\mathrm{M}}}\mathcal{L}'_{I_{\mathrm{S}}^{\mathrm{M}}|\beta_{\mathrm{S}}}\right] f_{d_i^{\mathrm{M}}}(x)\mathrm{d}x,\end{aligned} \tag{6.53}$$

$$\begin{aligned}\frac{\partial \mathcal{P}_{\mathrm{S}}}{\partial \beta_{\mathrm{S}}} &= \int_{0}^{\infty}\left[\frac{\partial}{\partial \beta_{\mathrm{S}}}\mathcal{L}_{I_l^{\mathrm{S}}}\mathcal{L}_{I_{\mathrm{M}}^{\mathrm{S}}}\right] f_{d_j^{\mathrm{S}}}(y)\mathrm{d}y \\ &= \int_{0}^{\infty}\left[\mathcal{L}_{I_l^{\mathrm{S}}}\mathcal{L}_{I_{\mathrm{M}}^{\mathrm{S}}}\left(\mathcal{L}'_{I_l^{\mathrm{S}}|\beta_{\mathrm{S}}}+\mathcal{L}'_{I_{\mathrm{M}}^{\mathrm{S}}|\beta_{\mathrm{S}}}\right)\right] f_{d_j^{\mathrm{S}}}(y)\mathrm{d}y,\end{aligned} \tag{6.54}$$

and

$$\mathcal{L}'_{I_k^{\mathrm{M}}|\beta_{\mathrm{M}}} = -\frac{2\pi\lambda_{\mathrm{M}}}{s}\int_{x}^{\infty}\left[d_k^{\mathrm{M}}\mathcal{K}_k^{\mathrm{M}}\frac{G_i^{\mathrm{M}}\frac{\partial G_k^{\mathrm{M}}}{\partial \beta_{\mathrm{M}}}-\frac{\partial G_i^{\mathrm{M}}}{\partial \beta_{\mathrm{M}}}G_k^{\mathrm{M}}}{(G_k^{\mathrm{M}}+\mathcal{K}_k^{\mathrm{M}}G_i^{\mathrm{M}})^2}\right]\mathrm{d}d_k^{\mathrm{M}}, \tag{6.55}$$

$$\mathcal{L}'_{I_{\mathrm{S}}^{\mathrm{M}}|\beta_{\mathrm{M}}} = -2\pi\lambda_{\mathrm{S}}\int_{W_{\mathrm{M}}}^{\infty}\left[-d_l^{\mathrm{M}}\mathcal{K}_{\mathrm{S}}^{\mathrm{M}}\frac{\frac{\partial G_i^{\mathrm{M}}}{\partial \beta_{\mathrm{M}}}}{G_l^{\mathrm{M}}\left(1+\mathcal{K}_{\mathrm{S}}^{\mathrm{M}}\frac{G_i^{\mathrm{M}}}{G_l^{\mathrm{M}}}\right)^2}\right]\mathrm{d}d_l^{\mathrm{M}}, \tag{6.56}$$

$$\mathcal{L}'_{I_{\mathrm{M}}^{\mathrm{S}}|\beta_{\mathrm{M}}} = -\frac{2\pi\lambda_{\mathrm{M}}}{s}\int_{W_{\mathrm{S}}}^{\infty}\left[d_k^{\mathrm{S}}\mathcal{K}_{\mathrm{M}}^{\mathrm{S}}G_j^{\mathrm{S}}\frac{\frac{\partial G_k^{\mathrm{S}}}{\partial \beta_{\mathrm{M}}}}{\left(G_k^{\mathrm{S}}+\mathcal{K}_{\mathrm{M}}^{\mathrm{S}}G_j^{\mathrm{S}}\right)^2}\right]\mathrm{d}d_k^{\mathrm{S}}, \tag{6.57}$$

$$\mathcal{L}'_{I_{\mathrm{S}}^{\mathrm{M}}|\beta_{\mathrm{S}}} = -2\pi\lambda_{\mathrm{S}} \int_{W_{\mathrm{M}}}^{\infty} \left[d_l^{\mathrm{M}} \mathcal{K}_{\mathrm{S}}^{\mathrm{M}} G_i^{\mathrm{M}} \frac{\frac{\partial G_l^{\mathrm{M}}}{\partial \beta_S}}{(G_l^{\mathrm{M}} + \mathcal{K}_{\mathrm{S}}^{\mathrm{M}} G_i^{\mathrm{M}})^2} \right] \mathrm{d}d_l^{\mathrm{M}}, \tag{6.58}$$

$$\mathcal{L}'_{I_l^{\mathrm{S}}|\beta_{\mathrm{S}}} = -2\pi\lambda_{\mathrm{S}} \int_{y}^{\infty} \left[d_l^{\mathrm{S}} \mathcal{K}_l^{\mathrm{S}} \frac{G_j^{\mathrm{S}} \frac{\partial G_l^{\mathrm{S}}}{\partial \beta_{\mathrm{S}}} - \frac{\partial G_j^{\mathrm{S}}}{\partial \beta_{\mathrm{S}}} G_l^{\mathrm{S}}}{\left(G_l^{\mathrm{S}} + \mathcal{K}_l^{\mathrm{S}} G_j^{\mathrm{S}}\right)^2} \right] \mathrm{d}d_l^{\mathrm{S}}, \tag{6.59}$$

$$\mathcal{L}'_{I_{\mathrm{M}}^{\mathrm{S}}|\beta_{\mathrm{S}}} = -\frac{2\pi\lambda_{\mathrm{M}}}{s} \int_{W_{\mathrm{S}}}^{\infty} \left[-d_k^{\mathrm{S}} \mathcal{K}_{\mathrm{M}}^{\mathrm{S}} \frac{\frac{\partial G_j^{\mathrm{S}}}{\partial \beta_{\mathrm{S}}}}{G_k^{\mathrm{S}} \left(1 + \mathcal{K}_{\mathrm{M}}^{\mathrm{S}} \frac{G_j^{\mathrm{S}}}{G_k^{\mathrm{S}}}\right)^2} \right] \mathrm{d}d_k^{\mathrm{S}}. \tag{6.60}$$

Since β_{S} is in the range of $\left[0, \frac{\pi}{2}\right]$, $\cos^{n_{\mathrm{S}}}\left(\beta_{\mathrm{S}} - \theta_j^{\mathrm{S}}\right)$ in (6.6) is always non-negative. The derivative of the antenna main lobe pattern with respect to β_{M} and β_{S} from MBS i and SBS j are computed as

$$\frac{\partial G_i^{\mathrm{M}}}{\partial \beta_{\mathrm{M}}} = \frac{2.4 \log\ 10 G_{\mathrm{M_m}}}{\theta_{3\mathrm{dB}}^2} 10^{-1.2\left(\frac{\theta_i^{\mathrm{M}} - \beta_{\mathrm{M}}}{\theta_{3\mathrm{dB}}}\right)^2} \left(\theta_i^{\mathrm{M}} - \beta_{\mathrm{M}}\right), \tag{6.61}$$

$$\frac{\partial G_j^{\mathrm{S}}}{\partial \beta_{\mathrm{S}}} = n_{\mathrm{S}} G_{\mathrm{S_m}} \cos^{n_{\mathrm{S}}-1}\left(\theta_j^{S} - \beta_{\mathrm{S}}\right) \sin\left(\theta_j^{S} - \beta_{\mathrm{S}}\right). \tag{6.62}$$

In order to verify the uniqueness of the stationary point which is derived from differential equations in (6.50), each equation is solved individually while keeping the invariable downtilt constant in the range of $\left[0, \frac{\pi}{2}\right]$. The complexity of calculation in (6.50) is reduced by a bisection method, which is shown in Algorithm 6.1 as follows:

Algorithm 6.1: Bisection Method.	
1:	Initialize $\beta_\mu^{\text{lower}} = \beta_\mu^{\min}$ and $\beta_\mu^{\text{upper}} = \beta_\mu^{\max}$.
	Calculate $p'_{\mathrm{c}'_{\min}} = \mathcal{A}_{\mathrm{M}} \frac{\partial \mathcal{P}_\mu(\beta_\mu^{\min})'}{\partial \beta_\mu^{\min}} + \mathcal{A}_{\mathrm{S}} \frac{\partial \mathcal{P}_{\mu'}(\beta_\mu^{\min})}{\partial \beta_\mu^{\min}}$.
2:	Calculate p'_{c} for $\beta_\mu = \frac{\beta_\mu^{\text{lower}} + \beta_\mu^{\text{upper}}}{2}$.
3:	If $p'_{\mathrm{c}_{\min}} p'_{\mathrm{c}} > 0$, then set $\beta_\mu^{\text{lower}} = \beta_\mu, p'_{\mathrm{c}_{\min}} = p'_{\mathrm{c}}$.
	Otherwise, set $\beta_\mu^{\text{upper}} = \beta_\mu$.
4:	Stop when $\left|\beta_\mu^{\text{upper}} - \beta_\mu^{\text{lower}}\right|$ is less than a predefined value.

Where $\mu, \mu' \in \{\mathrm{M}, \mathrm{S}\}$ indicates whether the serving BS is an MBS or an SBS. If $\mu = \mathrm{M}, \mu' = \mathrm{S}$; if $\mu = \mathrm{S}, \mu' = \mathrm{M}$. The range of the optimal MBS antenna downtilt and the optimal SBS antenna downtilt are restricted as $\beta_{\mathrm{M}}^* \in [\beta_{\mathrm{M}}^{\min}, \beta_{\mathrm{M}}^{\max}]$ and $\beta_S^* \in [\beta_{\mathrm{S}}^{\min}, \beta_{\mathrm{S}}^{\max}]$, respectively. According to (6.5) and (6.6), the bounds of β_μ are calculated as

$$-12\left(\frac{\tan^{-1}\left(\frac{h_{\mathrm{M}}}{x}\right) - \beta_{\mathrm{M}}}{\theta_{3\mathrm{dB}}}\right)^2 \geq SLL_{\mathrm{M}}, \tag{6.63}$$

$$10\log_{10}\left|\cos^{n_{\mathrm{S}}}\left(\tan^{-1}\left(\frac{h_{\mathrm{S}}}{y}\right) - \beta_{\mathrm{S}}\right)\right| \geq SLL_{\mathrm{S}}. \tag{6.64}$$

By combining these bounds with (6.49), the following expressions are obtained:

$$\begin{aligned} \beta_{\mathrm{M}}^{\min} &= \max\left[\tan^{-1}\left(\frac{h_{\mathrm{M}}}{x_{\max}}\right) - \theta_{3\mathrm{dB}}\sqrt{\frac{SLL_{\mathrm{M}}}{12}}, 0\right], \\ \beta_{\mathrm{M}}^{\max} &= \min\left[\tan^{-1}\left(\frac{h_{\mathrm{M}}}{x_{\min}}\right) + \theta_{3\mathrm{dB}}\sqrt{\frac{SLL_{\mathrm{M}}}{12}}, \frac{\pi}{2}\right], \end{aligned} \tag{6.65}$$

$$\begin{aligned} \beta_{\mathrm{S}}^{\min} &= \max\left[\tan^{-1}\left(\frac{h_{\mathrm{S}}}{y_{\max}}\right) - \cos^{-1}\left(\sqrt[n_{\mathrm{S}}]{SLL_{\mathrm{S}}}\right), 0\right], \\ \beta_{\mathrm{S}}^{\max} &= \min\left[\tan^{-1}\left(\frac{h_{\mathrm{S}}}{y_{\min}}\right) + \cos^{-1}\left(\sqrt[n_{\mathrm{S}}]{SLL_{\mathrm{S}}}\right), \frac{\pi}{2}\right], \end{aligned} \tag{6.66}$$

where $x_{\min}$ and $x_{\max}$ ($y_{\min}$ and $y_{\max}$) are constraints of the horizontal distance from a typical MBS (SBS) user to its serving BS. According to (6.23) and (6.28), for a given probability σ, the constraints of the distance are obtained by $\Pr\left(x_{\min} \leq x \leq x_{\max}\right) = f_{d_i^{\mathrm{M}}}(x) \geq \sigma$ and $\Pr\left(y_{\min} \leq y \leq y_{\max}\right) = f_{d_j^{\mathrm{S}}}(y) \geq \sigma$.

Define T represents the total number of iterations for obtaining β_μ^*, the computational complexity of Algorithm 6.1 is $\mathcal{O}(T)$.

6.4.2 Verification of the Optimal Point

To prove that the stationary point is a local maximum point, the second derivative test is employed to classify the type of this point [204]. The second derivative of p_c with respect to β_{M} and β_{S} are derived from (6.51), (6.52), (6.53), and (6.54) as

$$\begin{aligned}
\frac{\partial^2 p_{\mathrm{c}}}{\partial \beta_{\mathrm{M}}^2} &= \mathcal{A}_{\mathrm{M}} \frac{\partial^2 \mathcal{P}_{\mathrm{M}}}{\partial \beta_{\mathrm{M}}^2} + \mathcal{A}_{\mathrm{S}} \frac{\partial^2 \mathcal{P}_{\mathrm{S}}}{\partial \beta_{\mathrm{M}}^2} \\
&= \int_0^\infty \left[\frac{\partial^2}{\partial \beta_{\mathrm{M}}^2} \mathcal{L}_{I_k^{\mathrm{M}}} \mathcal{L}_{I_{\mathrm{S}}^{\mathrm{M}}}\right] f_{d_i^{\mathrm{M}}}(x)\mathrm{d}x + \int_0^\infty \left[\frac{\partial^2}{\partial \beta_{\mathrm{M}}^2} \mathcal{L}_{I_l^{\mathrm{S}}} \mathcal{L}_{I_{\mathrm{M}}^{\mathrm{S}}}\right] f_{d_j^{\mathrm{S}}}(y)\mathrm{d}y \\
&= \int_0^\infty \left[\mathcal{L}_{I_k^{\mathrm{M}}} \mathcal{L}_{I_{\mathrm{S}}^{\mathrm{M}}} \left[\left(\mathcal{L}'_{I_k^{\mathrm{M}}|\beta_{\mathrm{M}}} + \mathcal{L}'_{I_{\mathrm{S}}^{\mathrm{M}}|\beta_{\mathrm{M}}}\right)^2 + \left(\mathcal{L}''_{I_k^{\mathrm{M}}|\beta_{\mathrm{M}}} + \mathcal{L}''_{I_{\mathrm{S}}^{\mathrm{M}}|\beta_{\mathrm{M}}}\right)\right]\right] f_{d_i^{\mathrm{M}}}(x)\mathrm{d}x \\
&\quad + \int_0^\infty \left[\mathcal{L}_{I_l^{\mathrm{S}}} \mathcal{L}_{I_{\mathrm{M}}^{\mathrm{S}}} \left[\left(\mathcal{L}'_{I_{\mathrm{M}}^{\mathrm{S}}|\beta_{\mathrm{M}}}\right)^2 + \mathcal{L}''_{I_{\mathrm{M}}^{\mathrm{S}}|\beta_{\mathrm{M}}}\right]\right] f_{d_j^{\mathrm{S}}}(y)\mathrm{d}y,
\end{aligned} \tag{6.67}$$

$$\begin{aligned}
\frac{\partial^2 p_c}{\partial \beta_{\mathrm{S}}^2} &= \mathcal{A}_{\mathrm{M}} \frac{\partial^2 \mathcal{P}_{\mathrm{M}}}{\partial \beta_{\mathrm{S}}^2} + \mathcal{A}_S \frac{\partial^2 \mathcal{P}_{\mathrm{S}}}{\partial \beta_{\mathrm{S}}^2} \\
&= \int_0^\infty \left[\frac{\partial^2}{\partial \beta_{\mathrm{S}}^2} \mathcal{L}_{I_k^{\mathrm{M}}} \mathcal{L}_{I_{\mathrm{S}}^{\mathrm{M}}} \right] f_{d_i^{\mathrm{M}}}(x) \mathrm{d}x + \int_0^\infty \left[\frac{\partial^2}{\partial \beta_{\mathrm{S}}^2} \mathcal{L}_{I_l^{\mathrm{S}}} \mathcal{L}_{I_{\mathrm{M}}^{\mathrm{S}}} \right] f_{d_j^{\mathrm{S}}}(y) \mathrm{d}y \\
&= \int_0^\infty \left[\mathcal{L}_{I_k^{\mathrm{M}}} \mathcal{L}_{I_{\mathrm{S}}^{\mathrm{M}}} \left[\left(\mathcal{L}'_{I_{\mathrm{S}}^{\mathrm{M}}|\beta_{\mathrm{S}}} + \mathcal{L}''_{I_{\mathrm{S}}^{\mathrm{M}}|\beta_{\mathrm{S}}} \right)^2 \right] \right] f_{d_i^M}(x) \mathrm{d}x \\
&+ \int_0^\infty \left[\mathcal{L}_{I_l^{\mathrm{S}}} \mathcal{L}_{I_{\mathrm{M}}^{\mathrm{S}}} \left[\left(\mathcal{L}'_{I_l^{\mathrm{S}}|\beta_{\mathrm{S}}} + \mathcal{L}'_{I_{\mathrm{M}}^{\mathrm{S}}|\beta_{\mathrm{S}}} \right)^2 + \left(\mathcal{L}''_{I_l^{\mathrm{S}}|\beta_{\mathrm{S}}} + \mathcal{L}''_{I_{\mathrm{M}}^{\mathrm{S}}|\beta_{\mathrm{S}}} \right) \right] \right] f_{d_j^{\mathrm{S}}}(y) \mathrm{d}y,
\end{aligned} \tag{6.68}$$

where

$$\begin{aligned}
&\mathcal{L}''_{I_k^{\mathrm{M}}|\beta_{\mathrm{M}}} \\
&= -\frac{2\pi\lambda_{\mathrm{M}}}{s} \int_x^\infty d_k^{\mathrm{M}} \mathcal{K}_k^{\mathrm{M}} \left[\frac{\left(G_i^{\mathrm{M}} \frac{\partial^2 G_k^{\mathrm{M}}}{\partial \beta_{\mathrm{M}}^2} - G_k^{\mathrm{M}} \frac{\partial^2 G_i^{\mathrm{M}}}{\partial \beta_{\mathrm{M}}^2} \right) \left(G_k^{\mathrm{M}} + \mathcal{K}_k^{\mathrm{M}} G_i^{\mathrm{M}} \right)}{(G_k^{\mathrm{M}} + \mathcal{K}_k^{\mathrm{M}} G_i^{\mathrm{M}})^3} \right. \\
&\left. - \frac{2 \left(\frac{\partial G_k^{\mathrm{M}}}{\partial \beta_{\mathrm{M}}} + \mathcal{K}_k^{\mathrm{M}} \frac{\partial G_i^{\mathrm{M}}}{\partial \beta_{\mathrm{M}}} \right) \left(G_i^{\mathrm{M}} \frac{\partial G_k^{\mathrm{M}}}{\partial \beta_{\mathrm{M}}} - G_k^{\mathrm{M}} \frac{\partial G_i^{\mathrm{M}}}{\partial \beta_{\mathrm{M}}} \right)}{(G_k^{\mathrm{M}} + \mathcal{K}_k^{\mathrm{M}} G_i^{\mathrm{M}})^3} \right] \mathrm{d}d_k^{\mathrm{M}},
\end{aligned} \tag{6.69}$$

$$\begin{aligned}
&\mathcal{L}''_{I_{\mathrm{S}}^{\mathrm{M}}|\beta_{\mathrm{M}}} \\
&= -2\pi\lambda_{\mathrm{S}} \int_{W_{\mathrm{M}}}^\infty -d_l^{\mathrm{M}} \mathcal{K}_{\mathrm{S}}^{\mathrm{M}} \frac{\frac{\partial^2 G_i^{\mathrm{M}}}{\partial \beta_{\mathrm{M}}^2} \left(1 + \mathcal{K}_{\mathrm{S}}^{\mathrm{M}} \frac{G_i^{\mathrm{M}}}{G_l^{\mathrm{M}}} \right) - \frac{2\mathcal{K}_{\mathrm{S}}^{\mathrm{M}}}{G_l^{\mathrm{M}}} \left(\frac{\partial G_i^{\mathrm{M}}}{\partial \beta_{\mathrm{M}}} \right)^2}{G_l^{\mathrm{M}} \left(1 + \mathcal{K}_{\mathrm{S}}^{\mathrm{M}} \frac{G_i^{\mathrm{M}}}{G_l^{\mathrm{M}}} \right)^3} \mathrm{d}d_k^{\mathrm{S}},
\end{aligned} \tag{6.70}$$

$$\begin{aligned}
&\mathcal{L}''_{I_{\mathrm{M}}^{\mathrm{S}}|\beta_{\mathrm{M}}} \\
&= -\frac{2\pi\lambda_{\mathrm{M}}}{s} \int_{W_{\mathrm{S}}}^\infty d_k^{\mathrm{S}} \mathcal{K}_{\mathrm{M}}^{\mathrm{S}} G_j^{\mathrm{S}} \frac{\frac{\partial^2 G_k^{\mathrm{S}}}{\partial \beta_{\mathrm{M}}^2} \left(G_k^{\mathrm{S}} + \mathcal{K}_{\mathrm{M}}^{\mathrm{S}} G_j^{\mathrm{S}} \right) - 2 \left(\frac{\partial G_k^{\mathrm{S}}}{\partial \beta_M} \right)^2}{\left(G_k^{\mathrm{S}} + \mathcal{K}_{\mathrm{M}}^{\mathrm{S}} G_j^{\mathrm{S}} \right)^3} \mathrm{d}d_k^{\mathrm{S}},
\end{aligned} \tag{6.71}$$

$$\mathcal{L}''_{I_{\mathrm{S}}^{\mathrm{M}}|\beta_{\mathrm{S}}} = -2\pi\lambda_{\mathrm{S}}\int_{W_{\mathrm{M}}}^{\infty} d_l^{\mathrm{M}}\mathcal{K}_{\mathrm{S}}^{\mathrm{M}}G_i^{\mathrm{M}}\frac{\frac{\partial^2 G_l^{\mathrm{M}}}{\partial\beta_{\mathrm{S}}^2}\left(G_l^{\mathrm{M}}+\mathcal{K}_{\mathrm{S}}^{\mathrm{M}}G_i^{\mathrm{M}}\right)-2\left(\frac{\partial G_l^{\mathrm{M}}}{\partial\beta_{\mathrm{S}}}\right)^2}{(G_l^{\mathrm{M}}+\mathcal{K}_{\mathrm{S}}^{\mathrm{M}}G_i^{\mathrm{M}})^3}\mathrm{d}d_l^{\mathrm{M}}, \tag{6.72}$$

$$\mathcal{L}''_{I_l^{\mathrm{S}}|\beta_{\mathrm{S}}} = -2\pi\lambda_{\mathrm{S}}\int_{y}^{\infty} d_l^{\mathrm{S}}\mathcal{K}_l^{\mathrm{S}}\left[\frac{\left(G_j^{\mathrm{S}}\frac{\partial^2 G_l^{\mathrm{S}}}{\partial\beta_{\mathrm{S}}^2}-G_l^{\mathrm{S}}\frac{\partial^2 G_j^{\mathrm{S}}}{\partial\beta_{\mathrm{S}}^2}\right)\left(G_l^{\mathrm{S}}+\mathcal{K}_l^{\mathrm{S}}G_j^{\mathrm{S}}\right)}{\left(G_l^{\mathrm{S}}+\mathcal{K}_l^{\mathrm{S}}G_j^{\mathrm{S}}\right)^3} - \frac{2\left(\frac{\partial G_l^{\mathrm{S}}}{\partial\beta_{\mathrm{S}}}+\mathcal{K}_l^{\mathrm{S}}\frac{\partial G_j^{\mathrm{S}}}{\partial\beta_{\mathrm{S}}}\right)\left(G_j^{\mathrm{S}}\frac{\partial G_l^{\mathrm{S}}}{\partial\beta_{\mathrm{S}}}-G_l^{\mathrm{S}}\frac{\partial G_j^{\mathrm{S}}}{\partial\beta_{\mathrm{S}}}\right)}{\left(G_l^{\mathrm{S}}+\mathcal{K}_l^{\mathrm{S}}G_j^{\mathrm{S}}\right)^3}\right]\mathrm{d}d_l^{\mathrm{S}}, \tag{6.73}$$

$$\mathcal{L}''_{I_{\mathrm{M}}^{\mathrm{S}}|\beta_{\mathrm{S}}} = -\frac{2\pi\lambda_{\mathrm{M}}}{s}\int_{W_{\mathrm{S}}}^{\infty} -d_k^{\mathrm{S}}\mathcal{K}_{\mathrm{M}}^{\mathrm{S}}\frac{\frac{\partial^2 G_j^{\mathrm{S}}}{\partial\beta_{\mathrm{S}}^2}\left(1+\mathcal{K}_{\mathrm{M}}^{\mathrm{S}}\frac{G_j^{\mathrm{S}}}{G_k^{\mathrm{S}}}\right)-\frac{2\mathcal{K}_{\mathrm{M}}^{\mathrm{S}}}{G_k^{\mathrm{S}}}\left(\frac{\partial G_j^{\mathrm{S}}}{\partial\beta_{\mathrm{S}}}\right)^2}{G_k^{\mathrm{S}}\left(1+\mathcal{K}_{\mathrm{M}}^{\mathrm{S}}\frac{G_j^{\mathrm{S}}}{G_k^{\mathrm{S}}}\right)^3}\mathrm{d}d_l^{\mathrm{M}}. \tag{6.74}$$

From (6.61) and (6.62), the second derivative of the antenna main lobe pattern with respect to β_{M} and β_{S} from MBS i and SBS j are

$$\frac{\partial^2 G_i^{\mathrm{M}}}{\partial\beta_{\mathrm{M}}^2} = \frac{2.4\log\ 10G_{\mathrm{M_m}}}{\theta_{3\mathrm{dB}}^2}10^{-1.2\left(\frac{\theta_i^{\mathrm{M}}-\beta_{\mathrm{M}}}{\theta_{3\mathrm{dB}}}\right)^2}\left[\left(\frac{\theta_i^{\mathrm{M}}-\beta_{\mathrm{M}}}{\theta_{3\mathrm{dB}}}\right)^2-1\right], \tag{6.75}$$

$$\frac{\partial^2 G_j^{\mathrm{S}}}{\partial\beta_{\mathrm{S}}^2} = n_{\mathrm{S}}G_{\mathrm{S_m}}\cos^{n_{\mathrm{S}}}\left(\theta_j^S-\beta_{\mathrm{S}}\right)\left[(n_{\mathrm{S}}-1)\tan^2\left(\theta_j^S-\beta_{\mathrm{S}}\right)-1\right]. \tag{6.76}$$

If $\frac{\partial^2 p_{\mathrm{c}}}{\partial\beta_\mu^2} < 0$, then the stationary point is a local maximum point; if $\frac{\partial^2 p_{\mathrm{c}}}{\partial\beta_\mu^2} > 0$, then the stationary point is a local minimum point; if $\frac{\partial^2 p_{\mathrm{c}}}{\partial\beta_\mu^2} = 0$, then the stationary point can be any type and determined by gradients at both sides of it.

6.5 Numerical Results

In this section, the results of the analytical expressions are presented to evaluate the performance of the proposed 3D two-tier HTCNs, and investigate the impact of BS antenna downtilts. The maximum spatially-averaged coverage probability, ASE, and EE are obtained with the optimal MBS antenna downtilt and SBS antenna downtilt.

6.5.1 Validation of System Model Analysis

Table 6.1 Simulation Settings

	Parameter	**Value**
Basic Simulation Parameters	Density of MBSs, λ_{M}	10 BS/km^2
	Density of SBSs, λ_{M}	2×10^2 BS/km^2
	Transmit power of MBSs, P_{M}	48 dBm
	Transmit power of SBSs, P_{S}	33 dBm
	Height of MBS, H_{M}	20 m
	Height of SBSs, H_{S}	6 m
	Height of users, H_{U}	1 m
	Path loss exponent of macro-cell tier, α_{M}	3.8
	Path loss exponent of small-cell tier, α_{S}	4
	Coverage probability threshold, τ	0 dB
	Number of macro-cell sectors, s	3
MBS Antenna Parameters	Vertical HPBW of MBS, $\theta_{3\mathrm{dB}}$	$\frac{\pi}{6}$ rad
	Vertical sidelobe level of MBSs, SLL_{M}	-20 dB
	Maximum antenna gain of MBSs, $G_{\mathrm{M_m}}$	18 dBi
SBS Antenna Parameters	number of elements	4
	n_{S}	47.64
	Vertical sidelobe level of SBSs, SLL_{S}	-12 dB
	Maximum antenna gain of SBSs, $G_{\mathrm{S_m}}$	8.15 dBi

Firstly, results of the spatially-averaged coverage probability for different numbers of SBS antenna elements from numerical analysis and Monte Carlo simulations are compared to validate the accuracy of deductions and approximation methods. Each Monte Carlo simulation is performed with 2×10^4 independent random realizations. In each realization, assuming that a typical user is located at the origin on a 2D ground plane, an HTCN is simulated following the system model defined in Section 6.2 in a circular region centered at the origin with a radius of 3000 m. Unless otherwise specified, the simulation parameters are set in Table 6.1.

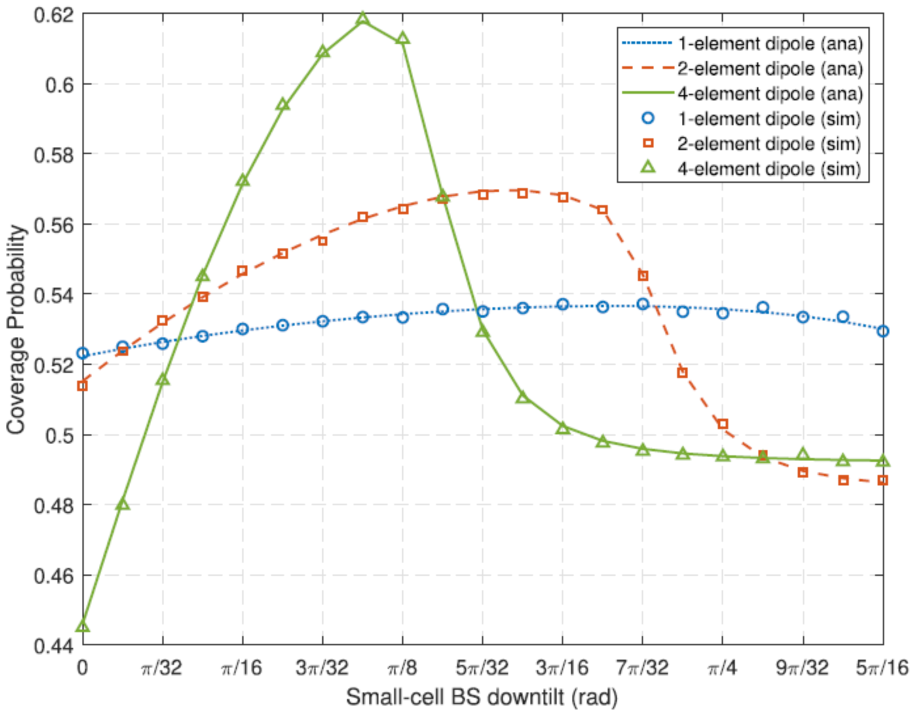

Fig. 6.2 Spatially-averaged coverage probability of a two-tier HTCN versus the SBS antenna downtilt for different numbers of SBS antenna elements in analysis and simulation, respectively.

In Fig. 6.2, the spatially-averaged coverage probabilities for different SBS antenna elements with no biasing of small cells are depicted in analysis and simulation, respectively. The antenna downtilt for the macro-cell tier is set at $\frac{\pi}{4}$ rad. According to [137], for 1-element dipole antenna, $n_S = 2.75$, SLL_S is not required, $G_{\mathrm{S_m}} = 2.15$ dBi; for 2-element dipole antenna, $n_{\mathrm{S}} = 11.73$, $SLL_{\mathrm{S}} = -10$ dB, $G_{\mathrm{S_m}} = 5.15$ dBi. It can be seen that analytical results match simulation results very well, which attests to the accuracy of derivations and the approximation method in Section 6.3. In addition, comparing curves for different numbers of SBS dipole elements, it can be observed that the SBS antenna downtilt angles increase first and then decrease as beams tilt down. The BS antenna with more elements leads to a larger maximum coverage probability. In general, the gain of the antenna element with a narrow vertical beamwidth is larger than that with a wide vertical beamwidth. The coverage probability for the 4-element antenna changes rapidly due to the small coverage for the narrow beam. Additionally, the optimal SBS antenna downtilt for the 4-element dipole antenna is smaller than that for other antennas because cell edge users cannot receive adequate desired signals when their associated SBSs provide large tilting beams.

6.5.2 Impact of MBS and SBS Antenna Downtilts, SBS Biasing, Height and Density

The numerical results of spatially-averaged coverage probability, ASE, and EE with respect to the MBS antenna downtilt, SBS antenna downtilt, SBS biasing, SBS height, and SBS density are obtained in this subsection.

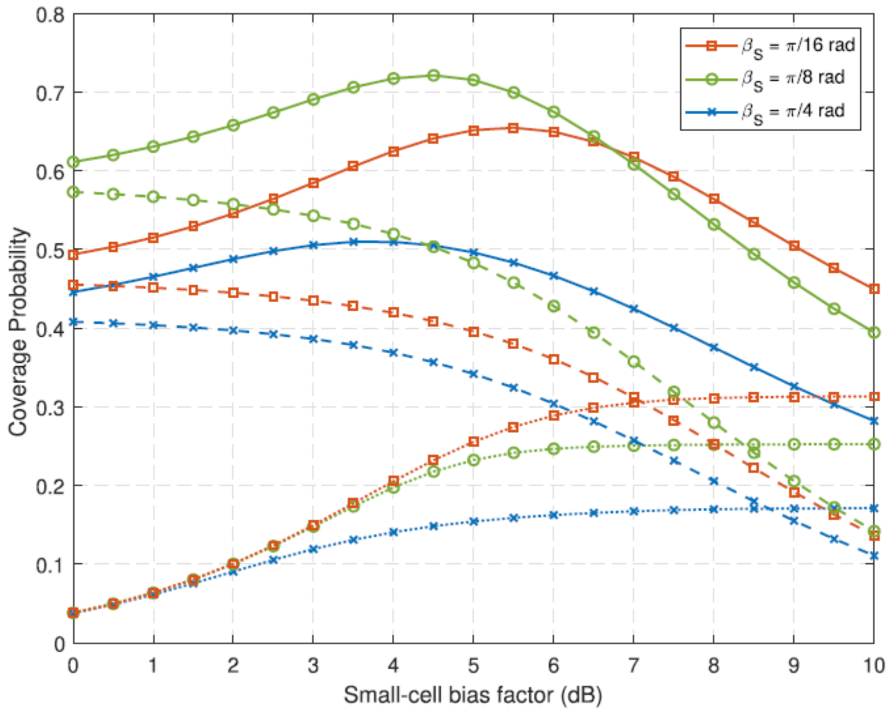

Fig. 6.3 Spatially-averaged coverage probability versus the small-cell association bias in the macro-cell tier (dotted lines), small-cell tier (dashed lines), and entire HTCN (solid lines) for different SBS antenna downtilts at $\beta_{\mathrm{M}} = \frac{\pi}{4}$ rad.

Fig. 6.3 illustrates the spatially-averaged coverage probability of the macro-cell tier, small-cell tier, and the entire HTCN versus the small-cell association bias at $\beta_{\mathrm{M}} = \frac{\pi}{4}$ rad and $\beta_{\mathrm{S}} = \frac{\pi}{16}, \frac{\pi}{8}, \frac{\pi}{4}$ rad, respectively. Each group of curves is shown with the same color and marker for a β_{S} setting. For each β_{S} considered, as small-cell association bias B_{S} rises, the coverage probability of the macro-cell tier increases and that of the small-cell tier decreases because users at the small-cell edge are transformed into macro-cell tier users, which results in the fact that the coverage probability for the entire HTCN first goes up and then drops down after reaching a maximum value. For each B_{S} considered, increasing β_{S} leads to the increase of macro-cell tier coverage probability, while the coverage probability of the small-cell tier first increases and then decreases. The maximum coverage probability of the entire HTCN achieves a much larger value at $\beta_{\mathrm{S}} = \frac{\pi}{8}$ rad than that at other

β_{S}. Since P_{M} is larger than P_{S}, MBSs can offer stronger received signals to increase the SIR of cell-edge users, which enables the enhancement in the coverage probability of the macro-cell tier, while weakening that of the small-cell tier to realize the traffic offloading from the small-cell tier to the macro-cell tier. As a result, an appropriate BS can balance the load of a HTCN and maximize the overall coverage probability for a given pair of β_{M} and β_{S}. For a given B_{S}, increasing β_{S} mitigates interference from the small-cell tier to MBS users, which improves the coverage probability of the macro-cell tier. However, the coverage probability of the small-cell tier decreases when beams from SBSs are close to the small-cell edge or small-cell center.

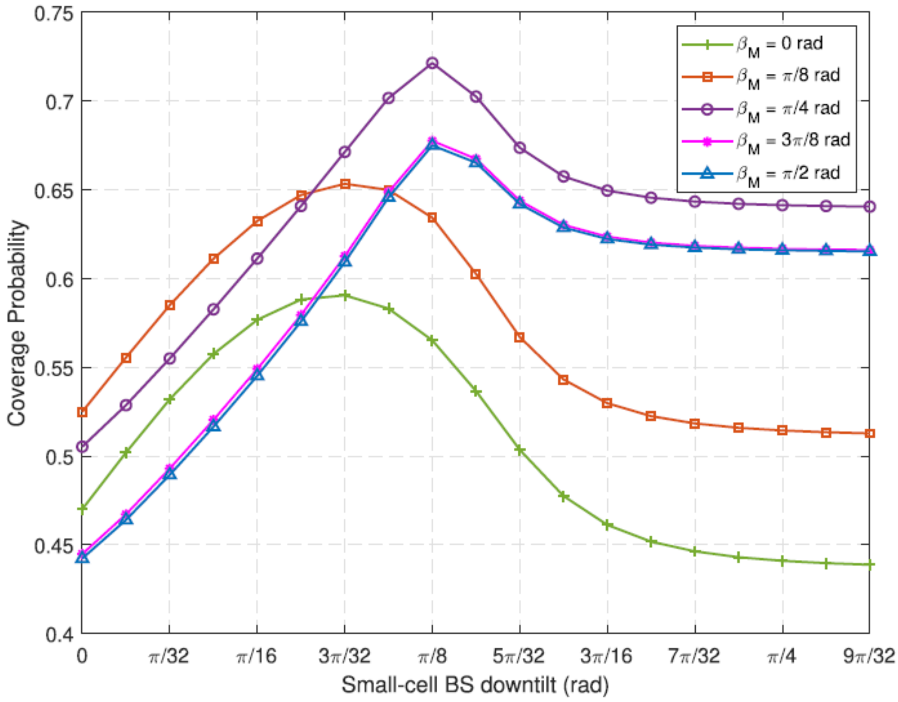

Fig. 6.4 Spatially-averaged coverage probability of a two-tier HTCN versus the SBS antenna downtilt for different MBS antenna downtilts.

Fig. 6.4 presents the spatially-averaged coverage probability in terms of β_{S} with $B_{\mathrm{S}} = 5$ dB for different β_{M} from 0 to $\frac{\pi}{2}$ rad. It is observed that for each β_{M}, the coverage probability first rises with β_{S} then declines after reaching a maximum value. The maximum coverage probability increases with the growth of β_{M} and achieves the largest value when β_{M} is around $\frac{\pi}{4}$ rad, then decreases and does not have a significant change in the large downtilt range. In general, small downtilts lead to much interference due to the overlapping among beams. As MBSs are higher than SBSs, the traffic for the small-cell tier is offloaded to the macro-cell tier when the biased association is applied. In this case, MBSs have larger coverage area than that in the unbiased association scheme, hence the optimal β_{M} is shown in the middle of the downtilt range. In addition, although large downtilts provide enough protection against interference, most users cannot receive sufficient desired power due to the small antenna gain.

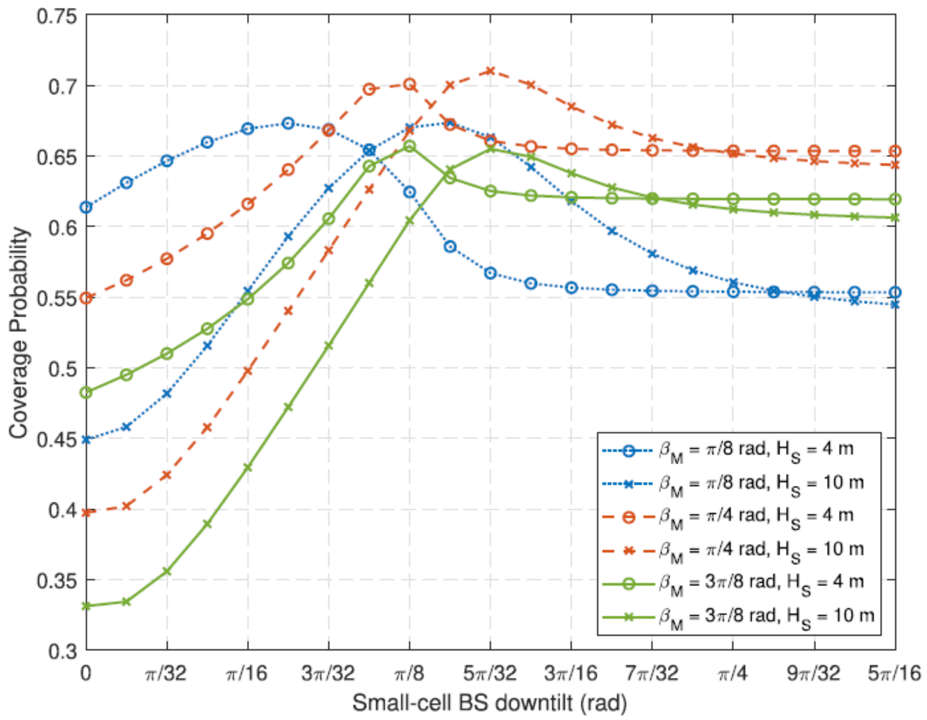

Fig. 6.5 Spatially-averaged coverage probability of a two-tier HTCN versus the SBS antenna downtilt for different SBS heights and MBS antenna downtilts.

In Fig. 6.5, the relationship between β_{S} and H_{S} is investigated with $B_{\mathrm{S}} = 5$ dB at $\beta_{\mathrm{M}} = \frac{\pi}{8}, \frac{\pi}{4}, \frac{3\pi}{8}$ rad, respectively. For each case, the coverage probability first goes up with the β_{S} then starts to drop after reaching a maximum value.

For each H_{S} considered, the maximum coverage probability first increases and then decreases with the increase of β_{M}. For each β_{M} considered, it is observed that the optimal β_{S} of taller SBSs is always larger than that of shorter SBSs, since $\theta_{\mathrm{S}} = \tan^{-1}\left(\frac{h_{\mathrm{S}}}{d}\right)$ illustrates that taller SBSs require larger antenna downtilt to improve the desired signal. In addition, larger downtilt can mitigate inter-cell interference. For the small value of β_{M}, the value of the maximum coverage probability of $H_{\mathrm{S}} = 4$ m is slightly higher than that of $H_{\mathrm{S}} = 10$ m, but is outstripped by that of $H_{\mathrm{S}} = 10$ m for the large value of β_{M}. When MBS antenna downtilt increases, a typical taller SBS user can suffer less interference from MBSs, whereas interfering beams are easier to point the area close to a typical shorter SBS user.

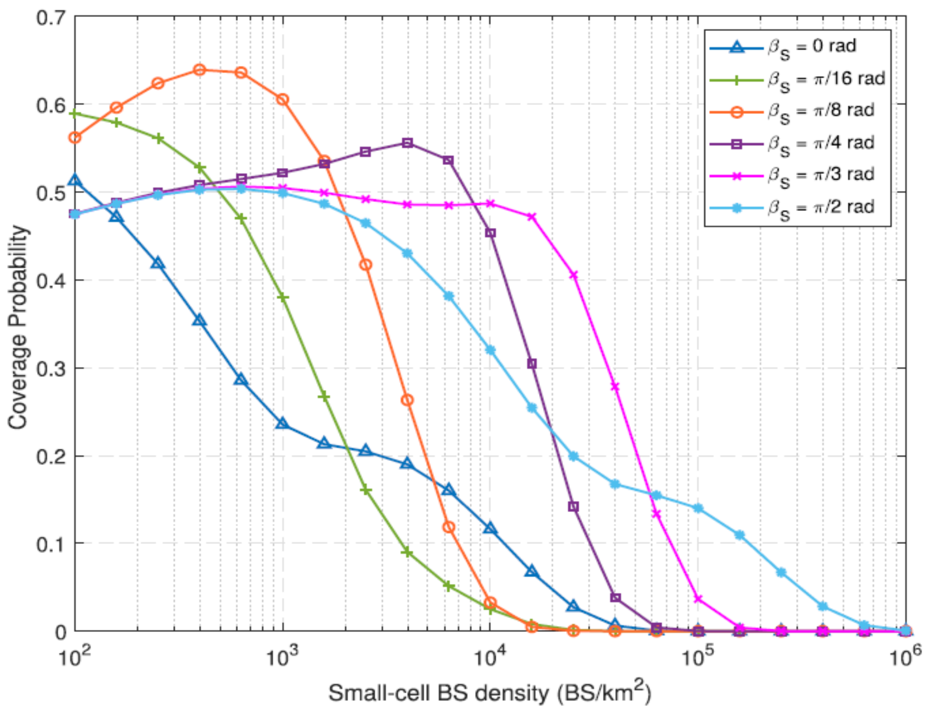

Fig. 6.6 Spatially-averaged coverage probability of a two-tier HTCN versus the small-cell BS density for different SBS antenna downtilts at $\beta_{\mathrm{M}} = \frac{\pi}{4}$ rad.

In Fig. 6.6, the effect of β_{S} and λ_{S} on the spatially-averaged coverage probability is considered with $B_{\mathrm{S}} = 0$ dB and $\beta_{\mathrm{M}} = \frac{\pi}{4}$ rad. It can be seen that the coverage probability decreases monotonically when $\beta_S < \frac{\pi}{16}$ rad; when $\beta_S > \frac{\pi}{16}$ rad, the coverage probability first goes up and then goes down after reaching a maximum value. In addition, the value of the maximum coverage probability increases with the increase of β_S, since massive SBSs leads to the growth of small-cell tier association probability and the shrinkage of the coverage area of each SBS. β_S rises to avoid beam overlapping and meet the demand of high SIR for cell center users. It is also observed that when the SBS antenna downtilt tends to $\frac{\pi}{2}$, there are two peaks on the curves. The first peak is much larger than the second peak because large β_S cannot supply adequate signals to SBS users. Small λ_S results in more users being associated with MBSs, which increases the coverage probability of the macro-cell tier.

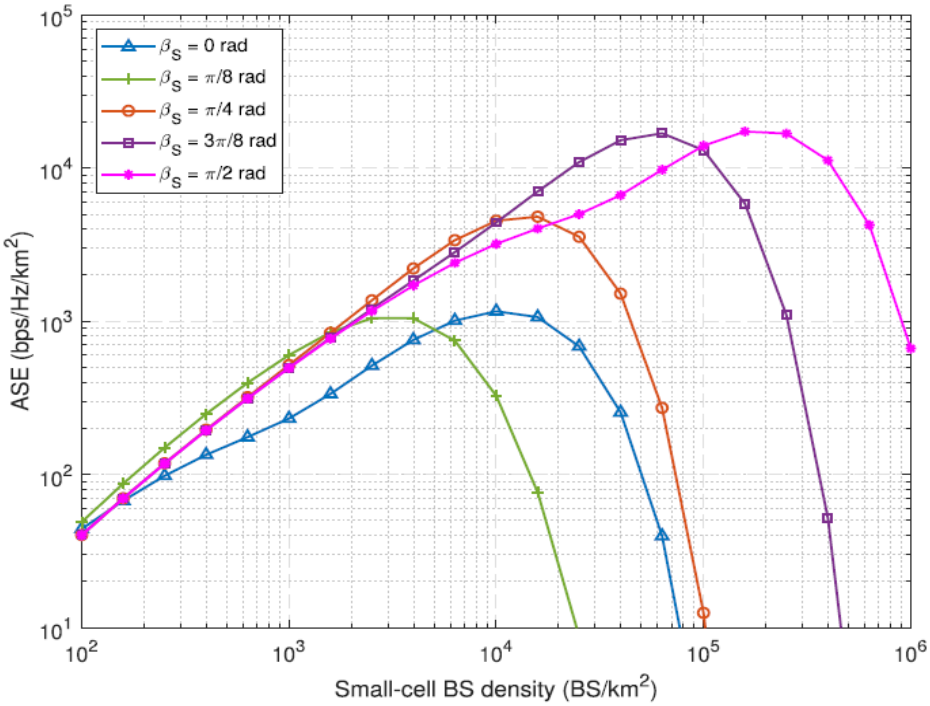

Fig. 6.7 ASE of a two-tier HTCN versus the small-cell BS density for different SBS antenna downtilts at $\beta_M = \frac{\pi}{4}$ rad.

From (6.45), the ASE versus λ_{S} with $B_S = 0$ dB for different β_{S} are presented in Fig. 6.7. It is shown that as β_{S} increases, the ASE ratchets up first then declines drastically after reaching a maximum value. The maximum ASE and the corresponding λ_{S} both boost as the β_{S} rises.

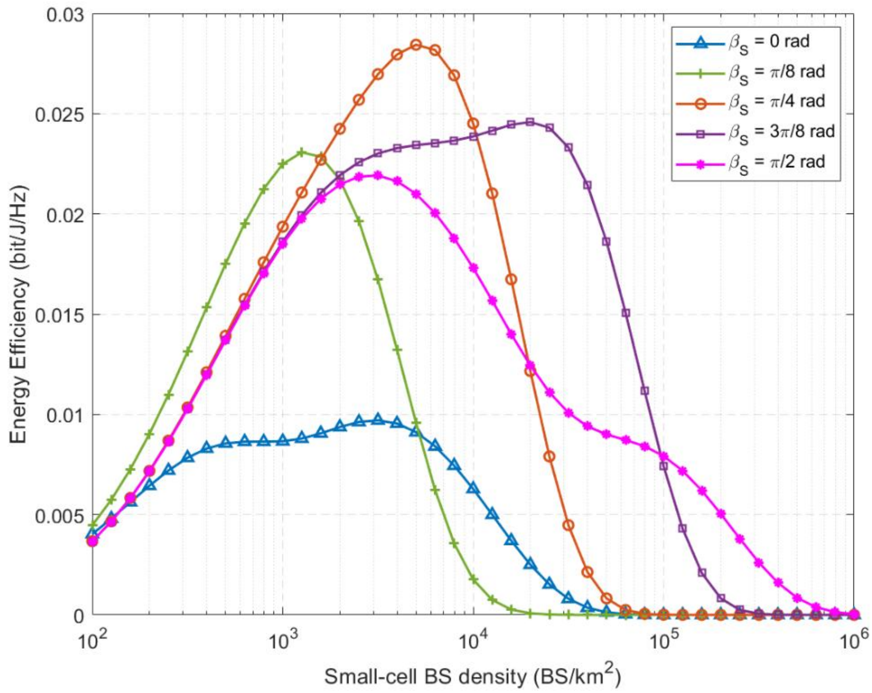

Fig. 6.8 EE of a two-tier HTCN versus the small-cell BS density for different SBS antenna downtilts at $\beta_{\mathrm{M}} = \frac{\pi}{4}$ rad.

From (6.46), the EE versus λ_{S} with $B_S = 0$ dB for different β_{S} are presented in Fig. 6.8. It can be seen that as β_{S} increases, the EE increases first and then drops after reaching a maximum value. When β_{S} is between $\frac{\pi}{8}$ rad and $\frac{3\pi}{8}$ rad, the value of the maximum EE first goes up and then goes down with the rise of β_{S}; When β_{S} tends to 0 or $\frac{\pi}{2}$, the value of the maximum EE is achieved at $\lambda_{\mathrm{S}}/\lambda_{\mathrm{M}} \approx 300$ due to the insufficiency of signals provided by SBSs.

6.5.3 The Optimal Downtilt Pair

In this subsection, the optimal MBS and SBS antenna downtilt pairs for various SBS heights and SBS densities are obtained. The uniqueness and type of the solution to (6.50) are analyzed as well. The spatially-averaged coverage probability with the optimal MBS and SBS antenna downtilt pair is compared to that with a pair of fixed MBS and SBS antenna downtilts.

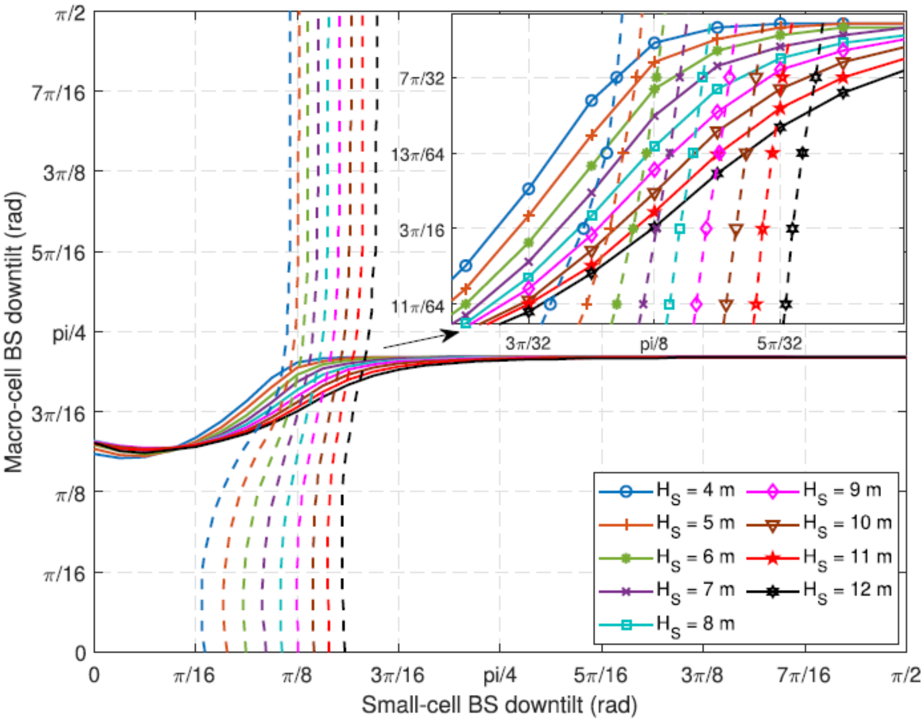

Fig. 6.9 Solutions to two equations in (6.50) for different SBS heights by holding β_{S} and β_{M} in the range of $\left[0, \frac{\pi}{2}\right]$, respectively.

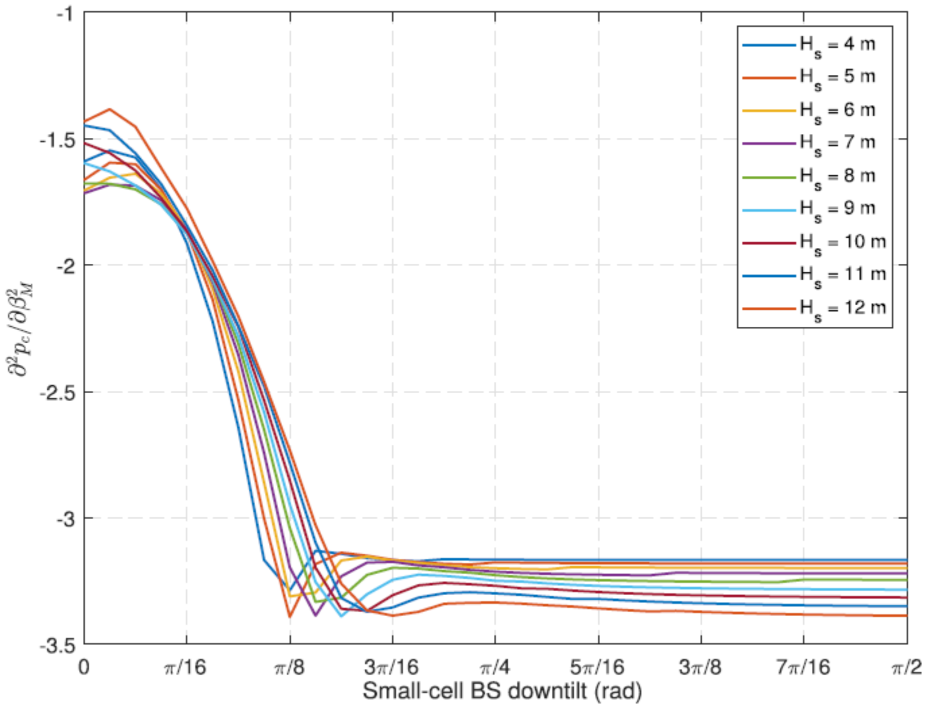

Fig. 6.10 Second derivative test results of (6.67) for different SBS heights.

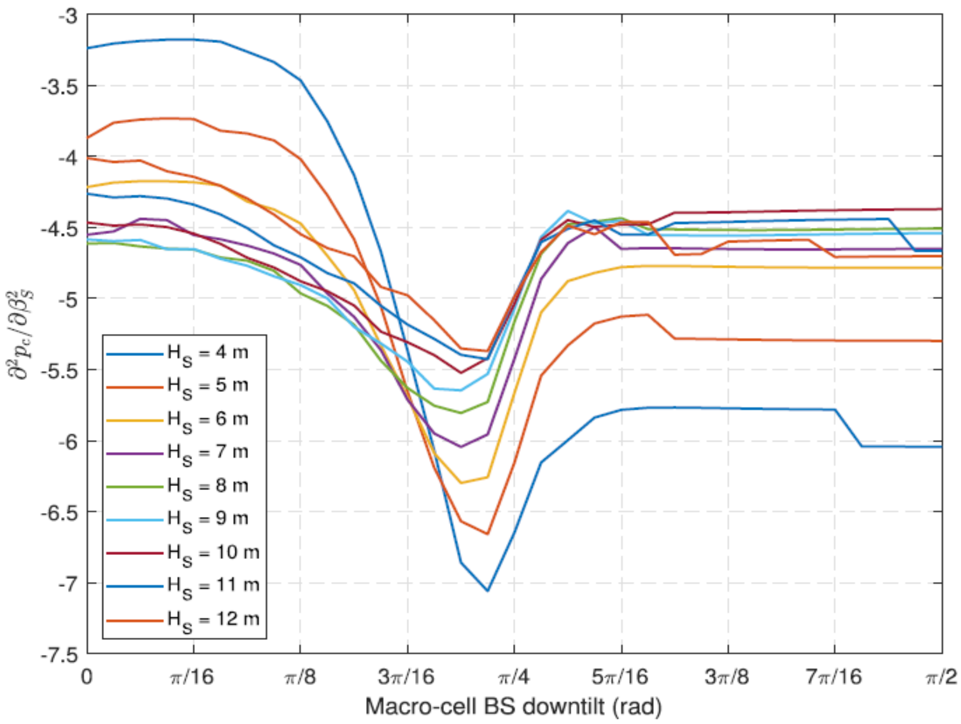

Fig. 6.11 Second derivative test results of (6.68) for different SBS heights.

Fig. 6.9 shows solutions to two equations in (6.50) for different SBS heights, where solid lines and dashed lines are solutions to $\mathcal{A}_{\mathrm{M}}\frac{\partial\mathcal{P}_{\mathrm{M}}}{\partial\beta_{\mathrm{M}}}+\mathcal{A}_{\mathrm{S}}\frac{\partial\mathcal{P}_{\mathrm{S}}}{\partial\beta_{\mathrm{M}}}=0$ for $\beta_{\mathrm{S}}\in\left[0,\frac{\pi}{2}\right]$ and $\mathcal{A}_{\mathrm{M}}\frac{\partial\mathcal{P}_{\mathrm{M}}}{\partial\beta_{\mathrm{S}}}+\mathcal{A}_{\mathrm{S}}\frac{\partial\mathcal{P}_{\mathrm{S}}}{\partial\beta_{\mathrm{S}}}=0$ for $\beta_{\mathrm{M}}\in\left[0,\frac{\pi}{2}\right]$, respectively. The intersection of the solid line and the dashed line for each H_{S} represents the stationary point $(\beta_{\mathrm{M}}^{*},\beta_{\mathrm{S}}^{*})$. It is obvious that there is only one intersection for each H_{S}, which proves the uniqueness of $(\beta_{\mathrm{M}}^{*},\beta_{\mathrm{S}}^{*})$. Fig. 6.10 and Fig. 6.11 present results of (6.66) and (6.67), respectively. As all results are below 0, it can be guaranteed that $(\beta_{\mathrm{M}}^{*},\beta_{\mathrm{S}}^{*})$ is the unique maximum point for a given H_{S}.

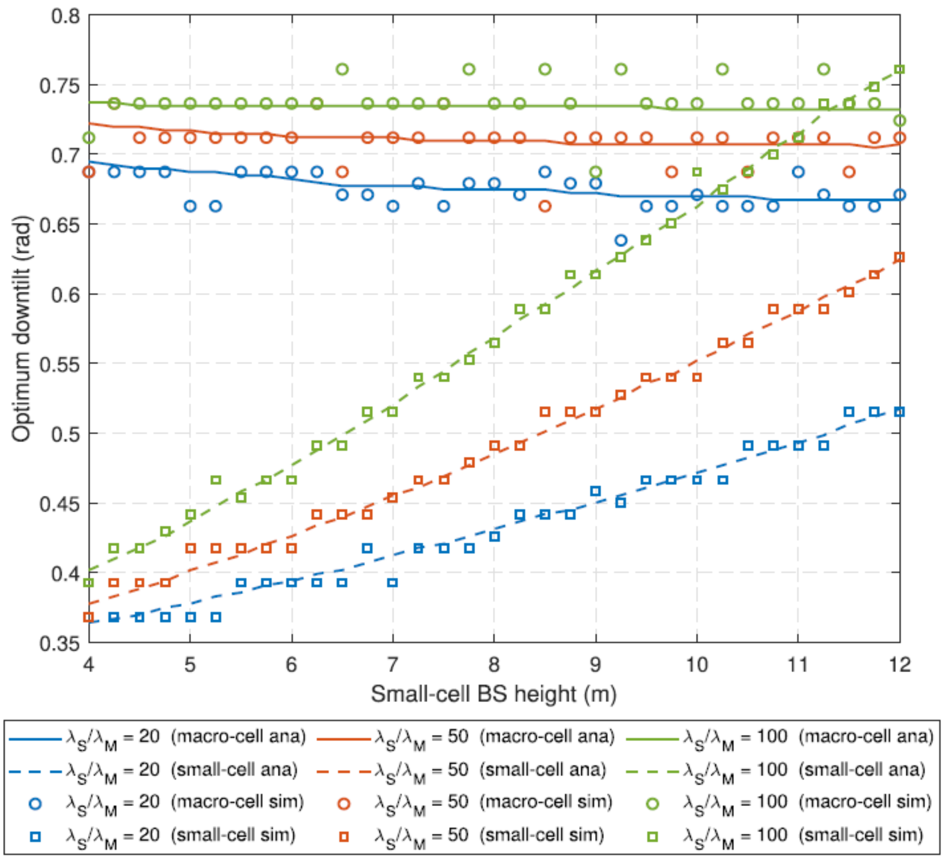

Fig. 6.12 The optimal MBS antenna downtilt and SBS antenna downtilt versus the SBS height for different small-cell BS densities in analysis and simulation, respectively.

Fig. 6.12 shows the optimal MBS antenna downtilt and SBS antenna downtilt obtained via the stationary points for different H_{S} and λ_{S}. There are some errors between the analysis and simulation due to the sampling intervals in Algorithm 6.1 and the simulation. Since the coverage probability at the optimal MBS and SBS antenna downtilt pair and that at the adjacent pair have negligible differences, these errors are acceptable. For each λ_{S} considered, the optimal SBS antenna downtilt grows monotonically as H_{S} increases to reduce interference in the small-cell tier. The optimal MBS antenna downtilt decreases quite slightly, which illustrates that it is not strongly affected by H_{S}. For each H_{S} considered, deploying more SBSs increases both optimal MBS antenna downtilt and SBS antenna downtilt to enhance signals and reduce inter-cell interference due to the overlap among beams in both tiers.

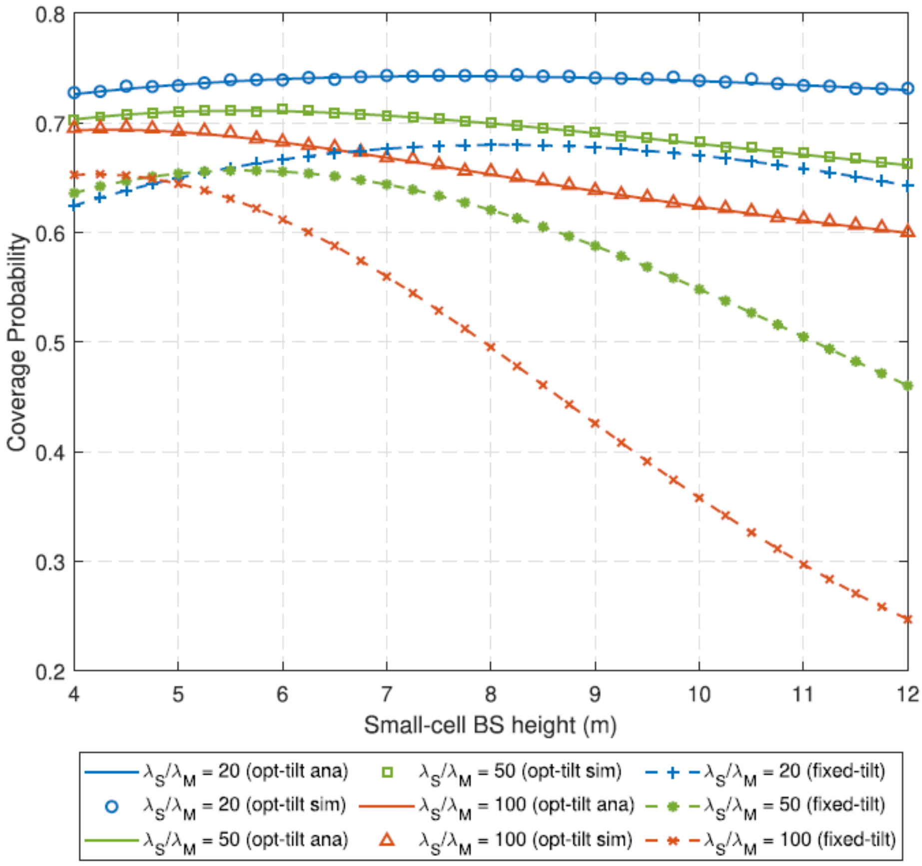

Fig. 6.13 Comparison of the spatially-averaged coverage probability with or without the optimal pair of MBS and SBS antenna downtilts versus the SBS height for different SBS densities in analysis and simulation, respectively.

Fig. 6.13 represents the spatially-averaged coverage probability with the corresponding optimal MBS and SBS antenna downtilts for varying H_S and λ_S in analysis and simulation, respectively. It is exhibited that for each H_S considered, increasing λ_S degrades the coverage probability. Although all coverage probabilities are obtained when the optimal pairs of MBS and SBS antenna downtilts are applied, adding redundant SBSs still increases beams overlapping to MBSs because of the reduction of MBS association probability. This can also explain why the dense small-cell tier requires lower SBSs in this figure. For each H_S and λ_S considered, the downlink coverage probability of an HTCN is significantly improved by optimizing the MBS and SBS antenna downtilts pair.

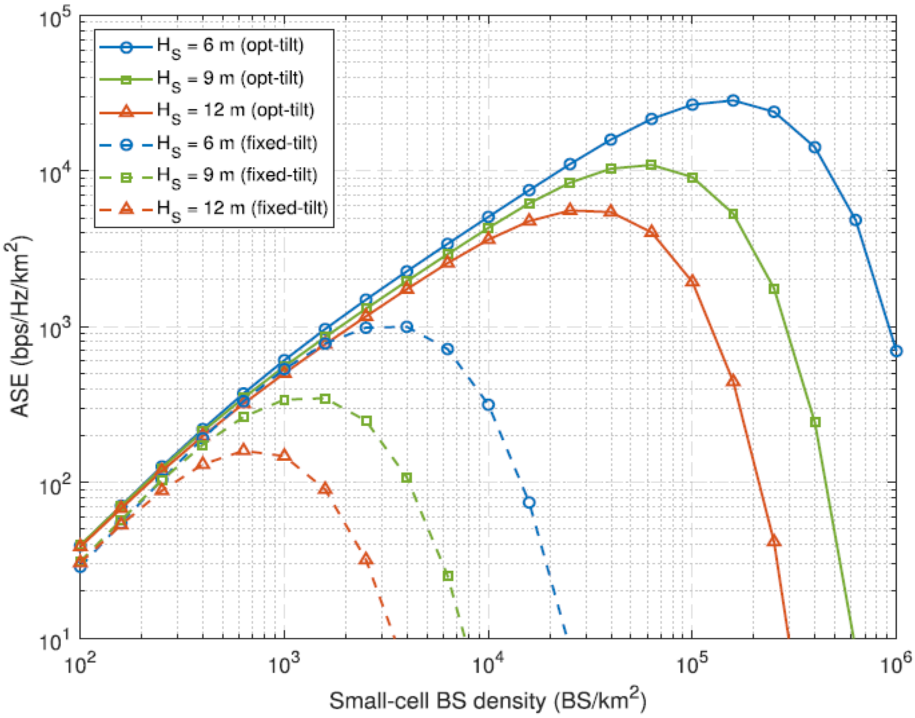

Fig. 6.14 Comparison of ASE with or without the optimal pair of MBS and SBS antenna downtilts versus the SBS density for different SBS heights.

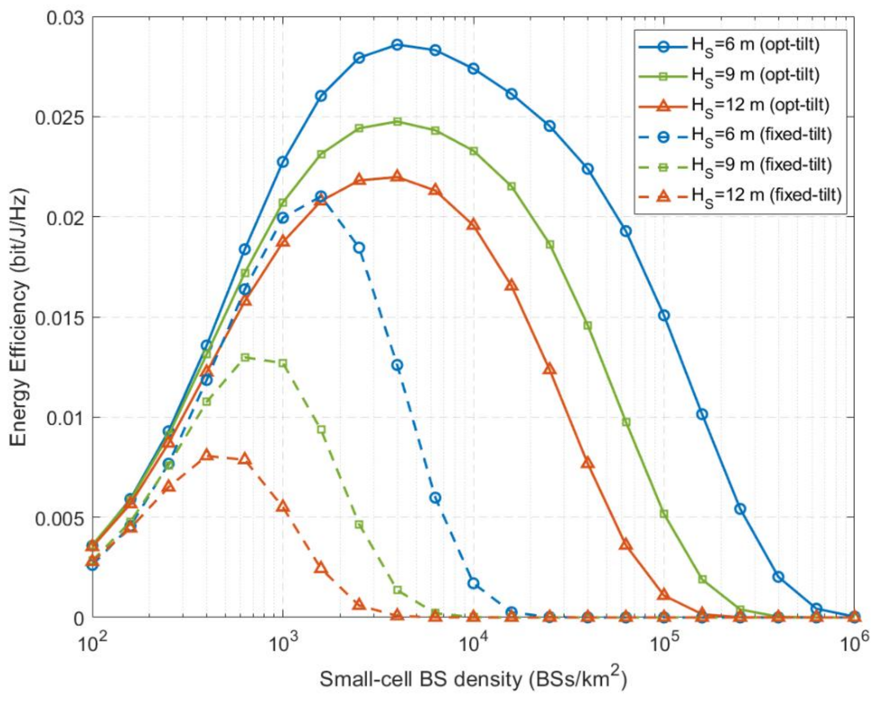

Fig. 6.15 Comparison of EE with or without the optimal pair of MBS and SBS antenna downtilts versus the SBS density for different SBS heights.

Fig. 6.14 and Fig. 6.15 plot the ASE and EE with the optimal MBS antenna downtilt and SBS antenna downtilt and that with the fixed MBS antenna downtilt and SBS antenna downtilt versus the λ_{S} for different H_{S}, respectively. It can be seen that for each case, the ASE and EE first increases with λ_{S} and then starts to decrease after reaching a maximum value. For each H_{S} considered, the optimal pair of MBS and SBS antenna downtilts achieve much larger values of the maximum ASE and EE than the case without optimizing the BS antenna downtilts. For each H_{S} and λ_{S} considered, the HTCN with the optimal pair of MBS and SBS antenna downtilts brings about significant ASE and EE enhancements. Additionally, with or without optimizing the BS antenna downtilts, for the same λ_{S}, the ASE and EE decrease with the increase of H_{S}.

6.6 Summary

In this chapter, a two-tier HTCN with an SG framework is proposed to analyze the downlink spatially-averaged coverage probability, ASE, and EE when considering the antenna downtilts in both tiers as optimization parameters. To facilitate the computation efficiency, the Gauss-Chebyshev quadrature method is leveraged for approximating integral parts in Laplace transforms. Results indicate that adjusting BS antenna downtilts in both tiers has a significant impact on the spatially-averaged coverage probability, ASE, and EE of HTCNs. Under the minimum biased transmission distance user association scheme, the SBS antenna height, SBS association bias, SBS density, and SBS transmit power can determine the optimal BS antenna downtilt. The lower bound of cell-edge coverage probability is derived under the scenario of unbiased association and equal path loss components, resulting in a closed-form expression that provides a useful insight into practical HTCN deployments.

The optimal MBS antenna downtilt and SBS antenna downtilt pair is then derived to maximize the spatially-averaged coverage probability, ASE, and EE. Results lead to the conclusion that the optimal SBS antenna downtilt increases as the height of SBS rises to alleviate the inter-cell interference, while MBS antenna downtilt does not significantly change. Moreover, the SBS height, SBS density, and SBS transmit power still have impact on the spatially-averaged coverage probability, ASE, and EE on condition that antenna downtilts in both tiers are optimal. The presented model shows that the MBS antenna downtilt and SBS antenna downtilt can be adapted effectively to improve the performance of HTCNs in terms of the spatially-averaged coverage probability, ASE, and EE.

Chapter 7

Conclusions and Future Work

In this chapter, the key points of this thesis and the contributions of our research effort are first summarized and highlighted. After that, further research on 3D beamforming in cellular networks and the potential directions for future investigations are presented and suggested.

In this thesis, the performance of BS antenna downtilts in 3D cellular networks is investigated. The analytical transmission models to investigate the impact of BS antenna downtilts on mm-Wave cellular networks and HTCNs are proposed. Joint optimization approaches for BS antenna downtilts and network statistical measures are developed to maximize the performance of mm-Wave cellular networks and HTCNs.

Existing works on optimizing BS antenna downtilt always set the BS antenna height with specific values. However, in the 3D deployment of mm-Wave networks, the BS antenna height cannot be ignored in the 3D antenna array design. Therefore, the joint impact of BS antenna height and downtilt in 3D mm-Wave networks is taken into account in Chapter 3, and numerical results are presented to determine the joint optimal BS antenna height and downtilt that maximize the cell-averaged downlink SE in a mm-Wave network.

Based on the network model in Chapter 3, a multi-cell multi-user mmWave B-MIMO network utilizing a beam-selection method is investigated in Chapter 4 to address the existing research gap, which primarily focuses on single-cell networks. The numerical results show that adjusting the BS antenna downtilts and heights appropriately can significantly enhance the cell-averaged SE under various precoding schemes, and the beam-selection method can provide considerable improvements on the EE compared to the full-beam strategy.

Due to the lack of efficient approaches for BS antenna downtilt optimization in existing studies, a joint optimization algorithm for mm-Wave cellular networks is developed in Chapter 5. The optimal precoding and BS antenna downtilting are obtained for network sum SE maximization. The simulation results show that the joint optimization of precoding and BS antenna downtilt leads to a significant enhancement in the sum SE of mm-Wave cellular networks.

In Chapter 6, the impact of BS antenna downtilt across all tiers in HTCNs is investigated to fill the existing research gap that only focuses on MBS antenna downtilts. The cell-edge coverage probability is studied in special and practical scenarios. The optimal BS antenna downtilts for both macro cells and small cells that maximize the coverage probability, ASE, and EE of HTCNs are obtained. The results demonstrate that jointly optimizing BS antenna downtilts across all tiers can significantly enhance the performance of HTCNs.

7.1 Conclusions

In this section, the key points of this thesis are summarized, and the contributions resulting from the conducted research efforts are concluded.

BS antenna downtilts have a significant impact on the performance of downlink mm-Wave cellular networks and HTCNs:

Analytical expressions for 3D mm-Wave cellular networks as functions of BS antenna downtilts and antenna heights are derived in Section 3.2 and Section 4.2. In Section 3.2, inter-cell interference is considered, and a simplified beamforming scheme is utilized for the transmission model. In Section 4.2, intra-cell and inter-cell interference are both taken into account in the context of employing WF and ZF precoding schemes, along with the implementation of a low-complexity beam-selection method. It can be seen that proper BS antenna downtilt and antenna height can significantly improve the cell-averaged downlink SE and EE in mm-Wave cellular networks.

In Section 6.2 and Section 6.3, the SG is utilized and a tractable system model with each tier of BSs drawn following an independent HPPP is proposed. Analytical expressions for the spatially-averaged coverage probability, cell-edge average coverage probability, ASE, and EE as functions of the BS antenna downtilts, heights, densities, and SBS association bias are derived. It is shown that under the minimum biased transmission distance user association scheme, adjusting BS antenna downtilts in both tiers, BS antenna heights, densities, and SBS association bias appropriately can notably enhance the spatially-averaged coverage probability, ASE, and EE of HTCNs. However, BS antenna downtilts and transmit power in both tiers have no significant impact on the cell-edge average coverage probability under specific assumptions in practical BS deployment scenarios. It is noted that BS antenna downtilts can be adapted effectively to reduce the cost and improve the cell-wide performance of downlink HTCNs.

Accurate approximation approaches are efficient for fast numerical evaluation:

Due to the complexity of the integral parts in analytical expression computations, numerical approaches are developed for fast and accurate computation. The approach proposed in Section 3.3 and Section 4.3.2 are based on the Riemann sum approximation. Therein, the coverage area is divided into equilateral triangle grids to approximate the continuous distribution of user positions by discretizing user positions. It is demonstrated that the discrete approximation approach with dense grids is highly precise in evaluating the provided analytical expressions. In Section 6.3.1, the Gauss-Chebyshev quadrature method is leveraged to transform the definite integral of the spatially-averaged coverage probability function into a weighted sum of the spatially-averaged coverage probability function. It can be seen that this method not only improves the computation efficiency but also ensures the accuracy of the calculations in a tractable system model.

Joint BS antenna downtilts optimization is critical for 3D cellular network deployment:

The works in Chapter 3 and Chapter 4 suggest that the optimal pair of BS antenna downtilt and antenna height can be obtained via the numerical search. The optimized trade-off between the BS antenna downtilts and heights can sustain an optimal mm-Wave cellular network performance.

In Chapter 5, the joint optimal precoding and BS antenna downtilting for 3D downlink mm-Wave cellular network sum SE maximization is obtained by an iterative algorithm leveraging the AO and FP techniques. The results confirm the feasibility and effectiveness of the proposed algorithm in performing joint optimization to maximize the network sum SE. The sum SE achieved through the joint optimal precoding and BS antenna downtilt shows significant enhancement compared to those using fixed precoding, fixed BS antenna downtilt, or the absence of elevation beamforming.

Additionally, the optimal BS antenna downtilts across both tiers of the HTCN that maximize the downlink spatially-averaged coverage probability are determined by using the partial derivative and the bisection method in Chapter 6. The presented results lead to the conclusion that the optimal SBS antenna downtilt increases with the rise in the SBS height and density, which helps mitigate inter-cell interference; the optimal MBS antenna downtilt increases with the rise in the SBS density, while does not vary significantly with the change of SBS height. The spatially-averaged coverage probability, ASE, and EE with the optimal BS antenna downtilt pair in HTCNs can achieve a significant improvement compared to those with the fixed BS antenna downtilt pair.

7.2 Future Works

In this thesis, the impact of 3D antenna radiation pattern on mmWave cellular networks and HTCNs is studied, and the BS antenna downtilt is optimized to improve the performance of 3D cellular networks. According to the works conducted in this thesis, potential topics for future research are summarized.

The downlink transmission in 3D mm-Wave cellular networks and 3D HTCNs is considered in Chapters 3 through 6. However, there remain some limitations in current works of 3D beamforming design. Given its status as one of the foremost challenges in 3D cellular network deployment design, further research in the following areas is deemed valuable.

BS antenna downtilt design for NLOS/indoor scenarios:

The typical LOS propagation scenarios are considered in the conducted research. In some specific scenarios, for instance, large indoor environments such as galleries, warehouses, and airports, obstacles and reflectors affect the signal propagation process. The blockages and reflections in the signal propagation process could be investigated further to see how they affect the BS antenna downtilt design in cellular networks.

BS antenna downtilt design in MIMO systems under Imperfect CSI:

The conducted research investigates network performance with perfect CSI availability at the transmitters. However, in some specific scenarios, BS has to estimate the channel response within a specific coherence interval. Therefore, it is worth designing and optimizing BS antenna downtilt for MIMO systems in scenarios where the BS performs channel estimation.

Interference management techniques in HTCNs with 3D beamforming:

As reviewed in Section 2.4.1, several interference management techniques have been proposed to improve the performance of HTCNs. The efficacy of these interference management techniques on the design of 3D beamforming in HTCNs can be investigated, leading to the proposal of optimizing 3D beamforming schemes to enhance the performance of HTCNs.

3D beamforming in 3D mobile networks:

The BSs in conducted works are distributed in the 2D area, thereby the BS antenna tilt is in the range between 0° and 90°. With the development of wireless communication technology, the 3D distributed BSs/APs have been put forward recently [205], [206]. The maximum BS antenna tilt can be extended to 180° by the design of 3D beamforming in 3D mobile networks.

The key challenge would be the vertical distance between the BS antenna and the UE from being fixed to dynamic.

I am keen on ongoing research in 3D beamforming design to enhance its usability and performance, inspire further investigations in wireless networks, and drive the development of innovative applications that ultimately contribute to economic growth and societal advancement.

Bibliography

[1] E. G. Larsson, O. Edfors, F. Tufvesson, and T. L. Marzetta, “Massive MIMO for next generation wireless systems,” *IEEE Commun. Mag.*, vol. 52, no. 2, pp. 186–195, 2014.

[2] A. Hoglund *et al.*, “Overview of 3GPP Release 14 Enhanced NB-IoT,” *IEEE Netw.*, vol. 31, no. 6, pp. 16–22, 2017.

[3] M. Shafi *et al.*, “5G: A tutorial overview of standards, trials, challenges, deployment, and practice,” *IEEE J. Sel. Areas Commun.*, vol. 35, no. 6, pp. 1201–1221, 2017.

[4] 3GPP TR 36.897 V13.0.0, “Study on elevation beamforming/Full-Dimension (FD) MIMO for LTE,” 2015.

[5] Y. H. Nam *et al.*, “Full-dimension MIMO (FD-MIMO) for next generation cellular technology,” *IEEE Commun. Mag.*, vol. 51, no. 6, pp. 172–179, 2013.

[6] Y. KIM *et al.*, “Full dimension MIMO (FD-MIMO): The next evolution of MIMO in LTE systems,” *IEEE Wireless Communications*, vol. 21, no. 2, pp. 26–33, 2014.

[7] S. M. Razavizadeh, M. Ahn, and I. Lee, “Three-dimensional beamforming: A new enabling technology for 5G wireless networks,” *IEEE Signal Process. Mag.*, vol. 31, no. 6, pp. 94–101, 2014.

[8] F. Athley and M. N. Johansson, “Impact of electrical and mechanical antenna tilt on LTE downlink system performance,” *IEEE Veh. Technol. Conf.*, pp. 1–5, 2010.

[9] N. Seifi, M. Coldrey, M. Matthaiou, and M. Viberg, “Impact of base station antenna tilt on the performance of network MIMO systems,” in *IEEE Vehicular Technology Conference*, 2012.

[10] A. Kammoun, H. Khanfir, Z. Altman, M. Debbah, and M. Kamoun, “Preliminary results on 3D channel modeling: From theory to standardization,” *IEEE J. Sel. Areas Commun.*, vol. 32, no. 6, pp. 1219–

1229, 2014.

[11] W. Lee, S. R. Lee, H. B. Kong, and I. Lee, "3D beamforming designs for Single User MISO systems," in *GLOBECOM - IEEE Global Telecommunications Conference*, 2013, pp. 3914–3919.

[12] W. Lee, S. Lee, H. Kong, and I. Lee, "Downlink Vertical Beamforming Designs for Active Antenna Systems," *IEEE Trans. Commun.*, vol. 62, no. 6, pp. 1897–1907, 2014.

[13] W. Lee, S. R. Lee, H. B. Kong, H. J. Kim, and I. Lee, "Downlink vertical beamforming designs for multi-user MISO systems," *IEEE Veh. Technol. Conf.*, vol. 2015, pp. 0–4, 2015.

[14] W. Yin, L. Li, X. Li, Z. Wang, and L. Xie, "Downlink performance analysis of multicell multiuser 3D MIMO system," *2015 IEEE 82nd Veh. Technol. Conf.*, pp. 1–5, 2015.

[15] W. Guo, S. Wang, Y. Wu, J. Rigelsford, X. Chu, and T. O'Farrell, "Spectral-and energy-efficient antenna tilting in a HetNet using reinforcement learning," *IEEE Wirel. Commun. Netw. Conf. WCNC*, pp. 767–772, 2013.

[16] R. Hernandez-Aquino, S. A. R. Zaidi, D. McLernon, M. Ghogho, and A. Imran, "Tilt Angle Optimization in Two-Tier Cellular Networks-A Stochastic Geometry Approach," *IEEE Trans. Commun.*, vol. 63, no. 12, pp. 5162–5177, 2015.

[17] A. Hu, "Antenna Tilt Design for Millimeter-Wave Beamspace MIMO Systems," *Wirel. Pers. Commun.*, vol. 94, no. 3, pp. 1701–1713, 2017.

[18] X. Liu, J. Xu, R. Shu, and Y. Li, "Impact of Height and Downtilt of Base Station Antenna for Millimeter-Wave Communication Networks with 3D LoS Probability," *2019 11th Int. Conf. Wirel. Commun. Signal Process.*, pp. 1–6, 2019.

[19] H. S. Dhillon, R. K. Ganti, F. Baccelli, and J. G. Andrews, "Modeling and analysis of K-tier downlink heterogeneous cellular networks," *IEEE J. Sel. Areas Commun.*, vol. 30, no. 3, pp. 550–560, 2012.

[20] M. Baianifar, S. Khavari, S. M. Razavizadeh, and T. Svensson, "Impact of user height on the coverage of 3D beamforming-enabled massive MIMO systems," *IEEE Int. Symp. Pers. Indoor Mob. Radio Commun. PIMRC*, vol. 2017-Octob, pp. 1–5, 2018.

[21] M. Baianifar, S. M. Razavizadeh, H. Akhlaghpasand, and I. Lee, "Energy efficiency maximization in mmWave wireless networks with 3D beamforming," *J. Commun. Networks*, vol. 21, no. 2, pp. 125–135, 2019.

[22] R1-122034, "Study on 3D channel model for elevation beamforming and FD-MIMO studies for LTE," *3GPP TSG RAN Plenary*, no. 58, Barcelona, Spain, Dec-2012.

[23] RP-141831, "Revised SID: Study on elevation beamforming/full-Dimension (FD) MIMO for LTE," *Samsung, Nokia Networks,* 2014.

[24] RP-160623, "New WID Proposal: Enhancements on Full-Dimension (FD) MIMO for LTE," *3GPP TSG RAN Meet.*, no. 71, 2016.

[25] I. F. Akyildiz, W. Su, Y. Sankarasubramaniam, and E. Cayirci, "Full Dimension MIMO (FD-MIMO): The Next Evolution of MIMO in LTE Systems," *IEEE Commun. Mag.*, vol. 21, no. 3, pp. 92–100, 2014.

[26] W. Liu, Z. Wang, C. Sun, S. Chen, and L. Hanzo, "Structured Non-Uniformly Spaced Rectangular Antenna Array Design for FD-MIMO Systems," *IEEE Trans. Wirel. Commun.*, vol. 16, no. 5, pp. 3252–3266, 2017.

[27] H. Ji *et al.*, "Overview of Full-Dimension MIMO in LTE-Advanced Pro," *IEEE Commun. Mag.*, vol. 55, no. 2, pp. 176–184, 2017.

[28] B. Debaillie *et al.*, "Analog/RF Solutions Enabling Compact Full-Duplex Radios," *IEEE J. Sel. Areas Commun.*, vol. 32, no. 9, pp. 1662–1673, 2014.

[29] Y. Li *et al.*, "Implementation of Full-Dimensional MIMO (FD-MIMO) in LTE," in *2013 Asilomar Conference on Signals, Systems and Computers*, 2013, vol. 8, no. 5, pp. 998–1003.

[30] G. Xu *et al.*, "Full Dimension MIMO (FD-MIMO): Demonstrating

Commercial Feasibility," *IEEE J. Sel. Areas Commun.*, vol. 35, no. 8, pp. 1876–1886, 2017.

[31] G. Liu, X. Hou, F. Wang, J. Jin, H. Tong, and Y. Huang, "Achieving 3D-MIMO With Massive Antennas From Theory to Practice With Evaluation and Field Trial Results," *IEEE Syst. J.*, vol. 11, no. 1, pp. 1–10, 2016.

[32] J. Zhang, C. Pan, F. Pei, G. Liu, and X. Cheng, "Three-dimensional fading channel models: A survey of elevation angle research," *IEEE Commun. Mag.*, vol. 52, no. 6, pp. 218–226, 2014.

[33] B. Mondal, T. A. Thomas, and E. Visotsky, "3D channel model in 3GPP," *IEEE Commun. Mag.*, vol. 53, no. 3, pp. 16–23, 2015.

[34] A. Roivainen, V. Hovinen, J. Meinila, N. Tervo, M. Sonkki, and C. F. Dias, "Elevation analysis for urban microcell outdoor measurements at 2.3 GHz," *Proc. 2014 1st Int. Conf. 5G Ubiquitous Connect. 5GU 2014*, pp. 176–180, 2014.

[35] M. Zhai, J. Li, Y. Liang, T. Li, G. Gui, and F. Li, "A novel coupling mode based 3D MIMO channel modeling and capacity analysis for 5G," *2016 IEEE Int. Conf. Ubiquitous Wirel. Broadband, ICUWB 2016*, no. 66, 2016.

[36] Y. Yu, J. Zhang, and M. Shafiy, "3D vs. 2D channel capacity of outdoor to indoor scenarios derived from measurements in China and New Zealand," *Eur. Signal Process. Conf.*, vol. 2016-Novem, pp. 1980–1984, 2016.

[37] X. Pu, X. Li, H. Tang, R. Han, Q. Chen, and A. S. Model, "Optimal Transmit Antenna Placement for Short-Range Indoor 3D MIMO Channels," in *2018 IEEE Wireless Communications and Networking Conference (WCNC)*, 2018, pp. 1–6.

[38] Y. Zhang *et al.*, "3-D MIMO Parametric Stochastic Channel Model for Urban Macrocell Scenario," *IEEE Trans. Wirel. Commun.*, vol. 16, no. 7, pp. 4246–4260, 2017.

[39] S. Kutty and D. Sen, "Beamforming for Millimeter Wave

Communications: An Inclusive Survey," *IEEE Commun. Surv. Tutorials*, vol. 18, no. 2, pp. 949–973, 2016.

[40] H. Halbauer, S. Saur, J. Koppenborg, and C. Hoek, "3D Beamforming Performance Improvement for Cellular Networks," *Bell Labs Tech. J.*, vol. 18, no. 2, pp. 37–56, 2013.

[41] V. Venkateswaran and A. J. Van Der Veen, "Analog beamforming in MIMO communications with phase shift networks and online channel estimation," *IEEE Trans. Signal Process.*, vol. 58, no. 8, pp. 4131–4143, 2010.

[42] S. Han, C. L. I, Z. Xu, and C. Rowell, "Large-scale antenna systems with hybrid analog and digital beamforming for millimeter wave 5G," *IEEE Commun. Mag.*, vol. 53, no. 1, pp. 186–194, 2015.

[43] S. Saur and H. Halbauer, "Exploring the vertical dimension of dynamic beam steering," *2011 8th Int. Work. Multi-Carrier Syst. Solut. MC-SS 2011*, 2011.

[44] N. Gresset, H. Halbauer, J. Koppenborg, W. Zirwas, and H. Khanfir, "Interference-Avoidance Techniques:Improving Ubiquitous User Experience," *IEEE Veh. Technol. Mag.*, vol. 7, no. 4, pp. 37–45, 2012.

[45] J. Koppenborg, H. Halbauer, S. Saur, and C. Hoek, "3D beamforming trials with an active antenna array," *2012 16th Int. ITG Work. Smart Antennas, WSA 2012*, pp. 110–114, 2012.

[46] H. Halbauer, S. Saur, J. Koppenborg, and C. Hoek, "Interference avoidance with dynamic vertical beamsteering in real deployments," *2012 IEEE Wirel. Commun. Netw. Conf. Work. WCNCW 2012*, pp. 294–299, 2012.

[47] H. Halbauer, J. Koppenborg, J. Holfeld, M. Danneberg, M. Grieger, and G. Fettweis, "Field Trial Evaluation of 3D Beamforming in a Multicell Scenario," *WSA 2013 - 17th Int. ITG Work. Smart Antennas*, vol. 9, pp. 3–9, 2013.

[48] Radiocommunication Sector of International Telecommunication Union,

"Report ITU-R M.2135-1: Guidelines for evaluation of radio interface technologies for IMT-advanced," 2009.

[49] 3GPP TR 36.814 V9.0.0, "Evolved Universal Terrestrial Radio Access (E-UTRA); Further advancements for E-UTRA physical layer aspects (Release 9)," *3rd Gener. Partnersh. Proj. Tech. Rep*, vol. 9, no. 3, pp. 1–104, 2010.

[50] N. Seifi, M. Coldrey, and M. Viberg, "Throughput optimization for MISO interference channels via coordinated user-specific tilting," *IEEE Commun. Lett.*, vol. 16, no. 8, pp. 1248–1251, 2012.

[51] N. Seifi, M. Coldrey, and T. Svensson, "Throughput optimization in MU-MIMO systems via exploiting bs antenna tilt," in *2012 IEEE Globecom Workshops, GC Wkshps 2012*, 2012, pp. 653–657.

[52] B. Partov, D. J. Leith, and R. Razavi, "Utility Fair Optimization of Antenna Tilt Angles in LTE Networks," *IEEE/ACM Trans. Netw.*, vol. 23, no. 1, pp. 175–185, 2015.

[53] 3GPP TR 36.873 V12.7.0, "Technical Specification Group Radio Access Network; Study on 3D channel model for LTE (Release 12)," 2017.

[54] K. Xia, Y. Wang, and D. Zhang, "Coexistence interference evaluation and analysis of LTE with 3D-MIMO system," *IEEE Int. Symp. Pers. Indoor Mob. Radio Commun. PIMRC*, vol. 2017-Octob, pp. 1–6, 2018.

[55] Y. Zhang, P. Ren, L. Sun, Q. Du, and Y. Wang, "Antenna tilt assignment for three-dimensional beamforming in multiuser systems," *2015 IEEE Glob. Commun. Conf. GLOBECOM 2015*, 2015.

[56] J. Brady and A. Sayeed, "Beamspace MU-MIMO for high-density gigabit small cell access at millimeter-wave frequencies," *IEEE Work. Signal Process. Adv. Wirel. Commun. SPAWC*, vol. 2014-Octob, no. October, pp. 80–84, 2014.

[57] C. Division, K. Abdullah, T. Kaust, and S. Arabia, "Elevation Beamforming in a Multi-Cell Full Dimension Massive MIMO System," in

2018 IEEE Wireless Communications and Networking Conference (WCNC), 2018, pp. 1–6.

[58] R. Pal, K. V. Srinivas, and A. K. Chaitanya, “A Beam Selection Algorithm for Millimeter-Wave Multi-User MIMO Systems,” *IEEE Commun. Lett.*, vol. 22, no. 4, pp. 852–855, 2018.

[59] C. A. Balanis, *Antenna Theory: Analysis and Design*, 3rd ed. New York: Wiley-Interscience, 2005.

[60] M. Tang, G. Cui, L. Zhao, C. Zhou, and W. Wang, “Throughput optimization in MU-MIMO systems via coordinated vertical double-beam tilting,” *Proc. - 2014 IEEE Int. Conf. Comput. Inf. Technol. CIT 2014*, pp. 674–678, 2014.

[61] W. Zhang, Y. Wang, and P. Li, “Interference Coordination with Vertical Beamforming in 3D MIMO-OFDMA networks,” *2014 IEEE Int. Conf. Commun. ICC 2014*, vol. 18, no. 1, pp. 4765–4770, 2014.

[62] N. Seifi, J. Zhang, R. W. Heath, T. Svensson, and M. Coldrey, “Coordinated 3D beamforming for interference management in cellular networks,” *IEEE Trans. Wirel. Commun.*, vol. 13, no. 10, pp. 5396–5410, 2014.

[63] N. Seifi, R. W. Heath, M. Coldrey, and T. Svensson, “Adaptive Multicell 3-D Beamforming in Multiantenna Cellular Networks,” *IEEE Trans. Veh. Technol.*, vol. 65, no. 8, pp. 6217–6231, 2016.

[64] J. Wang, J. Weitzen, O. Bayat, V. Sevindik, and M. Li, “Interference coordination for millimeter wave communications in 5G networks for performance optimization,” *Eurasip J. Wirel. Commun. Netw.*, vol. 46, 2019.

[65] T. S. Rappaport *et al.*, “Millimeter wave mobile communications for 5G cellular: It will work!,” *IEEE Access*, vol. 1, pp. 335–349, 2013.

[66] J. G. Andrews *et al.*, “What will 5G be?,” *IEEE J. Sel. Areas Commun.*, vol. 32, no. 6, pp. 1065–1082, 2014.

[67] N. A. Muhammad, P. Wang, Y. Li, and B. Vucetic, “Analytical Model for

Outdoor Millimeter Wave Channels Using Geometry-Based Stochastic Approach," *IEEE Trans. Veh. Technol.*, vol. 66, no. 2, pp. 912–926, 2017.

[68] L. Wei, R. Hu, Y. Qian, and G. Wu, "Key elements to enable millimeter wave communications for 5G wireless systems," *IEEE Wirel. Commun.*, vol. 21, no. 6, pp. 136–143, 2014.

[69] S. Hur, T. Kim, D. J. Love, J. V. Krogmeier, T. A. Thomas, and A. Ghosh, "Millimeter wave beamforming for wireless backhaul and access in small cell networks," *IEEE Trans. Commun.*, vol. 61, no. 10, pp. 4391–4403, 2013.

[70] S. Mumtaz, J. Rodriguez, and L. Dai, "Introduction to mmWave massive MIMO," *mmWave Massive MIMO A Paradig. 5G*, pp. 1–18, 2017.

[71] M. Xiao *et al.*, "Millimeter Wave Communications for Future Mobile Networks," *IEEE J. Sel. Areas Commun.*, vol. 35, no. 9, pp. 1909–1935, 2017.

[72] Z. Pi and F. Khan, "An introduction to millimeter-wave mobile broadband systems," *IEEE Commun. Mag.*, vol. 49, no. 6, pp. 101–107, 2011.

[73] A. Swindlehurst, E. Ayanoglu, P. Heydari, and F. Capolino, "Millimeter-wave massive MIMO: The next wireless revolution?," *IEEE Commun. Mag.*, vol. 52, no. 9, pp. 56–62, 2014.

[74] A. Alkhateeb, J. Mo, N. González-Prelcic, and R. W. Heath, "MIMO precoding and combining solutions for millimeter-wave systems," *IEEE Commun. Mag.*, vol. 52, no. 12, pp. 122–131, 2014.

[75] S. K. Yong, P. Xia, and A. Valdes-Garcia, *60 GHz Technology for Gbps WLAN and WPAN: From Theory to Practice*. Hoboken, NJ, USA: Wiley, 2010.

[76] K.-C. Huang and Z. Wang, *Millimeterwave Communication Systems*. Hoboken, NJ, USA: Wiley, 2011.

[77] T. S. Rappaport, R. W. Heath, R. C. Daniels, and J. N. Murdock, *Millimeter wave wireless communications*. Englewood Cliffs, NJ, USA:

Prentice-Hall, 2014.

[78] L. Dai, X. Gao, J. Quan, S. Han, and I. Chih-Lin, “Near-optimal hybrid analog and digital precoding for downlink mmWave massive MIMO systems,” *IEEE Int. Conf. Commun.*, vol. 2015-Septe, pp. 1334–1339, 2015.

[79] X. Yu, J. C. Shen, J. Zhang, and K. B. Letaief, “Alternating Minimization Algorithms for Hybrid Precoding in Millimeter Wave MIMO Systems,” *IEEE J. Sel. Top. Signal Process.*, vol. 10, no. 3, pp. 485–500, 2016.

[80] J. Wang, H. Xu, B. Zhu, L. Fan, and A. Zhou, “Hybrid Beamforming Design for mmWave Joint Unicast and Multicast Transmission,” *IEEE Commun. Lett.*, vol. 22, no. 10, pp. 2012–2015, 2018.

[81] A. Mejri, M. Hajjaj, S. Hasnaoui, and R. Bouallegue, “Power factorization based hybrid precoding design for millimeter wave MIMO transmitters using sub-array structure,” *IEEE Int. Symp. Pers. Indoor Mob. Radio Commun. PIMRC*, vol. 2017-Octob, pp. 1–5, 2018.

[82] M. Hajjaj, A. Mejri, R. Bouallegue, and S. Hasnaoui, “Iterative SDR-based Hybrid Precoding Algorithm for mmWave massive MIMO Systems,” *2018 26th Int. Conf. Software, Telecommun. Comput. Networks, SoftCOM 2018*, pp. 213–217, 2018.

[83] A. Mejri, M. Hajjaj, S. Hasnaoui, and R. Bouallegue, “Singular Value Thresholding based Adaptive Approach for Hybrid Beamforming in MmWave Massive MIMO-OFDM Transmitters,” *2018 26th Int. Conf. Software, Telecommun. Comput. Networks, SoftCOM 2018*, pp. 1–5, 2018.

[84] A. M. Elbir and S. Coleri, “Federated learning for hybrid beamforming in mm-Wave massive MIMO,” *IEEE Commun. Lett.*, vol. 24, no. 12, pp. 2795–2799, 2020.

[85] J. Huang, C. Qi, and O. A. Dobre, “Two-Stage Beamforming Design for High-Speed Train mmWave Communications,” *Proc. - IEEE Glob. Commun. Conf. GLOBECOM*, pp. 6621–6626, 2023.

[86] F. Rusek *et al.*, "Scaling Up MIMO: Opportunities and Challenges with Very Large Arrays," *IEEE Signal Process. Mag.*, vol. 30, no. 1, pp. 40–60, 2013.

[87] A. Hakkarainen, J. Werner, K. R. Dandekar, and M. Valkama, "Widely-linear beamforming and RF impairment suppression in massive antenna arrays," *J. Commun. Networks*, vol. 15, no. 4, pp. 383–397, 2013.

[88] S. Cui, A. J. Goldsmith, and A. Bahai, "Energy-efficiency of virtual cooperative MIMO techniques in wireless sensor networks," *IEEE J. Sel. Areas Commun.*, vol. 22, no. 6, pp. 1089–1098, 2004.

[89] J. Brady, N. Behdad, and A. M. Sayeed, "Beamspace MIMO for Millimeter-Wave Communications: System Architecture, Modeling,Analysis, and Measurements," *IEEE Trans. Antennas Propag.*, vol. 61, no. 7, pp. 3814–3827, 2013.

[90] A. M. Sayeed, "Deconstructing multiantenna fading channels," *IEEE Trans. Signal Process.*, vol. 50, no. 10, pp. 2563–2579, 2002.

[91] A. S. Y. Poon, R. W. Brodersen, and D. N. C. Tse, "Degrees of Freedom in Multiple-Antenna Channels : A Signal Space Approach," vol. 51, no. 2, pp. 523–536, 2005.

[92] A. M. Sayeed and N. Behdad, "Continuous aperture phased MIMO: A new architecture for optimum line-of-sight links," *IEEE Antennas Propag. Soc. AP-S Int. Symp.*, pp. 293–296, 2011.

[93] A. Sayeed and J. Brady, "Beamspace MIMO for High-Dimensional Multiuser Communication at Millimeter-Wave Frequencies," *2013 IEEE Glob. Commun. Conf.*, pp. 3679–3684, 2013.

[94] B. Wang, L. Dai, Z. Wang, N. Ge, and S. Zhou, "Spectrum and Energy-Efficient Beamspace MIMO-NOMA for Millimeter-Wave Communications Using Lens Antenna Array," *IEEE J. Sel. Areas Commun.*, vol. 35, no. 10, pp. 2370–2382, 2017.

[95] B. Wang, L. Dai, X. Gao, and L. Hanzo, "Beamspace MIMO-NOMA for

millimeter-wave communications using lens antenna arrays," *IEEE Veh. Technol. Conf.*, vol. 2017-Septe, pp. 1–5, 2018.

[96] P. Liu, Y. Li, W. Cheng, W. Zhang, and X. Gao, "Energy-Efficient Power Allocation for Millimeter Wave Beamspace MIMO-NOMA Systems," *IEEE Access*, vol. 7, pp. 114582–114592, 2019.

[97] P. V. Amadori and C. Masouros, "Low RF-complexity millimeter-wave beamspace-MIMO systems by beam selection," *IEEE Trans. Commun.*, vol. 63, no. 6, pp. 2212–2223, 2015.

[98] X. Gao, L. Dai, Z. Chen, Z. Wang, and Z. Zhang, "Near-Optimal Beam Selection for Beamspace MmWave Massive MIMO Systems," *IEEE Commun. Lett.*, vol. 20, no. 5, pp. 1054–1057, 2016.

[99] R. Pal, A. K. Chaitanya, and K. V. Srinivas, "Low-Complexity Beam Selection Algorithms for Millimeter Wave Beamspace MIMO Systems," *IEEE Commun. Lett.*, vol. 23, no. 4, pp. 768–771, 2019.

[100] R. Pal, K. P. Sarawadekar, and K. V Srinivas, "A Decentralized Beam Selection for MmWave Beamspace Multi-user MIMO System," *AEUE - Int. J. Electron. Commun.*, vol. 111, p. 152884, 2019.

[101] W. Shen, X. Bu, X. Gao, C. Xing, and L. Hanzo, "Beamspace Precoding and Beam Selection for Wideband Millimeter-Wave MIMO Relying on Lens Antenna Arrays," *IEEE Trans. Signal Process.*, vol. 67, no. 24, pp. 6301–6313, 2019.

[102] A. L. Sarker, F. Kader, and D. S. Han, "Rate-Loss Mitigation for a Millimeter-Wave Beamspace MIMO Lens Antenna Array System Using a Hybrid Beam Selection Scheme," *IEEE Syst. J.*, vol. 14, no. 3, pp. 3582–3585, 2020.

[103] A. L. Sarker and D. S. Han, "Hybrid Beamforming with Blockwise Beam Selection for mmWave Beamspace MIMO systems," *2023 14th Int. Conf. Inf. Commun. Technol. Converg.*, pp. 710–712, 2023.

[104] S. Cetinkaya and H. Arslan, "Beamspace MIMO Systems With Reduced Beam Selection Complexity," *IEEE Commun. Lett.*, vol. 27, no. 5, pp.

1427–1431, 2023.

[105] C. Y. Chi, W. C. Li, and C. H. Lin, *Convex Optimization for Signal Processing and Communications: From Fundamentals to Applications*. London: Boca Raton: CRC Press, 2017.

[106] A. Charnes and W. W. Cooper, "Programming with linear fractional functionals," *Nav. Res. Logist.*, vol. 9, no. 3, pp. 181–186, 1962.

[107] S. Schaible, "Parameter-free convex equivalent and dual programs of fractional programming problems," *Manag. Sci.*, vol. 22, no. 8, pp. 868–873, 1976.

[108] W. Dinkelbach, "On nonlinear fractional programming," *Manag. Sci.*, vol. 133, no. 7, pp. 492–498, 1967.

[109] K. Shen and W. Yu, "Fractional Programming for Communication Systems — Part Ⅰ: Power Control and Beamforming," *IEEE Trans. Signal Process.*, vol. 66, no. 10, pp. 2616–2630, 2018.

[110] K. Shen and W. Yu, "Fractional Programming for Communication Systems — Part Ⅱ: Uplink Scheduling via Matching," *IEEE Trans. Signal Process.*, vol. 66, no. 10, pp. 2631–2644, 2018.

[111] Y. Zhang, H. Deng, J. He, Z. Zhu, C. Peng, and H. Xiao, "Spectral Efficiency Optimization of Uplink Millimeter Wave MIMO-NOMA Systems," *Sensors*, vol. 22, no. 17, p. 6466, 2022.

[112] K. Shen, H. V. Cheng, X. Chen, Y. C. Eldar, and W. Yu, "Enhanced Channel Estimation in Massive MIMO via Coordinated Pilot Design," *IEEE Trans. Commun.*, vol. 68, no. 11, pp. 6872–6885, 2020.

[113] R. Munagala, D. N. Amudala, and R. Budhiraja, "Analysis and Optimization of URLLC-Enabled Full Duplex Hybrid Massive MIMO Relaying," *IEEE Trans. Commun.*, vol. 72, no. 4, pp. 2027–2044, 2024.

[114] H. Li, M. Li, and Q. Liu, "Hybrid Beamforming With Dynamic Subarrays and Low-Resolution PSs for mmWave MU-MSO Systems," *IEEE Trans. Commun.*, vol. 68, no. 1, pp. 602–614, 2020.

[115] Y. Liu, C. Li, J. Li, and L. Feng, “Joint User Scheduling and Hybrid Beamforming Design for Massive MIMO LEO Satellite Multigroup Multicast Communication Systems,” *Sensors*, vol. 22, no. 18, p. 6858, 2022.

[116] T. S. Abdu, S. Kisseleff, E. Lagunas, S. Chatzinotas, and B. Ottersten, “Demand and Interference Aware Adaptive Resource Management for High Throughput GEO Satellite Systems,” *IEEE Open J. Commun. Soc.*, vol. 3, pp. 759–775, 2022.

[117] J. Li, R. Chai, C. Liu, C. Liang, Q. Chen, and F. R. Yu, “Energy-Aware Joint Route Selection and Resource Allocation in Heterogeneous Satellite Networks,” *IEEE Trans. Veh. Technol.*, vol. 73, no. 8, pp. 12067–12081, 2024.

[118] J. Tang, J. Nie, Z. Xiong, J. Zhao, Y. Zhang, and D. Niyato, “Slicing-Based Reliable Resource Orchestration for Secure Software-Defined Edge-Cloud Computing Systems,” *IEEE Internet Things J.*, vol. 9, no. 4, pp. 2637–2648, 2022.

[119] R. Reifert *et al.*, “Rate-Splitting and Common Message Decoding in Hybrid Cloud / Mobile Edge Computing Networks,” *IEEE J. Sel. Areas Commun.*, vol. 41, no. 5, pp. 1566–1583, 2023.

[120] T. Zhang, D. Xu, A. Tolba, K. Yu, H. Song, and S. Yu, “Reinforcement-Learning-Based Offloading for RIS-Aided Cloud-Edge Computing in IoT Networks: Modeling, Analysis, and Optimization,” *IEEE Internet Things J.*, vol. 11, no. 11, pp. 19421–19439, 2024.

[121] L. Guo, J. Jia, J. Chen, and X. Wang, “Secure Communication Optimization in NOMA Systems With UAV-Mounted STAR-RIS,” *IEEE Trans. Inf. Forensics Secur.*, vol. 19, pp. 2300–2314, 2024.

[122] R. Tang, W. Zhou, R. Zhang, Y. Xu, X. Li, and H. Zhang, “Utility Maximization for Multi-UAV-Assisted IoT Sensor Systems With NOMA,” *IEEE Sens. J.*, vol. 24, no. 17, pp. 28233–28250, 2024.

[123] R. Ye, Y. Peng, F. Al-hazemi, and R. Boutaba, “A Robust Cooperative

Jamming Scheme for Secure UAV Communication via Intelligent Reflecting Surface," *IEEE Trans. Commun.*, vol. 72, no. 2, pp. 1005–1019, 2024.

[124] S. Asaad, Y. Wu, A. Bereyhi, R. R. Müller, R. F. Schaefer, and H. V. Poor, "Secure Active and Passive Beamforming in IRS-Aided MIMO Systems," *EEE Trans. Inf. Forensics Secur.*, vol. 17, pp. 1300–1315, 2022.

[125] S. Liu, R. Liu, M. Li, Y. Liu, and Q. Liu, "Joint BS-RIS-User Association and Beamforming Design for RIS-Assisted Cellular Networks," *IEEE Trans. Veh. Technol.*, vol. 72, no. 5, pp. 6113–6128, 2023.

[126] H. Zhou, M. Erol-kantarci, Y. Liu, and H. V. Poor, "A Survey on Model-Based , Heuristic , and Machine Learning Optimization Approaches in RIS-Aided Wireless Networks," *IEEE Commun. Surv. Tutorials*, vol. 26, no. 2, pp. 781–823, 2024.

[127] L. Cantos, J. Choi, and Y. H. Kim, "Exploiting Active Intelligent Reflecting Surface for Wireless Powered Nonorthogonal Multiple Access," *IEEE Trans. Wirel. Commun.*, vol. 23, no. 6, pp. 5740–5755, 2024.

[128] Y. Chen, L. Zhao, and K. Shen, "Mixed Max-and-Min Fractional Programming for Wireless Networks," *IEEE Trans. Signal Process.*, vol. 72, pp. 337–351, 2024.

[129] 3GPP TR 36.932 V12.1.0, "Scenarios and requirements for small cell enhancements for E-UTRA and E-UTRAN," 2013.

[130] A. K. Al-samarrie, H. Alyasiri, and A. H. Al-nakkash, "Proposed Multi-Stage PSO Scheme for LTE Network Planning and Operation," *Int. J. Appl. Eng. Res. ISSN*, vol. 11, no. 20, pp. 10199–10210, 2016.

[131] D. Kimura and H. Seki, "Inter-Cell Interference Coordination (ICIC) Technology," *Fujitsu Sci. Tech. J.*, vol. 48, no. 1, pp. 89–94, 2012.

[132] D. López-Pérez, G. De La Roche, A. Valcarce, A. Jüttner, and J. Zhang, "Interference avoidance and dynamic frequency planning for WiMAX

femtocells networks," *2008 11th IEEE Singapore Int. Conf. Commun. Syst. ICCS 2008*, pp. 1579–1584, 2008.

[133] M. Kaneko, T. Nakano, K. Hayashi, T. Kamenosono, and H. Sakai, "Distributed Resource Allocation with Local CSI Overhearing and Scheduling Prediction for OFDMA Heterogeneous Networks," *IEEE Trans. Veh. Technol.*, vol. 66, no. 2, pp. 1186–1199, 2017.

[134] Y. Xu, Y. Hu, Q. Chen, T. Song, and R. Lai, "Robust resource allocation for multi-tier cognitive heterogeneous networks," *IEEE Int. Conf. Commun.*, pp. 1–6, 2017.

[135] T. Lv, C. Liu, and H. Gao, "Novel user scheduling algorithms for carrier aggregation system in heterogeneous network," *IEEE Wirel. Commun. Netw. Conf. WCNC*, pp. 1–6, 2017.

[136] A. Celik, R. M. Radaydeh, F. S. Al-Qahtani, and M. S. Alouini, "Joint interference management and resource allocation for device-to-device (D2D) communications underlying downlink/uplink decoupled (DUDe) heterogeneous networks," *IEEE Int. Conf. Commun.*, pp. 1–6, 2017.

[137] S. A. Khan, A. Kavak, S. A. Çolak, and K. Küçük, "A novel fractional frequency reuse scheme for interference management in LTE-A hetnets," *IEEE Access*, vol. 7, pp. 109662–109672, 2019.

[138] J. Huang, P. Zhou, K. Luo, Z. Yang, and G. He, "Two-Stage Resource Allocation Scheme for Three-Tier Ultra-Dense Network," *China Commun.*, vol. 14, no. 10, pp. 118–129, 2017.

[139] Y. Xu, Y. Hu, G. Li, and H. Zhang, "Robust resource allocation for heterogeneous wireless network: A worst-case optimisation," *IET Commun.*, vol. 12, no. 9, pp. 1064–1071, 2018.

[140] Kyocera, "Potential performance of range expansion in macro-pico deployment(r1-104355)," *3GPP TSG RAN WG1 Meet.*, 2010.

[141] E. Mugume and D. K. C. So, "User Association in Energy-Aware Dense Heterogeneous Cellular Networks," *IEEE Trans. Wirel. Commun.*, vol. 16, no. 3, pp. 1713–1726, 2017.

[142] H. S. Jo, Y. J. Sang, P. Xia, and J. G. Andrews, “Heterogeneous cellular networks with flexible cell association: A comprehensive downlink SINR analysis,” *IEEE Trans. Wirel. Commun.*, vol. 11, no. 10, pp. 3484–3494, 2012.

[143] Y. S. Soh, T. Q. S. Quek, M. Kountouris, and H. Shin, “Energy efficient heterogeneous cellular networks,” *IEEE J. Sel. Areas Commun.*, vol. 31, no. 5, pp. 840–850, 2013.

[144] I. Guvenc, “Capacity and fairness analysis of heterogeneous networks with range expansion and interference coordination,” *IEEE Commun. Lett.*, vol. 15, no. 10, pp. 1084–1087, 2011.

[145] H. S. Dhillon, R. K. Ganti, and J. G. Andrews, “Load-aware modeling and analysis of heterogeneous cellular networks,” *IEEE Trans. Wirel. Commun.*, vol. 12, no. 4, pp. 1666–1677, 2013.

[146] S. Corroy, L. Falconetti, and R. Mathar, “Dynamic cell association for downlink sum rate maximization in multi-cell heterogeneous networks,” *IEEE Int. Conf. Commun.*, pp. 2457–2461, 2012.

[147] Q. Ye, B. Rong, Y. Chen, M. Al-Shalash, C. Caramanis, and J. G. Andrews, “User association for load balancing in heterogeneous cellular networks,” *IEEE Trans. Wirel. Commun.*, vol. 12, no. 6, pp. 2706–2716, 2013.

[148] N. Hassan and X. Fernando, “Interference mitigation and dynamic user association for load balancing in heterogeneous networks,” *IEEE Trans. Veh. Technol.*, vol. 68, no. 8, pp. 7578–7592, 2019.

[149] S. Singh, H. S. Dhillon, and J. G. Andrews, “Offloading in heterogeneous networks: Modeling, analysis, and design insights,” *IEEE Trans. Wirel. Commun.*, vol. 12, no. 5, pp. 2484–2497, 2013.

[150] D. Fooladivanda, A. Al Daoud, and C. Rosenberg, “Joint channel allocation and user association for heterogeneous wireless cellular networks,” *IEEE Int. Symp. Pers. Indoor Mob. Radio Commun. PIMRC*, pp. 384–390, 2011.

[151] R. Sun, M. Hong, and Z. Q. Luo, “Joint downlink base station association and power control for max-min fairness: Computation and complexity,” *IEEE J. Sel. Areas Commun.*, vol. 33, no. 6, pp. 1040–1054, 2015.

[152] T. Zhou, Z. Liu, J. Zhao, C. Li, and L. Yang, “Joint User Association and Power Control for Load Balancing in Downlink Heterogeneous Cellular Networks,” *IEEE Trans. Veh. Technol.*, vol. 67, no. 3, pp. 2582–2593, 2018.

[153] H. Liu, Z. Gao, X. Shao, X. Shan, and W. Zhou, “Joint user association and resource allocation for interference mitigation and load balancing in HCNs,” *J. Commun.*, vol. 11, no. 11, pp. 977–983, 2016.

[154] N. Miki and Y. Kanehira, “Investigation on Distributed Optimization of User Association and Inter-Cell Interference Coordination Based on Proportional Fair Criteria,” *2019 16th IEEE Annu. Consum. Commun. Netw. Conf. CCNC 2019*, pp. 1–5, 2019.

[155] J. G. Andrews, F. Baccelli, and R. K. Ganti, “A tractable approach to coverage and rate in cellular networks,” *IEEE Trans. Commun.*, vol. 59, no. 11, pp. 3122–3134, 2011.

[156] A. Guo and M. Haenggi, “Spatial stochastic models and metrics for the structure of base stations in cellular networks,” *IEEE Trans. Wirel. Commun.*, vol. 12, no. 11, pp. 5800–5812, 2013.

[157] B. Blaszczyszyn, M. K. Karray, and H. P. Keeler, “Using Poisson processes to model lattice cellular networks,” *2013 Proc. IEEE INFOCOM*, pp. 773–781, 2013.

[158] Q. Nadeem, A. Kammoun, and M.-S. Alouini, “Elevation Beamforming with Full Dimension MIMO Architectures in 5G Systems : A Tutorial,” *IEEE Commun. Surv. Tutorials*, vol. 21, no. 4, pp. 1–35, 2019.

[159] R. W. Heath, N. Gonzalez-Prelcic, S. Rangan, W. Roh, and A. M. Sayeed, “An Overview of Signal Processing Techniques for Millimeter Wave MIMO Systems,” *IEEE J. Sel. Top. Signal Process.*, vol. 10, no.

3, pp. 436–453, 2016.

[160] Q. Zheng, R. Liu, X. Cheng, S. Sun, and X. Chen, "Optimal downtilts for 3D beamforming in massive MIMO networks with imperfect CSI," in *2016 16th International Symposium on Communications and Information Technologies, ISCIT 2016*, 2016, pp. 569–573.

[161] J. Yang, M. Ding, G. Mao, Z. Lin, D.-G. Zhang, and T. H. Luan, "Optimal Base Station Antenna Downtilt in Downlink Cellular Networks," *IEEE Trans. Wirel. Commun.*, vol. 18, no. 3, pp. 1779–1791, 2019.

[162] V. A. Zorich, "Integration," in *Mathematical Analysis I*, Springer, 2004.

[163] H. T. Friis, "A note on a simple transmission formula," *Proc. IRE*, vol. 34, no. 5, pp. 254–256.

[164] A. A.Asaker, R. S. Ghoname, and A. A. Zekry, "Design of a Planar MIMO Antenna for LTE-Advanced," *Int. J. Comput. Appl.*, vol. 115, no. 12, pp. 27–33, 2015.

[165] R. Yang, "Beam Space Signal Processing for Directional Transmission Phased Arrays," no. June, 2018.

[166] M. Joham, W. Utschick, and J. A. Nossek, "Linear Transmit Processing in MIMO Communications Systems," *IEEE Trans. Signal Process.*, vol. 53, no. 8, pp. 2700–2712, 2005.

[167] E. Björnson, M. Bengtsson, and B. Ottersten, "Optimal Multiuser Transmit Beamforming: A Difficult Problem with a Simple Solution Structure," *IEEE Signal Process. Mag.*, vol. 31, no. 4, pp. 142–148, 2014.

[168] M. R. Akdeniz *et al.*, "Millimeter Wave Channel Modeling and Cellular Capacity Evaluation," *IEEE J. Sel. Areas Commun.*, vol. 32, no. 6, pp. 1164–1179, 2014.

[169] X. Gao, L. Dai, S. Han, C.-L. I, and X. Wang, "Reliable Beamspace Channel Estimation for Millimeter-Wave Massive MIMO Systems with Lens Antenna Array," *IEEE Trans. Wirel. Commun.*, vol. 16, no. 9, pp. 6010–6021, 2017.

[170] C. Masouros, M. Sellathurai, and T. Ratnarajah, “Computationally Efficient Vector Perturbation Precoding Using Thresholded Optimization,” *IEEE Trans. Commun.*, vol. 61, no. 5, pp. 1880–1890, 2013.

[171] T. S. Rappaport, J. N. Murdock, and F. Gutierrez, “State of the Art in 60-GHz Integrated Circuits and Systems for Wireless Communications,” *Proc. IEEE*, vol. 99, no. 8, pp. 1390–1436, 2011.

[172] J. C. Bezdek and R. J. Hathaway, “Some Notes on Alternating Optimization,” in *Advances in Soft Computing — AFSS 2002*, Heidelberg, Ed. Berlin: Springer, 2002, pp. 288–300.

[173] A. Hu, “Beam Grouping Based User Scheduling in Multi-Cell Millimeter-Wave MIMO Systems,” *IEEE Access*, vol. 6, pp. 55004–55012, 2018.

[174] S. P. Boyd and L. Vandenberghe, *Convex Optimization*. Cambridge: Cambridge University Press, 2004.

[175] A. Damnjanovic *et al.*, “A survey on 3GPP heterogeneous networks,” *IEEE Wirel. Commun.*, vol. 18, no. 3, pp. 10–21, 2011.

[176] A. Ghosh *et al.*, “Heterogeneous cellular networks: From theory to practice,” *IEEE Commun. Mag.*, vol. 50, no. 6, pp. 54–64, 2012.

[177] R. W. Heath, M. Kountouris, and T. Bai, “Modeling heterogeneous network interference using poisson point processes,” *IEEE Trans. Signal Process.*, vol. 61, no. 16, pp. 4114–4126, 2013.

[178] J. Wang, X. Chu, M. Ding, and D. López-Pérez, “On the performance of multi-tier Heterogeneous networks under LoS and NLoS transmissions,” *2016 IEEE Globecom Work. GC Wkshps 2016 - Proc.*, pp. 0–5, 2016.

[179] H. Hu, J. Zhang, X. Chu, and J. Zhang, “Downlink Coverage Analysis of K-Tier Heterogeneous Networks with Multiple Antennas,” *IEEE Int. Conf. Commun.*, vol. 2019-May, pp. 1–6, 2019.

[180] C. Chen, J. Zhang, X. Chu, and J. Zhang, “On the Optimal Base-Station Height in mmWave Small-Cell Networks Considering Cylindrical Blockage Effects,” *IEEE Trans. Veh. Technol.*, vol. 70, no. 9, pp. 9588–

9592, 2021.

[181] D. Liu *et al.*, "User Association in 5G Networks: A Survey and an Outlook," *IEEE Commun. Surv. Tutorials*, vol. 18, no. 2, pp. 1018–1044, 2016.

[182] A. K. Gupta, H. S. Dhillon, S. Vishwanath, and J. G. Andrews, "Downlink multi-antenna heterogeneous cellular network with load balancing," *IEEE Trans. Commun.*, vol. 62, no. 11, pp. 4052–4067, 2014.

[183] C. Chen, J. Zhang, X. Chu, and J. Zhang, "On the Deployment of Small Cells in 3D HetNets With Multi-Antenna Base Stations," *IEEE Trans. Wirel. Commun.*, vol. 21, no. 11, pp. 9761–9774, 2022.

[184] E. Turgut and M. Cenk Gursoy, "Coverage in Heterogeneous Downlink Millimeter Wave Cellular Networks," *IEEE Trans. Commun.*, vol. 65, no. 10, pp. 4463–4477, 2017.

[185] M. Tang, G. Cui, X. Zou, W. Wang, and Y. Zhang, "A 3D-beamforming scheme for throughput optimization in Heterogeneous Network," *CCIS 2014 - Proc. 2014 IEEE 3rd Int. Conf. Cloud Comput. Intell. Syst.*, pp. 222–227, 2014.

[186] X. Li, C. Li, S. Jin, and X. Gao, "Interference Coordination for 3D Beamforming Based HetNet Exploiting Statistical Channel State Information," *IEEE Trans. Wirel. Commun.*, vol. PP, no. XX, pp. 1–1, 2018.

[187] D. Li, J. Xu, X. Wang, and X. Tao, "Joint Optimization for Cell Association and Vertical Downtilts Adjustment in 3D MIMO enabled HetNets," in *2018 IEEE Wireless Communications and Networking Conference (WCNC)*, 2018, pp. 1–6.

[188] X. Li, T. Bai, and R. W. Heath, "Impact of 3D Base Station Antenna in Random Heterogeneous Cellular Networks," *2014 IEEE Wirel. Commun. Netw. Conf.*, vol. 3, pp. 2254–2259, 2014.

[189] X. Li, R. W. Heath, K. Linehan, and R. Butler, "Impact of Metro Cell Antenna Pattern and Downtilt in Heterogeneous Networks," *arXiv Prepr.*

arXiv1502.05782, 2015.

[190] E. Mugume, “Green Heterogeneous Cellular networks,” Univ. Manchester, Manchester, U.K., 2016.

[191] F. Gunnarsson *et al.*, “Downtilted base station antennas - A simulation model proposal and impact on HSPA and LTE performance,” *IEEE Veh. Technol. Conf.*, pp. 13–17, 2008.

[192] D. López-Pérez, M. Ding, H. Claussen, and A. H. Jafari, “Towards 1 Gbps/UE in Cellular Systems: Understanding Ultra-Dense Small Cell Deployments,” *IEEE Commun. Surv. Tutorials*, vol. 17, no. 4, pp. 2078–2101, 2015.

[193] T. Bai and R. W. Heath, “Coverage and rate analysis for millimeter-wave cellular networks,” *IEEE Trans. Wirel. Commun.*, vol. 14, no. 2, pp. 1100–1114, 2015.

[194] R. . Streit, *Poisson Point Processes: Imaging, Tracking, and Sensing*. New York: USA: Springer, 2010.

[195] M. Abramowitz and I. Stegun, *Handbook of Mathematical Functions With Formulas, Graphs, and Mathematical Tables*. New York: USA: Dover, 1972.

[196] S. S. Dragomir, “A Survey on Cauchy-Bunyakovsky-Schwarz Type Discrete Inequalities,” *J. Inequalities Pure Appl. Math.*, vol. 4, no. 3, p. 140, 2003.

[197] A. M. Fink and M. J. Jodeit, “On Chebyshev’s Other Inequality,” in *Inequalities in Statistics and Probability*, vol. 5, Y. L. Tong, Ed. Institute of Mathematical Statistics, 1984, pp. 115–120.

[198] M. S. Alouini and A. J. Goldsmith, “Area spectral efficiency of cellular mobile radio systems,” *IEEE Trans. Veh. Technol.*, vol. 48, no. 4, pp. 1047–1066, 1999.

[199] C. Li, J. Zhang, J. G. Andrews, and K. B. Letaief, “Success probability and area spectral efficiency in multiuser MIMO hetnets,” *IEEE Trans. Commun.*, vol. 64, no. 4, pp. 1544–1556, 2016.

[200] A. J. Fehske, F. Richter, and G. P. Fettweis, “Energy efficiency improvements through micro sites in cellular mobile radio networks,” *2009 IEEE Globecom Work. Gc Work. 2009*, pp. 1–5, 2009.

[201] H. Klessig, A. J. Fehske, and G. P. Fettweis, “Energy efficiency gains in interference-limited heterogeneous cellular mobile radio networks with random micro site deployment,” *2011 34th IEEE Sarnoff Symp. SARNOFF 2011*, no. 1, pp. 1–6, 2011.

[202] M. Deruyck, D. De Vulder, W. Joseph, and L. Martens, “Modelling the power consumption in femtocell networks,” *2012 IEEE Wirel. Commun. Netw. Conf. Work. WCNCW 2012*, no. 2, pp. 30–35, 2012.

[203] G. Simmons, *Calculus with Analytic Geometry*, 2nd ed. New York: USA: McGraw-Hill, 1995.

[204] S. I. Grossman, *Calculus*, 3rd ed. Amsterdam: The Netherlands: Elsevier, 1984.

[205] L. Zhang, X. Gu, Z. Liu, and L. Zhang, “Energy Efficiency Analysis for Future 3D Ultra Dense Mobile Networks with Sleep Mode,” *Int. Symp. Wirel. Pers. Multimed. Commun. WPMC*, pp. 1–6, 2017.

[206] J. Miao, X. Gu, L. Zhang, and B. Leng, “Energy Efficiency Analysis for Future 3D Mobile Networks with Strategic Sleep Mode,” *Int. Symp. Wirel. Pers. Multimed. Commun. WPMC*, pp. 1–6, 2019.